

---

---

# **Mass Distributions of Galaxies from SAURON and CALIFA Stellar Kinematic Maps**

**Veselina Kalinova**  
Max-Planck-Institut für Astronomie

---

---

**Heidelberg 2014**



*Dissertation in Astronomy*  
submitted to the  
**Combined Faculties of the Natural Sciences and Mathematics**  
**of the Ruperto-Carola-University of Heidelberg, Germany,**  
for the degree of  
*Doctor of Natural Sciences*

Put forward by  
**M.Sc. *Veselina Kalinova***  
born in Sliven, Bulgaria

**Oral examination: 30.04.2014**



---

---

# **Mass Distributions of Galaxies from SAURON and CALIFA Stellar Kinematic Maps**

**Veselina Kalinova**  
Max-Planck-Institut für Astronomie

---

---

**Referees: Dr. Glenn van de Ven**  
**Prof. Dr. Luca Amendola**



# Zusammenfassung

Die Menge und Verteilung dunkler Materie in Galaxien bestimmt wesentlich deren Entstehung, Entwicklung und ihren dynamischen Zustand. In der vorliegenden Arbeit erschließen wir die interne Massenverteilung von 26 E–Sd-Galaxien anhand zweidimensionaler stellarer kinematischer Karten, die mit SAURON sowie im Rahmen des CALIFA -Beobachtungsprogrammes gemessen wurden. Wir vergleichen dabei zwei Modellierungsansätze – Anpassung von Lösungen der axisymmetrischen Jeans-Gleichungen, und die weitverbreitete Korrektur Asymmetrischen Drifts (engl.: asymmetric drift correction, "ADC"). Wir zeigen daß ADC die eingeschlossene Masse um einen Faktor  $\sim 3-4$  unterschätzt sobald die ungeordnete Bewegung (Dispersion) bedeutsam im Vergleich zu geordneter Bewegung (Strömung) wird, also das Verhältnis geordneter-zu-ungeordneter Bewegung einen Wert von etwa 1.5 unterschreitet. Genau wie es in Bulges und dicken Scheiben von Spiralgalaxien sowie in elliptischen Galaxien der Fall ist, indizieren solche Bewegungszustände, daß die stellare Masse nicht auf die galaktische Scheibenebene beschränkt ist. Da diese Situation allgemein anzutreffen ist, und nicht nur in den Galaxien unserer Untersuchung, muß auch generell die vollständige Integration von Lösungen der Jeans-Gleichungen herangezogen werden wenn die galaktische Massenverteilung zuverlässig ermittelt werden soll. Wir benutzen folglich diese realistischere Methode um den Anteil dunkler Materie zu bestimmen, wobei wir das totale Masse-zu-Licht-Verhältnis zuerst aus den dynamischen Modellen errechnen, und es dann mit dem Wert vergleichen, der für Sterne (Baryonen) aus stellaren Populationsmodellen abgeleitet wurde.

Im Ergebnis dieser Untersuchung zeigen sich einige statistische Zusammenhänge zwischen dem Massenanteil dunkler Materie und globalen Galaxieigenschaften. Elliptische Galaxien (E) und Spiralgalaxien späten Typs (Scd-Sd) gehören zu den Objekten mit dem höchsten Dunkelanteil, während linsenförmige (S0) und Spiralgalaxien frühen Typs (Sa–Sb) wesentlich geringere Anteile dunkler Materie besitzen. Im Allgemeinen nimmt  $f_{DM}$  zu den größten als auch den kleinsten Galaxiemassen hin zu, und ist kleiner bei Galaxien mittlerer Masse. Weiterhin ist es mit dem Verhältnis von geordneter-zu-ungeordneter Bewegung antikorreliert, das heißt dispersionsdominierte Galaxien weisen größere Dunkelanteile auf. Schließlich untersuchen wir die maximalen Rotationsgeschwindigkeiten und die Form der Rotationskurven in Abhängigkeit des galaktomorphischen Typs innerhalb der Hubble-Reihe. Rotationskurven mit ausgeprägtem Maximum sind in Galaxien frühen Typs zu finden, während langsam steigende Kurven typisch für späte Galaxientypen sind. Dies bestätigt Vorhersagen aktueller Simulationen der Galaxienentwicklung mit Photoionisations-Rückkopplung. In ihrer Gesamtheit liefern unsere Ergebnisse zum Gehalt dunkler Materie und der Dynamik von Galaxien empirische Randbedingungen für gegenwärtige und zukünftige theoretische Modelle der Galaxienentwicklung für eine Vielfalt von Massen und morphologischer Typen, und werden somit zum Verständnis der relevanten physikalischen Prozesse beitragen.



# Abstract

The amount and distribution of dark matter in galaxies defines the formation, evolution and dynamics of these systems. In this thesis we infer the internal mass distributions of 26 E–Sd galaxies using SAURON and CALIFA two-dimensional stellar kinematic maps. We compare two modeling approaches – fitting a solution of the axisymmetric Jeans equations and the commonly applied asymmetric drift correction (ADC). We show that ADC underestimates the enclosed mass by a factor of  $\sim 3\text{--}4$  once random motion (velocity dispersion) becomes significant compared to ordered motion (streaming), that is, when the ratio of ordered-over-random motion is less than about 1.5. Such kinematics indicate that the stellar mass of the galaxy is not confined to the disk plane, as happens in bulges and thick disks of spiral galaxies, as well as in elliptical galaxies. Since this is frequently realized in our sample, as well as in the general galaxy population, a full line-of-sight integration as provided by solutions of the axisymmetric Jeans equation is needed to reliably infer mass distributions in galaxies. We henceforth use the more realistic Jeans models to estimate the dark matter fraction ( $f_{DM}$ ), by modeling the total (dynamical) mass-to-light ratio and comparing it with the value derived for stars (baryons) from stellar population models.

We find several trends of dark matter fraction with global galaxy properties. Ellipticals (E) and late-type spiral (Scd–Sd) galaxies are the most dark matter-dominated objects, while lenticular (S0) and early-type spirals (Sa–Sb) have significantly smaller dark matter fractions. On average,  $f_{DM}$  increases both at highest and lowest galaxy (stellar) masses, and is smaller at intermediate masses. Further, it is also anticorrelated with the ratio of ordered-over-random motion, that is dispersion-dominated galaxies show a higher dark matter fraction. Finally, we investigate the maximum circular velocities and qualitative shape of rotation curves as a function of galaxy morphological type along the Hubble sequence. Peaked rotation curves are found in early-type galaxies, while slowly rising rotation curves are typical for late-type spirals. This confirms predictions of recent simulations of galaxy evolution with local photoionization feedback. More generally, our results for dark matter content and dynamics provide empirical constraints on current and future theoretical models of galaxy evolution across a wide range of galaxy morphological types and masses, and thereby will help us to understand the relevant physical processes.



*Dedicated to my grandmother  
Mariya Georgieva...*



# CONTENTS

1	INTRODUCTION	1
CHAPTER 1		1
1.1	GALAXIES	1
1.2	MORPHOLOGICAL CLASSIFICATION: HUBBLE SEQUENCE	2
1.3	STRUCTURE OF DISC GALAXIES	5
1.4	STRUCTURE OF ELLIPTICAL GALAXIES	8
1.5	REVISED HUBBLE SEQUENCE FROM ATLAS <sup>3D</sup> SURVEY	10
1.6	DARK MATTER ON GALACTIC SCALES	12
1.6.1	DARK MATTER DISCOVERY	13
1.6.2	SHAPE OF THE ROTATION VELOCITY CURVES	14
1.7	SCALE RADIUS AND DISK ROTATIONAL VELOCITY. MAXIMAL DISC THEORY	16
1.8	INNER DYNAMICAL MASS ACROSS GALAXY MORPHOLOGY	16
1.9	GALAXY FORMATION: RECENT SIMULATIONS	19
1.9.1	STELLAR-TO-HALO MASS RELATION	19

1.9.2	LOCAL PHOTOIONIZATION FEEDBACK SHAPES THE ROTATION CURVES . . . . .	20
1.10	OUTLINE OF THE THESIS . . . . .	21
<b>2</b>	<b>DATA AND MODELS</b>	<b>23</b>
<b>CHAPTER2</b>		<b>23</b>
2.1	INTRODUCTION . . . . .	23
2.2	DATA AND SAMPLE SELECTION . . . . .	25
2.2.1	SAURON AND CALIFA INTEGRAL-FIELD SPECTROSCOPY . . . . .	26
2.3	STELLAR KINEMATICS EXTRACTION . . . . .	29
2.4	NEAR-INFRARED IMAGING . . . . .	30
2.5	PHOTOMETRIC AND MASS MODELLING METHODS . . . . .	32
2.5.1	AXISYMMETRIC JEANS EQUATIONS . . . . .	32
2.5.2	MULTI-GAUSSIAN EXPANSION . . . . .	34
2.5.3	ASYMMETRIC DRIFT CORRECTION . . . . .	35
2.6	SUMMARY . . . . .	37
<b>3</b>	<b>AXISYMMETRIC JEANS EQUATIONS VERSUS ASYMMETRIC DRIFT CORRECTION</b>	<b>39</b>
<b>CHAPTER3</b>		<b>39</b>
3.1	INTRODUCTION . . . . .	39
3.2	SURFACE BRIGHTNESS PARAMETRISATION . . . . .	41
3.3	STELLAR KINEMATIC MAPS . . . . .	43
3.4	DYNAMICAL MODELING . . . . .	46
3.4.1	AXISYMMETRIC JEANS EQUATIONS . . . . .	46
3.4.2	ASYMMETRIC DRIFT CORRECTION: RADIAL PROFILES . . . . .	46

3.5	COMPARING CIRCULAR VELOCITY CURVES . . . . .	63
3.6	DISCUSSION . . . . .	63
3.6.1	ASSUMPTIONS IN THE MASS MODELS . . . . .	67
3.6.2	BULGES, THICK DISCS AND SPHEROIDS . . . . .	69
3.7	CONCLUSIONS . . . . .	70
4	MASS DISTRIBUTIONS OF GALAXIES ACROSS HUBBLE SEQUENCE: THE LINK BETWEEN GALACTIC KINEMATICS AND DARK MATTER CONTENT	<b>73</b>
	CHAPTER4	<b>73</b>
4.1	INTRODUCTION . . . . .	74
4.2	MASS DISTRIBUTIONS OF GALAXIES ACROSS HUBBLE SEQUENCE . . . . .	76
4.2.1	DYNAMICAL MASS . . . . .	76
4.2.2	STELLAR MASS DISTRIBUTION . . . . .	77
4.2.3	GAS MASS MODEL . . . . .	78
4.2.4	BARYONIC AND DARK MATTER RADIAL PROFILES . . . . .	79
4.3	INNER DYNAMICAL SCALINGS OF GALAXIES: CORRELATION WITH TOTAL STELLAR MASS . . . . .	82
4.4	VELOCITY SCALINGS OF GALAXIES: CONNECTIONS WITH MAXIMAL OR SUB-MAXIMAL DISKS . . . . .	85
4.5	SHAPE OF THE ROTATION CURVES ACROSS HUBBLE SEQUENCE . . . . .	90
4.6	DISCUSSION . . . . .	90
4.6.1	DYNAMICAL CLASSIFICATION OF GALAXIES . . . . .	91
4.6.2	LINK WITH RECENT SIMULATIONS IN GALAXY FORMATION . . . . .	94
4.7	CONCLUSIONS . . . . .	95
5	SUMMARY AND FUTURE WORK	<b>101</b>
	CHAPTER5	<b>101</b>

---

APPENDIX	<b>107</b>
5.1 ADC ASSUMPTIONS . . . . .	107
5.1.1 REPRESENTATIVE GALAXY MODEL . . . . .	107
5.1.2 POWER-LAW STREAMING MOTION . . . . .	110
5.1.3 SHAPE OF THE VELOCITY ELLIPSOID . . . . .	110
5.2 MULTI-GAUSSIAN EXPANSION TABLES . . . . .	112
ACKNOWLEDGEMENTS	<b>133</b>
BIBLIOGRAPHY	<b>135</b>

## 1.1 GALAXIES

*“The Milky Way is nothing else but a mass of innumerable stars planted together in clusters”*. In his revolutionary work *Sidereus Nuncius* or *The Sidereal Messenger* in 1610, Galileo Galilei first brought to light that our galaxy consists of stars when it is observed through a telescope. Cosmological speculations started right after these observations. In 1750, English astronomer Thomas Wright first described the shape of the Milky Way in his *An original theory or new hypothesis of the Universe* and proposed the idea that faint nebulae were distant galaxies, i.e. solar systems but on a much larger scale. In 1755, Immanuel Kant developed Wright’s idea about the structure of the Milky Way. He introduced the term “island universe” for these distant nebulae and suggested that their flattening was caused by rotation. Until the end of the eighteenth centuries, these early cosmologies did not have an observational support.

Charles Messier made significant contributions due to his interest in distinguishing comets from diffuse nebulae. In the late 18th century, he catalogued 109 “bright nebulae” and his *Messier Catalogue* is still used today to identify the brightest Galactic and extragalactic objects. In contrast to Messier, the German-born British astronomer William Herschel was directly interested in identifying these nebulae based upon visual observations. He, his sister, Caroline, and his son, John Herschel, contributed to first systematic catalogue of 5079 nebulae, the *General Catalogue of Nebulae and Clusters of Stars*, published in 1864. In 1888, the Danish-Irish astronomer John Dreyer extended this catalogue to *New General Catalogue of Nebulae and Clusters of Stars*, and with the supplementary *Index Catalogues* of 1895 and 1908, contained 15 000 objects. Even with such large catalogues of known objects, their natures remained unclear.

Looking for answers, William Herschel was one of the first astronomers to estimate the stellar

distribution of the Milky Way based on astronomical observations. His method relied on counting stars in different directions, assuming a constant intrinsic luminosity for all of them. Herschel described the structure of the Milky Way as a flattened disc of stars with a diameter about five times its thickness, and where the Sun is located near its center (Herschel 1785). Later, in the 1860s, William Huggins used spectroscopic observations of diffuse nebulae to show that many of these objects were clouds of gas. Another spectroscopic analysis in 1912 by Vesto Slipher proved that the spiral nebulae were rotating, but it was still a mystery if these nebulae were part of Milky Way or outside of it. *The Great Debate* between Harlow Shapley and Heber Curtis was a public discussion in 1920, inspired by this big question. Shapley believed that the “island universes” were part of the Milky Way, while Curtis argued that the nebulae were distant galaxies. Their arguments were based on partially incorrect assumptions and data. Finally, in 1925, Edwin Hubble proved that the spiral nebulae were distant extragalactic systems using the period-luminosity relation for Cepheid variables in Andromeda (M31). In the next year, Hubble published his revolutionary work about the properties of galaxies as extragalactic systems, introducing the early version of his classification (Hubble 1926).

## 1.2 MORPHOLOGICAL CLASSIFICATION: HUBBLE SEQUENCE

The current traditional morphological classification is based on the Hubble’s monograph *The Realm of the Nebulae* (Hubble 1936). The *Hubble Sequence of Galaxies* or the “tuning-fork” diagram (see Figure 1.1) is built on the visual appearance of the galaxies, originally made on photometric plates but nowadays from digital images taken with CCD cameras. In this tuning-fork diagram, elliptical galaxies are found on the left side and spiral galaxies are found on the right side. Hubble believed (incorrectly) that there was an evolutionary transition from one type to another. Therefore, he named the left end of the diagram as “early-type” and the right end as “late-type” galaxies, presented by two branches of spiral galaxies - normal and barred spirals. The Hubble sequence is meaningful, because independent properties of the galaxies (such as total mass, luminosity, integrated colour, neutral hydrogen, total surface density, and surface density of neutral hydrogen content, luminosity function of HII regions, etc.) correlate with the morphological classes. Presently, astronomers use the *revised Hubble Sequence of Galaxies*, described by several authors – de Vaucouleurs (1974), Sandage (1975), Kormendy (1982) and van den Bergh (1998). Here, we summarize the *revised Hubble classification system* as reported in Binney & Tremaine (2008). For further explanation see also Sandage & Bedke (1994), Binney & Merrifield (1998a; Sec.4.1.1) and Longair (2008).

**(A) Elliptical galaxies:** Elliptical galaxies are large, featureless systems of primarily old stars (i.e., stars with ages comparable to the age of the Universe). They contain little to no cool gas

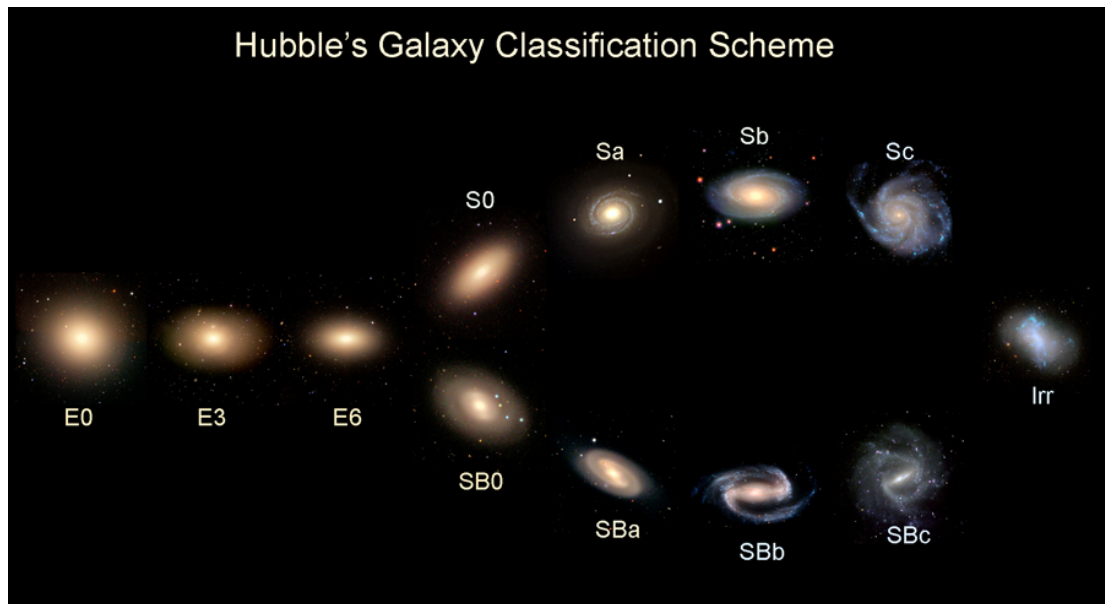


**Figure 1.1:** Hubble Galaxy Classification “tuning-fork” diagram constructed from Sloan Digital Sky Survey (credit: John Kormendy’s homepage, <http://chandra.as.utexas.edu/kormendy/a301-2010-spring.html>).

and no (or a weak) stellar disk. Their surface brightness isophotes are concentric ellipses with axis ratios ( $b/a$ ) varying between 1 and 0.3, and ellipticity values ( $\epsilon \equiv 1 - b/a$ ) between 0 and 0.7. The elliptical galaxies are indicated by the symbols E0, E1, etc., where  $E_n$  corresponds to a galaxy with axis ratio  $b/a = 1 - n/10$ . E0 galaxies are circular whereas E7 galaxies are the most elongated ellipticals with  $b/a = 0.3$ . Galaxies flatter than E7 show distinct disc and bulge structure. They are classified as lenticular (S0) rather than E. The elliptical galaxies are ranging between the most luminous galaxies known with absolute magnitude  $M_B \approx -24$  to dwarf ellipticals (dE). The surface brightness of an elliptical galaxy falls off smoothly with radius. The galaxy size is measured by using the effective radius  $R_e$  (the radius of the isophote containing the half of the total luminosity) due to the absence of sharp outer edges.  $R_e$  also correlates with the galaxy luminosity (20 kpc for a giant elliptical and 0.2 kpc for a dwarf elliptical galaxy). Most luminous ellipticals (even those with large ellipticity) show little to no rotation. The luminosities, velocity dispersions, and sizes of elliptical galaxies correlate with each other and lie on a two-dimensional surface called the *fundamental plane* (Jorgensen et al. 1996). Their masses (both luminous and dark matter) vary between  $10^7 M_\odot$  to  $10^{13} M_\odot$ , and their diameters can be a few tenths of a kiloparsec to hundreds of kiloparsecs.

**(B) Spiral galaxies:** These galaxies contain prominent discs composed of stars, gas, and dust. The discs are characterized by well-defined spiral arms emanating from the galaxy central regions. The spiral arms vary in shape, length, and prominence. The spiral pattern could be double

with a high symmetry regarding to the galaxy center or more complicated. Most spiral galaxies, like the Milky Way and M31, contain a centrally concentrated stellar system, called a bulge (or spheroidal component), whose nature is not totally understood. The bulge luminosity correlates with the luminosity of the disc, the fraction of the disc mass in gas, the color of the disc, how tightly the spiral arms are wound, etc. Based on these correlations, the Hubble classification system could be sub-divided into four classes - Sa, Sb, Sc, Sd (Sandage & Bedke 1994). From Sa to Sd, the relative luminosity of the bulge decreases, the relative mass of the gas increases, the spiral arms are loosely wound and more clumpy, where the HII regions become more prominent. Some spiral galaxies have a bar. It is an elongated, smooth stellar system that is reminiscent of a rigid paddle or stirrer rotating at the center of the galactic disc, even categorized as a triaxial bulge (Binney & Tremaine 2008). All spiral galaxies are divided into two main branches in the Hubble diagram (Hubble 1926), and thus they are “barred” (SB) or “normal” (SA) galaxies, depending on the presence or absence of a bar in the center, respectively. Here, we give a brief description of the four classes, taking into account: the openness of the winding of the spiral arms, the degree of resolution of the arms into stars, and the size of the spheroidal component or central bar relative to the disc component.

- Sa galaxies* have tight spiral arms that are unresolved into stars, and dominant bulges or bars without clear structure.
  - Sb galaxies* have more open spiral arms that are resolved into stars, and smaller bulges (spheroidal components) or bars.
  - Sc galaxies* have very open and patchy spiral arms that are resolved into star clusters and regions of ionised hydrogen. These galaxies also have very small spheroidal components. The bars in SBc galaxies are resolved into star clusters and HII regions, which are not prominent as in Sa or Sb.
  - Sd galaxies* are very late Sc spirals and have “nearly chaotic” structures.
- There are also intermediate morphological stages called Sab, Sbc, and Scd, holding the features of two main classes.

**(C) Lenticular galaxies:** The lens-like or S0 galaxies are intermediate in morphological type between ellipticals and spirals. Similar to the elliptical galaxies, they have smooth light distributions and axial ratios of  $b/a < 0.3$ , featureless appearance, no spiral structure, and little to no cool gas or recent star formation (the absence of the young stars is relevant to the absence of gas). Similar to the spiral galaxies, they contain rapidly rotating discs with an exponential surface-brightness light distribution, a bulge, and sometimes a bar. Due to the bar-like appearance of the central bulges, S0 galaxies can be also divided into “barred” and “ordinary” lenticulars (analogous to the spirals), including intermediate types too. van Gorkom (2004) suggests that the lenticulars are spirals that have been depleted of interstellar gas by interactions with the hot gas in the galaxy clusters.

**(D) Irregular galaxies:** In the Hubble classification from 1939, the irregular galaxies (Irr) are classified as lacking both dominating nuclei and rotational symmetry that can not fit to the standard galaxy types. In comparison to the spiral and elliptical galaxies, they are less luminous with less well defined spiral structure. There are two types of irregulars presented by galaxies with weak regular (Irr I) or no regular (Irr II) structure. The companion galaxies of the Milky Way, the Large and Small Magellanic clouds, are considered as prototypes of irregular galaxies. Irr galaxies include spirals or ellipticals that have been violently distorted by a recent encounter with a neighbour, and are at the last stages of merging, or are experiencing intense bursts of star formation (it could overwhelm the stellar population, determining the morphological classification). These galaxies are extremely gas-rich, where their interstellar gas masses could be more than 30% of their stellar masses. Their circular speeds are low and are linear functions of their radii with maximum speeds of around  $50\text{-}70 \text{ km s}^{-1}$  near the edge of the disc. This rotation profile is very different from those of spirals, where the circular velocity is nearly flat and reaches  $300\text{-}400 \text{ km s}^{-1}$ .

### 1.3 STRUCTURE OF DISC GALAXIES

Galaxy discs are best described as flattened triaxial ellipsoids with exponential surface brightness profiles (Freeman 1970). Although discs are generally considered circular, observations suggest they are slightly elliptical with  $b/a \lesssim 0.9$  (Lambas et al. 1992; Ryden 2004). Additionally, discs have low vertical-to-radial axial ratios of 0.15 to 0.25, indicating that they are mostly thin. (Holmberg 1950; Sandage et al. 1970a, see Fig. 1.2).

**Thin disc:** The thin disc<sup>1</sup> is the defining component of disc galaxies, which contain stars, star clusters, gas and dust. They are confined into the galaxy's plane of rotation and drive an active star formation, especially in the spiral arms (Banerjee & Jog 2012). For this reason, stars in the thin disc tend to be relatively young and metal-rich compared to stars in the thick disc or the halo (Marsakov et al. 2011). Thin discs also contain the majority of the baryonic material in spiral galaxies (Gilmore & Reid 1983).

**Thick disc:** The first detections of a thick disc component in galaxies were made by Burstein (1979) and Tsikoudi (1980) as an exponential excesses of light a few thin disc scale heights above the midplane of edge-on lenticular galaxies. In our Galaxy, Gilmore & Reid (1983) distinguished two vertically exponential components - thin and thick disc, using star counts at high Galactic latitudes. Moreover, studies show most disc galaxies contain thick discs (e.g., Dalcanton & Bernstein 2002; Seth et al. 2005; Yoachim & Dalcanton 2005; Comerón et al. 2011). Furthermore,

---

<sup>1</sup>Definition from the online SAO Encyclopedia of Astronomy - COSMOS; <http://astronomy.swin.edu.au/cosmos/>

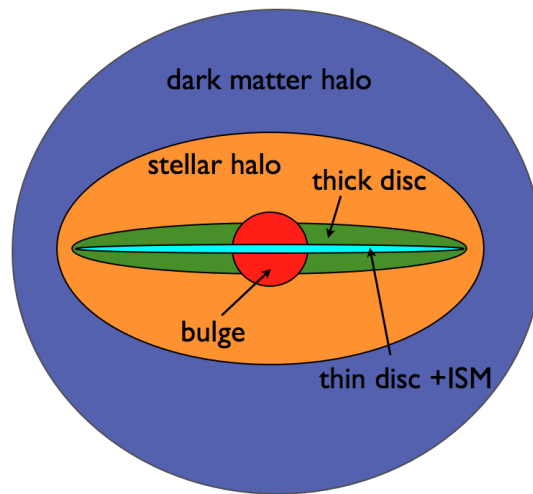


**Figure 1.2:** Main components of a spiral galaxy, including a spheroidal bulge (red), a thin disc with stars and interstellar medium (ISM; bright blue), a thick disc of older stars (green), a spheroidal low-density stellar halo (yellow), and an extended spheroidal dark matter halo (dark blue).

Yoachim & Dalcanton (2006) studied a large sample of edge-on galaxies and found that the ratio of stars in the thick disc to thin disc depended on the luminosity and circular velocity of the galaxy. They calculated that the ratio is  $\sim 10\%$  for large spirals like the Milky Way and increases to  $\sim 50\%$  for the smallest disc systems.

Compared to the thin disc, the thick disc has higher velocity dispersions, lags in its net rotation (Chiba & Beers 2000), older stars with lower metallicities (Majewski 1993), and enhanced  $[\alpha/\text{Fe}]$  ratios (Bensby et al. 2005; Reddy et al. 2006; Fuhrmann 2008). Many studies used different spatial, kinematic, or chemical criteria to place stars into either the thin disc or thick disc populations (Fuhrmann 2008; Schönrich & Binney 2009b; Lee et al. 2011). Recent studies, however, show that thin and thick disc components lack clear distinctions (Bovy et al. 2012a,b; Liu & van de Ven 2012).

Previous theoretical studies used many different models to explain the formation of the thick disc, such as the accretion of stars from disrupted satellites (Statler 1988; Abadi et al. 2003), the thickening of a pre-existing thin disc by minor mergers (Quinn et al. 1993; Villalobos & Helmi 2008), triggered star formation due to a gas-rich merger (Jones & Wyse 1983; Brook et al. 2004, 2005; Bournaud et al. 2009), the radial migration of stars (Schönrich & Binney 2009a; Loebman et al. 2011) due to corotation resonances with transient spiral structure (Sellwood & Binney 2002), bar structure (Minchev & Famaey 2010), or orbiting satellites (Quillen et al. 2009).

One of the scenarios for disc formation considers that baryons cool and collapse within hierarchi-

cally assembled dark matter haloes. As such, angular momentum is transferred to the baryonic component and leads to the formation of a rotationally supported thin structure (Fall & Efstathiou 1980a). This model is able to reproduce well many observational properties of disc galaxies (e.g., Dalcanton et al. 1997; Mo et al. 1998; van den Bosch 1998, 2000). Detailed N-body simulations, however, showed that when the dissipative effects of gas are not considered this scenario results in disc destruction (Toth & Ostriker 1992). Additionally, hydrodynamical simulations produce discs that are too small and too centrally concentrated due to excessive angular momentum exchanges between the gas and the dark matter haloes (Navarro & Steinmetz 1997). One solution for these problems and producing of realistic discs is to include strong feedback mechanisms from different sources, e.g., from star formation or supernovae explosions (e.g. Governato et al. 2010).

**Bulge:** Galactic bulges are believed to form via early mergers at high redshifts or during secular evolution, such as the presence of a bar brings slowly the gas to the center of the galaxy and form a spheroid (e.g., Raha et al. 1991; Debattista et al. 2004, 2005), see Fig.1.2. This defines two different types of bulges: classical bulges and pseudobulges.

Classical bulges are thought to form via mergers (Naab & Trujillo 2006; Hopkins et al. 2010), where spheroids are produced by violently destroying discs. These bulges have steep increases in density toward their galaxy centers with high Sersic indices ( $n > 2$ ) and smooth, nearly elliptical surface brightness isophotes (e. g., Fisher & Drory 2008). They rotate rapidly as oblate spheroidal stellar systems that have isotropic velocity dispersions flattened mainly by rotation (e.g., Kormendy 1982).

Conversely, pseudobulges are thought to originate from collapsing disc material via secular evolution (see a review by Kormendy & Kennicutt 2004a) induced by spiral structures or bars (Combes & Sanders 1981; Pfenniger & Norman 1990; Combes & Elmegreen 1993; Debattista et al. 2004; Athanassoula 2005). They have disc-like density profiles (Carollo et al. 1997, 1998; Carollo & Stiavelli 1998) and kinematics (Kormendy 1993) with low Sersic indices ( $n < 2$ ). Carollo et al. (2007) showed that pseudobulges also have younger stellar populations than classical bulges, and that only massive late type spirals tend to have older pseudobulges.

**Stellar halo:** A stellar halo<sup>2</sup> is spherical population of stars and globular clusters thought to surround most disc galaxies and the cD class of elliptical galaxies. The halo represents only  $\sim 1\%$  of the total galaxy stellar mass with no net rotation and almost entirely supported by velocity dispersion. The stellar halos of spiral galaxies are very difficult to observe, because they are very faint. It is necessary to go  $\sim 10$  magnitudes below the night sky level to reach  $\sim 30$  mag arcsec<sup>-2</sup> (Zibetti et al. 2004; Jablonka et al. 2010). The halo stellar populations reflect how

---

<sup>2</sup>Definition from the online SAO Encyclopedia of Astronomy - COSMOS; <http://astronomy.swin.edu.au/cosmos/>

stellar populations and masses were assembled in the earliest epochs of the galactic formation. Most studies examine the stellar halo populations of the Milky Way (e.g., Majewski et al. 1999; Belokurov et al. 2007; Rocha-Pinto et al. 2003; Jurić et al. 2008; Grillmair 2006; Vivas & Zinn 2006; Bell et al. 2008), but several studies probe the stellar halos of other spiral galaxies (e.g., Sackett et al. 1994; Lequeux et al. 1998; Mouhcine et al. 2005).

The two main mechanisms of halo formation and evolution are based on the chemical, kinematic, and structural properties of the Milky Way halo stars. The first mechanism is monolithic collapse, where the stellar halo forms from the rapid collapse of a proto-Galaxy, within a time on the order of the dynamical timescale (Eggen et al. 1962). In the second method, the halo forms within a longer timescale by accretion of proto-Galactic fragments that experienced separate pre-enrichment (Searle & Zinn 1978). Due to identified gas streams in halos of different galaxies (Yanny et al. 2000; Ibata et al. 2001; Peng et al. 2002), the halo populations may be affected by infall/accretion of dwarfs (Ferguson et al. 2002).

Unfortunately, neither mechanism can explain the observed properties of the Milky Way halo stars (Norris & Ryan 1991; Beers & Sommer-Larsen 1995; Chiba & Beers 2000). Additionally, a comparison between the Milky Way and M31 (Durrell et al. 2001) halo star properties shows that the Milky Way halo is atypical. The halos of spiral galaxies seem to be quite diverse (Bekki & Chiba 2001).

## 1.4 STRUCTURE OF ELLIPTICAL GALAXIES

Elliptical galaxies dominate the denser regions and the mass budget of the Universe, from rich clusters to small groups, with only a small fraction of isolated galaxies being ellipticals (as first noted by Hubble & Humason 1931). Those galaxies are generally considered as the simplest dynamical systems possessing a regular and smooth shape. Elliptical galaxies do not present the striking features found in spirals, such as prominent discs and spiral structure, and contain a small quantity of gas and dust (see Bayet et al. 2013). Consequently, there is little evidence for ongoing star formation, with no HII regions or young star clusters.

In reality, elliptical galaxies possess a wealth of dynamics and shapes. Detailed characterization showed that they are not only simply axisymmetric objects (oblate or prolate), but also complex triaxial stellar systems (see Fig.1.3). For example, Peletier et al. (1990) observed that isophotes of massive elliptical galaxies are, in general, not true ellipses. These deviations from purely elliptical isophotes appear only at the levels of at most a few percent a pure elliptical isophote; but are well-determined and significant.

Generally, the type of deviation are characterized in the terms of *boxiness* (when the isophotes

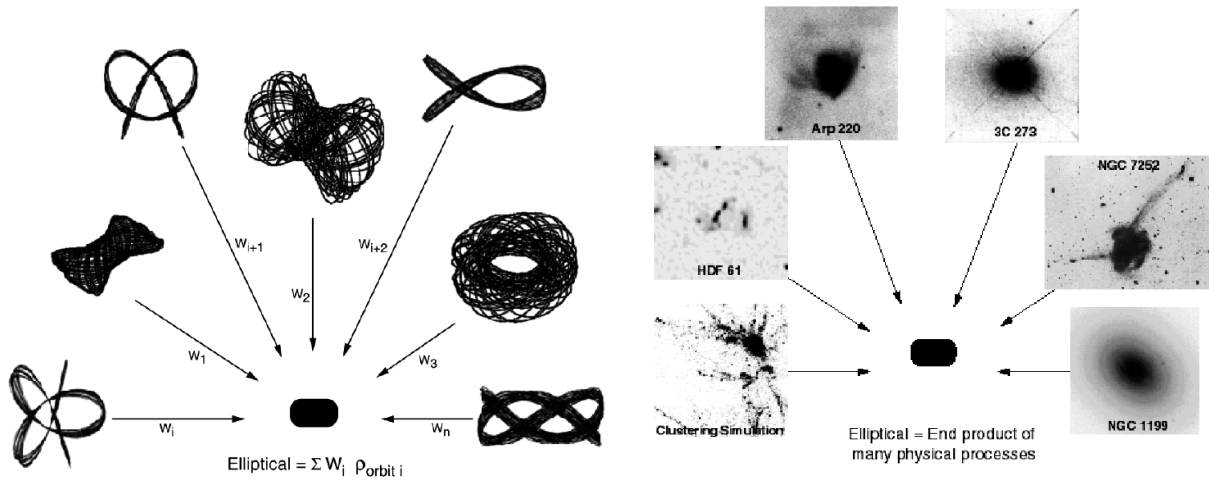


**Figure 1.3:** *Left:* Dynamical look at an elliptical galaxy as a sum of the density distributions corresponding to orbits of various kinds, each weighted by the relative number of stars  $W_i$  that populate it. *Right:* Observational look at an elliptical galaxy as the result of physical processes of formation and evolution (Credit images: Kormendy 1999).

are thinner than an ellipse, with squarer ends), and *discy-ness* (when the isophotes fatter than an ellipse, with more pointed ends). Those deviation are important and some observed properties of elliptical galaxies are found to vary depending on the type and strength of the distortion. For example, luminous ellipticals are often boxy, whereas average sized ellipticals are discy. Boxy galaxies are powerful sources of X-ray and radio emission, while discy galaxies can be several orders of magnitude weaker (Bender et al. 1989).

From the kinematic point of view, the discy-ness of the galaxies appears to be connected with the rotation rate,  $V/\sigma$ . A discy galaxy is generally accompanied by unitary values of  $V/\sigma$ , with small minor axis rotation, implying a rotationally-supported object as in the case of a disc. In boxy galaxies the value of  $V/\sigma$  is observed to be less than unity, implying that rotation is dynamically unimportant in these objects. Those objects present instead a significant rotation along the minor axis, suggesting triaxiality.

Isophote distortions also carry an important information on the formation and nature of elliptical galaxies. The global origin of these deviations is still unclear but simulations have shown that they likely depend on the evolutionary history of the systems. Unequal-mass mergers have been observed to produce rotationally supported ellipticals with discy isophotes and small minor axis rotation. Instead, equal-mass mergers result into anisotropic, slowly rotating systems with preferentially boxy isophotes and large minor axis rotation (e.g. Naab et al. 1999, Bendo & Barnes 2000).

The boxiness or the discy-ness of an elliptical galaxy is quantified in terms of fluctuations in intensity along the best-fitting ellipse as a Fourier series:

$$I(\phi) = I_0 + \sum_{n \geq 3} A_n \sin n\phi + B_n \cos n\phi. \quad (1.1)$$

where  $I(\phi)$  is the intensity fluctuation,  $I_0$  is the intensity of the best-fitting ellipse,  $\phi$  is the angle measured from the major-axis of that ellipse, and A and B are coefficients describing the amplitude of the intensity deviations for a given order  $n$ . The fluctuations are therefore described in term of the dimensionless coefficient  $C4 = B_4/I_0$ . If the isophote is discy, the  $C4$  term is positive, while a negative  $C4$  value implies a boxy isophote (e.g., [Bender et al. 1988](#)). Lenticular galaxies S0 can be seen as the continuation of the discy-ness trend of the elliptical galaxies.

## 1.5 REVISED HUBBLE SEQUENCE FROM ATLAS<sup>3D</sup> SURVEY

In the tuning-fork diagram of galaxies ([Hubble 1936](#)), the S0 galaxies are consider as the transition systems between the spiral and elliptical galaxies ([de Vaucouleurs 1959](#); [Sandage 1961](#)).

[Spitzer & Baade \(1951\)](#) first reported that the S0 morphology is more various than Hubble expected, and represent series of forms that are parallel to those of normal spirals, such as Sa, Sb, Sc. S0 galaxy series contain no obscuring matter and therefore they are unable to develop spiral structure. Indeed, S0s appear like spiral galaxies without arms ([Sandage et al. 1970b](#)). This hypothesis was strongly supported by [van den Bergh \(1976\)](#), who noticed that normal spirals, which exhibit a strong display of Population I stars, might occur from parallel sequences of S0 galaxies.

[Cappellari et al. \(2011a\)](#) first study the kinematic morphology-density relation of 260 early-type galaxies (ETGs) as part of ATLAS<sup>3D</sup> survey. They propose a revision of the tuning-fork diagram, replacing the lenticular and elliptical galaxies with fast and slow rotators, respectively. Further, they consider the large variation in the bulge sizes of the fast rotators in contrast to the Hubble diagram.

Their classification utilizes the specific angular momentum parameter defined by [Emsellem et al. \(2007\)](#) as

$$\lambda_R \equiv \frac{\langle R|V| \rangle}{\langle R \sqrt{V^2 + \sigma^2} \rangle} = \frac{\sum_{n=1}^N F_n R_n |V_n|}{\sum_{n=1}^N F_n R_n \sqrt{V_n^2 + \sigma_n^2}} \quad (1.2)$$

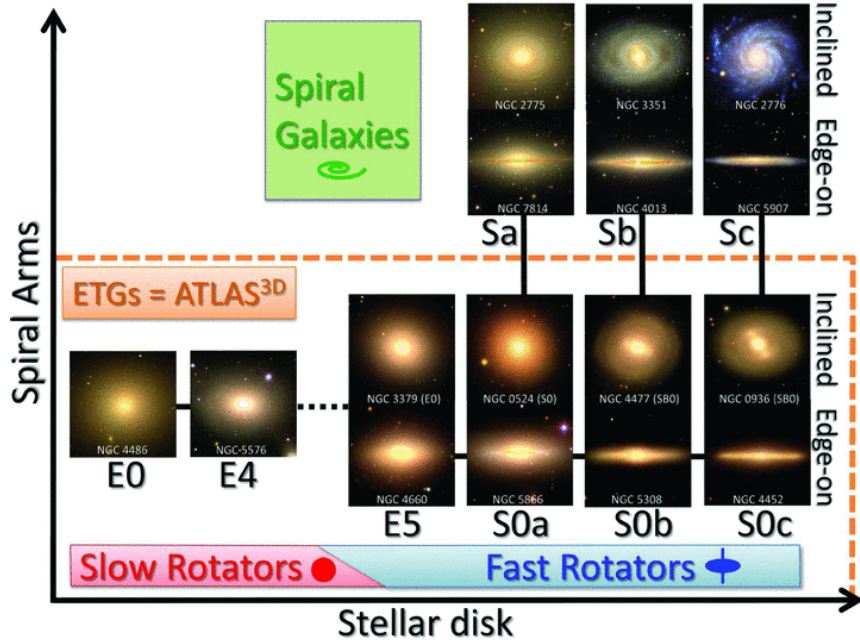


**Figure 1.4:** Morphology of nearby galaxies from the ATLAS<sup>3D</sup> parent sample. The early-type galaxies (E/S0) can be divided in two main types: fast and slow rotators depending on their kinematics, and particularly, their specific angular momentum parameter defined in Emsellem et al. (2007). Fast rotators are intrinsically flatter than  $\epsilon \gtrsim 0.4$  and span the same full range of shapes as spiral galaxies, including very thin discs. The slow rotators are rounder than  $\epsilon \lesssim 0.4$ . (Credit image: Cappellari et al. 2011a).

where  $F_n$  is the flux contained inside the  $n$ th Voronoi bin and  $V_n$  and  $\sigma_n$  the corresponding measured line-of-sight mean stellar velocity and velocity dispersion. This criterion is based on the classification of the velocity maps presented in Krajnović et al. (2011) and introduced by Emsellem et al. (2011). The slow rotators are therefore considered as those having  $\lambda_R(R_e) < 0.31 \sqrt{\epsilon}$ , where  $R_e$  is the effective (half light) radius and  $\epsilon$  is the ellipticity within  $1R_e$ . The kinematic classification eliminates the discussed high fractions of E/S0 misclassification that affect standard morphological classification due to photometry alone.

S0s or flat ellipticals with discy isophotes appear morphologically equivalent to the edge-on fast rotators. All the galaxies classified as ‘discy’ ellipticals E(d) by Bender et al. (1994) belong to the fast rotator class. In contrast to E(d) and S0 galaxies, the fast rotators can be identified from integral-field kinematics even if they are face-on (Cappellari et al. 2007; Emsellem et al. 2007). They form a parallel sequence to spiral galaxies as already emphasized for S0 galaxies by van den Bergh (1976), who proposed the distinction between S0a–S0c. Fast rotators are intrinsically flatter ( $\epsilon \gtrsim 0.4$ ), spanning in a range of shapes similar to those of spiral galaxies. Nevertheless, very few Sa galaxies display spheroids as large as those of E(d) galaxies. The slow rotators are rounder with  $\epsilon \lesssim 0.4$  (see Fig. 1.4).

Williams et al. (2009) suggests that the stellar dynamics of the fast rotators appear to be indistinguishable from that of spiral galaxies of comparable flattening. Both classes are well described by the simple anisotropic Jeans models of Cappellari (2008). This further confirms the structural similarity of the two classes of objects (within the limit of the small studied sample). From a purely observational point of view the difference between fast rotator ETGs and spiral galaxies is their cold gas content, which is significantly lower than one in the spiral galaxies, and also in their dust content, visible as spiral arms in optical photometry (Young et al. 2011).

S0 galaxies tend to have bulge fractions comparable to that of Sa galaxies, but larger than later spiral types. The same is expected to be for fast rotators, which contain large fractions of S0 galaxies. This was quantified by Simien & de Vaucouleurs (1986) and Laurikainen et al. (2010).

There are several mechanisms (see Boselli & Gavazzi 2006 for review) that can transform spiral galaxies into fast rotators or reduce spiral formation via cold accretion (Dekel et al. 2009). For example, gravitational heating by minor merging might suppress star formation (Khochfar & Ostriker 2008; Johansson et al. 2009) or quenching produced by galaxy harassment (Moore et al. 1996, 1999). Further, reduction of star formation can result from morphological quenching (Martig et al. 2009) caused by the thickening of the discs and growth of the bulges by secular evolution or during close encounters and minor mergers (Kormendy & Kennicutt 2004b; Debattista et al. 2006). (Dressler 1980) show that the negative trend between the amount of gas and the bulge fraction predicted by these processes is in agreement with the observations. The presence of thick discs in S0s (Burstein 1979) are expected to form via dynamical disturbances (Read et al. 2008).

## 1.6 DARK MATTER ON GALACTIC SCALES

The Dutch astronomer Jan Oort (Oort 1932a,b) first used the term ‘dark matter’, although in a different context than used today. He used the motion of stars above the galactic plane to discuss the mass density in the disc of Milky Way. Oort found using kinematic data that only about one-third of the dynamically inferred mass was present in bright visible stars. In his context of dark matter, Oort referred to all low-mass stars and undetected component of the interstellar medium (i.e., the gas and the dust between stars). He suggested that these forms of undetected matter would make the observed mass consistent with the dynamical mass. Decades later, from the observation of galaxy rotational curves, it was clear that low-mass stars and the interstellar medium could not break the discrepancy between the visible mass and the dynamical mass (Bosma 1978; Rubin & Ford 1983).

### 1.6.1 DARK MATTER DISCOVERY

One year later, Zwicky (1933) measured the radial velocities of several galaxies in the Coma cluster and applied the virial theorem to them. He noticed that the galaxies seemed to move too fast for the amount of the visible matter in the cluster, indicating that the cluster should have dispersed. Thus, Fritz Zwicky first proposed the current definition of dark matter, as the dominant component of the bound astronomical systems like galaxies and cluster of galaxies that is detectable only by its gravitational influence on these systems. Zwicky's hypothesis was fully accepted only 40 years later (Bosma 1978; Rubin & Ford 1983). By 1970 radio astronomy

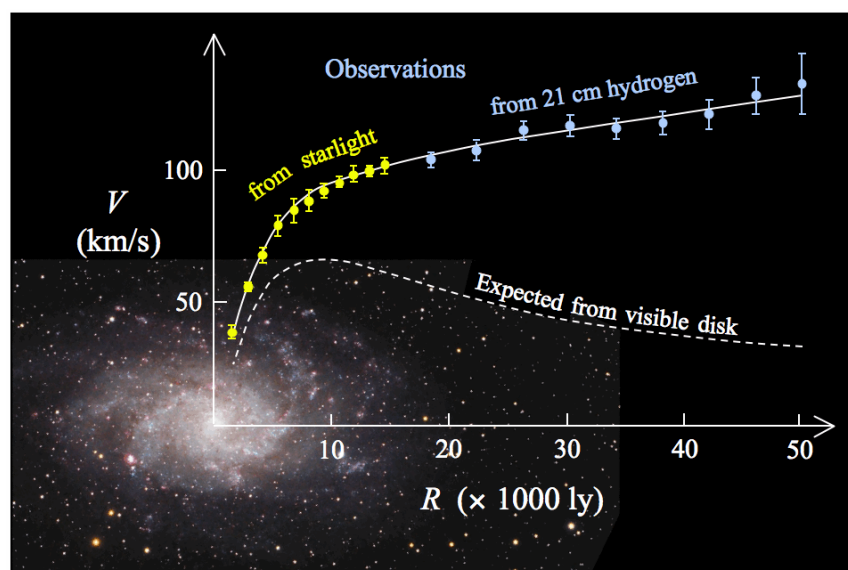


**Figure 1.5:** The rotation curve for M33 continues to rise well beyond the optical disc as measured by HI. (Credit: Whittle's online lectures:

[http://www.astro.virginia.edu/class/whittle/astr553/Topic05/t5\\_HI\\_M33.html](http://www.astro.virginia.edu/class/whittle/astr553/Topic05/t5_HI_M33.html).)

became a major tool for exploring galactic and extragalactic astronomy. Measurements of the 21-cm line from neutral hydrogen (HI) trace the mass distribution of the Milky way and many other spiral galaxies. HI-derived galaxy rotational curves extended to almost twice the optical radius of the galaxy and demonstrated flat profiles. Optical rotational curves could be derived only within the brightest regions of the galaxy, and thus, not enough to confirm the need of additional mass. The radio observations, however, demonstrated the necessity of non-baryonic dark matter in the outer parts of spiral galaxies (e.g., Bosma 1978, 1981a,c; Rubin et al. 1978a,b; Rubin & Ford 1983). The phenomenology of flat rotation curves went from dubious result of radio astronomers to an accepted view of spiral-galaxy kinematics. In galaxy rotational curves, the velocity rises to a maximum at a radius of a few kiloparsecs, and then it plateaus at constant value well beyond the optical disc (see Fig. 1.5). The knowledge about spiral galaxies has changed dramatically. These

observations were completely consistent with previous theoretical work by Ostriker & Peebles (1973). They proposed that the rotationally-supported disc galaxies require a massive spherical dark halo to stabilize the disc. This dark halo extends beyond the visible disc and increases the mass-to-light ratio in the outer regions of the galaxies.

According to the modern large-scale simulations, the Universe is dominated by dark matter (Springel et al. 2005). Galactic evolution is driven by the formation of the dark matter halos. For example, their gravitational potential shapes galaxies by gas cooling and condensation. But the exact mechanism for the hierarchical assembling of the stellar masses is still undiscovered (White & Rees 1978). The observed stellar mass is usually estimated from the light of the galaxies times the assumed value of the mass-to-light ratio coming from stellar populations (Kuntschner 2000; Sánchez-Blázquez et al. 2007). The dynamical mass of the galaxies comes from the gravitational potential, constructed from the velocity and velocity dispersion fields of the galaxies. Then the residual of the inferred stellar mass and the dynamical mass gives the dark matter content.

Thus, the mass distribution in disc systems is a key to understand galaxy formation. Currently, a wealth of observations allow one to study the properties of the baryonic components in the galaxies. The rotation curves, one of the best tracers of their mass, do not show any Keplerian fall-off and do not match the distribution of baryonic (stellar and gaseous) matter. This implies an additional invisible mass component (Rubin et al. 1980; Bosma 1981b; Persic & Salucci 1988).

## 1.6.2 SHAPE OF THE ROTATION VELOCITY CURVES

The shape and the amplitude of the rotation curves reflect the mass distribution of luminous and dark matter in galaxies, and is the scope of many studies (e.g., Zasov & Kyazumov 1983; Corradi & Capaccioli 1990; Swaters et al. 2009; Martinsson et al. 2013). Rubin et al. (1985) pointed out that, within a same morphological type, spiral galaxies show a progression of central velocity gradients and maximum rotation velocities with increasing absolute luminosities.

Similarly, in a large sample of Sb-Sc galaxies, Sofue et al. (1999) observe a steep nuclear rise of their rotational velocity and conclude that is a universal property for massive Sb and Sc galaxies, regardless of the existence of a bar and morphological peculiarities. However, less massive galaxies tend to show a rigid-body rise.

They classify the observed rotation curves into the following three types, according to their behavior in the central regions. (see Fig.1.6) :

*Central Peak Type:* Rotational velocity attains a sharp maximum near the center at  $R \sim 100\text{--}500$  pc, followed by a dip at  $\sim 1$  kpc, then by a broad maximum of the disc component (e.g., Milky Way).

*No-Central Peak Type*: The rotational curve rises steeply at the center, followed immediately by a flat part.

*Rigid-Body Type*: The rotational velocity increases mildly from the center in a rigid-body fashion within the central 1 kpc. This type is rather the exception, and is found in less massive Sc-type galaxies and it has been already reported by Casertano & van Gorkom (1991).

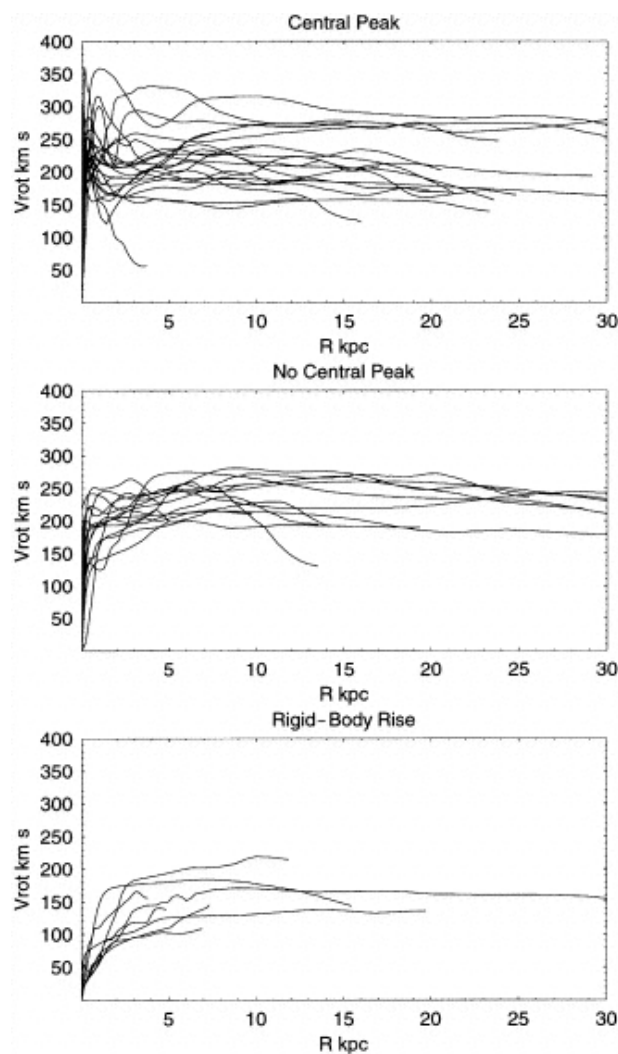


**Figure 1.6:** Classification of rotation curves of spiral galaxies into three types according to the central behavior. (Credit: Sofue et al. 1999)

## 1.7 SCALE RADIUS AND DISK ROTATIONAL VELOCITY. MAXIMAL DISC THEORY

Maximum rotational velocity is an indicator of the total mass of a galaxy (e.g., Persic et al. 1996). The disc mass is also related to the optical scale radius ( $h$ ), because the mass-to-luminosity ratio would not vary significantly inside the disc.

Dark matter halos in rotation curve decompositions have been modeled traditionally as isothermal spheres with a homogeneous core. Because these multi-component fits to the rotation curve data are not unique, it appeared sensible to add a constraint, such as the maximum disc or minimum dark matter solution (Sancisi 1985; Carignan & Freeman 1985), to obtain a unique solution.

Maximum disc models imply that for bright spirals, the stellar disc and bulge are the dominant mass components inside two exponential scale lengths. An operational definition for the maximum disc hypothesis is that the stellar disc provides  $85\% \pm 10\%$  of the total rotational support of the galaxy at  $R_{disc} = 2.2h$  (Sackett 1997). The lower boundary accounts for bars and massive bulges which reduce the contribution of the disc to the overall rotation curve. The upper boundary of this ratio is kept at 95% in order to prevent hollow cores in the dark halo. Still, the validity of the maximum disc hypothesis has yet to be demonstrated unequivocally in external galaxies because of our inability to constrain  $(M/L)_{disc}$ , independent of mass models.

In Figure 1.7 (left-hand side), Pizagno et al. 2005 compare the maximum stellar velocity  $V_{2.2,*}$  with dynamical velocities  $V_{2.2}$  at  $R = 2.2h$ , where  $h$  is the scale radius of the 81 disc external galaxies. Their relation (solid line) differs from the relation  $V_{*,2.2} = 0.85V_{2.2}$  expected for maximal discs (Sackett 1997).

Bovy & Rix (2013) compare Milky Way with the sample of Pizagno et al. (2005), shown in Fig. 1.7 (right-hand side). They study how the scale lengths of the discs, i.e. the compactness of the galaxies, relates to the ratio of the  $V_{*,2.2}/V_{2.2}$ . The Milky Way falls along the general trend defined by these external galaxies, except that its scale length appears short compared with similar external galaxies.

## 1.8 INNER DYNAMICAL MASS ACROSS GALAXY MORPHOLOGY

Galaxy simulations that aim to reproduce the observed properties of galaxies and their dark matter halos over a wide range of masses have become complex, and especially in their inner parts (Brook et al. 2012; Governato et al. 2012; Di Cintio et al. 2014; Vogelsberger et al. 2013). Kuzio de Naray & McGaugh (2014) investigate the inner mass scalings across galaxy morphology in

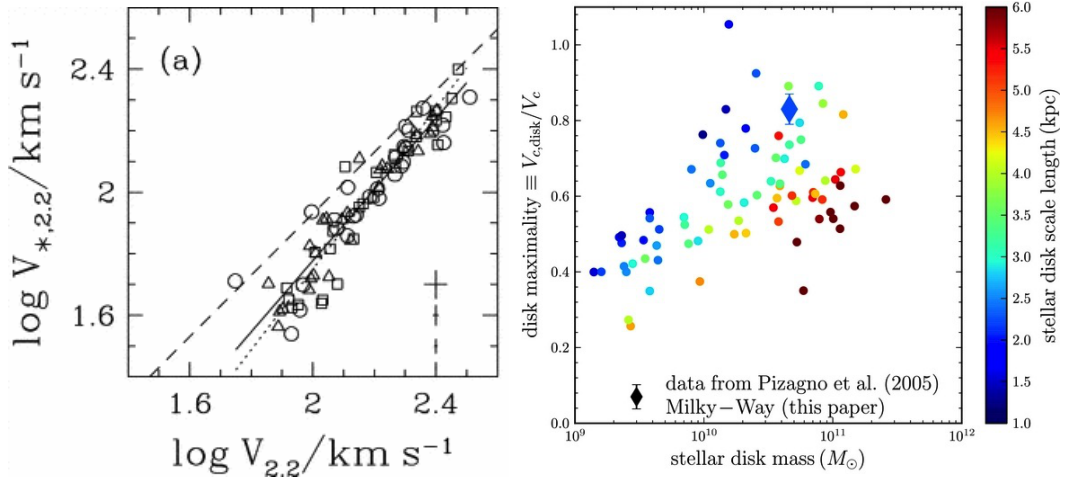


**Figure 1.7:** *Left:* Comparison of the rotation stellar velocity for each galaxy’s components  $V_{*,2.2}$  to the dynamical mass  $V_{2.2}$ . Solid line shows the fit to the data, while dashed indicate the relation  $V_{*,2.2} = 0.85V_{2.2}$  expected for maximal discs (Sackett 1997), (Credit: Pizagno et al. 2005).

*Right:* The Milky Way’s disc properties compared to 81 external galaxies from Pizagno et al. (2005). Relation between stellar mass and the disc’s contribution to the rotational velocity at 2.2 scale lengths (the extent to which the disc is maximal). Points are color-coded by the radial scale length. (Credit: Bovy & Rix 2013)

order to obtain better constraints on the stellar and dynamical masses of galaxies.

To do this, they collect data for a sample of 50 dispersion- and 61 rotation-supported systems. The dispersion-supported systems are Local Group dwarf spheroidal (dSph) galaxies with measured half-light radii and stellar velocity dispersions. The data are taken from Walker et al. (2007), McConnachie (2012) and Collins et al. (2013).

They probe the total stellar mass  $M_{\text{stars}}$  as a function of the  $M_{\text{total}}$  in 500 pc for combined dSph and disc galaxy samples. Kuzio de Naray & McGaugh (2014) also find that  $M_{\text{total}}$  increases very slowly over many orders of magnitude in the other parameters. There is a smooth transition between dispersion-supported systems and rotation-supported systems.  $M_{\text{total}}$  increases from a few  $\times 10^6 M_\odot$  for the lowest luminosity dSph galaxies to  $\sim 10^8 M_\odot$  for Sb-Sc type disc galaxies in the sample (see Fig. 1.8).

They find a gradual trend for the inner dynamical mass to increase with total stellar mass:  $\text{Log}M(< 500) = 0.16\text{Log}M_{\text{stars}} + 6.19$  without significant scatter, where the majority of galaxies fall within 0.5 dex of the relation. Therefore the dynamical masses enclosed at 500 pc is similar for galaxies with different morphology, internal motions (pressure support versus rotational support), different primary baryonic mass components (stellar mass versus gas mass), and different physical sizes. The sudden increase in central mass is interpreted as dominant stellar bulges.

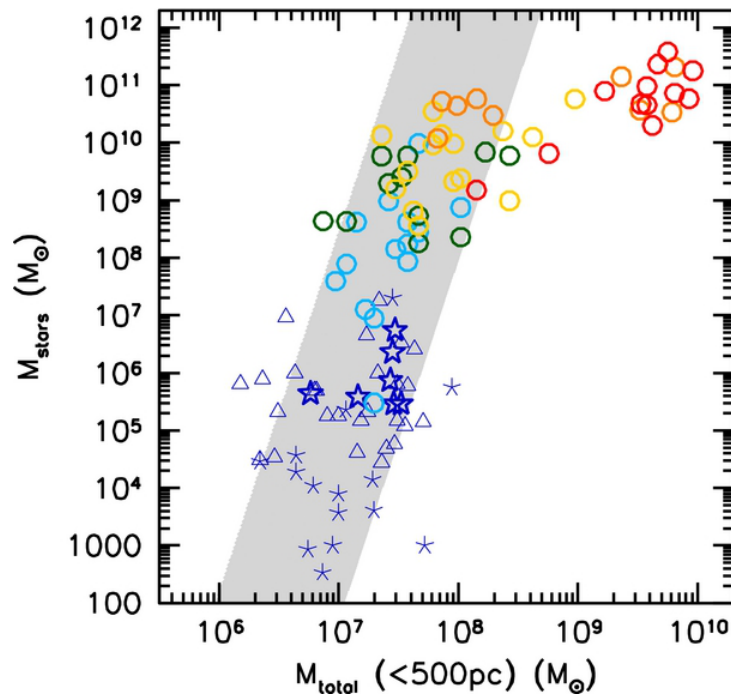


**Figure 1.8:** Total stellar  $M_{stars}$  against total dynamical mass  $M_{total}$  (stars+gas+dark matter) inside 500 pc plotted. Dispersion-supported dSph systems are plotted as dark blue stars. Rotation-supported disc galaxies are plotted as open circles, with the following color/galaxy-type combinations: red/S0-Sa, orange/Sb-Sbc, yellow/Sc-Scd, green/Sd-Sdm, and light blue/Sm-Irr. The relation in the top panel between the total inner dynamical mass and total stellar mass is  $\text{Log}M(< 500) = 0.16\text{Log}M_{stars} + 6.19$  with the width of the gray band set to 1 dex for illustration. The sudden increase in central mass is associated with dominant stellar bulges. (Credit: Kuzio de Naray & McGaugh 2014)

Early-type galaxies are probably dominated by stars in their central regions (Noordermeer & van der Hulst 2007) and their mass models often show an inner peak in the rotation curve due to the presence of bulge (Sofue et al. 1999). A subsequent peak might occur in the outer parts of galaxies that is usually attributed to either the disc or the dark matter halo. However, a dark matter halo cannot produce both peaks.

The observed difference in the inner mass between early- and late-type spirals in the studied sample of Kuzio de Naray & McGaugh (2014) might be due to possible distinct bulge formation mechanisms. Early-type spirals are efficient in forming lots of stars into a small radius. Perhaps these are classical  $r^{1/4}$  (Davies & Illingworth 1983a) bulges built by mergers, or cold flows are more efficient at delivering baryons to small radii in these massive galaxies (Dekel et al. 2009). Contrarily, the secular evolution of the disc galaxies might increase the central density of late-type galaxies (Athanasoula 2005).

## 1.9 GALAXY FORMATION: RECENT SIMULATIONS

### 1.9.1 STELLAR-TO-HALO MASS RELATION

Recent simulations of [Moster et al. \(2010\)](#) become a milestone in the recent galaxy formation theory. Their work provides a link between the luminous mass of the galaxies and dark matter halo properties through galaxy's star formation efficiency.

They derived a stellar-to-halo mass (SHM) relation between the stellar mass of a galaxy  $m$  and the mass of its dark matter halo  $M$ . [Moster et al. \(2010\)](#) also show that the observed galaxy mass function is steeper for high masses and shallower for low masses than the one derived from the halo mass function. If the SHM ratio is constant there will be too many galaxies at the low and high mass end. Therefore the actual SHM ratio ( $m/M$ ) is not constant. It increases with increasing mass, reaches a maximum and then decreases again. The authors adopt a parametrization, which similar to the one in [Yang et al. \(2003\)](#):

$$\frac{m(M)}{M} = 2 \left( \frac{m}{M} \right)_0 \left[ \left( \frac{M}{M_1} \right)^{-\beta} + \left( \frac{M}{M_2} \right)^{\gamma} \right]^{-1}, \quad (1.3)$$

where  $(m/M)_0$  is the normalization of the stellar-to-halo mass ratio,  $M_1$  is a characteristic mass and the SHM ratio is equal to  $(m/M)_0$ . The two slopes  $\beta$  and  $\gamma$  indicate the behaviour of  $(m/M)$  at the low- and high-mass ends, respectively. Both slopes are expected to be positive, but not restricted to be so and therefore the SHM relation is not necessarily monotonic. They use the best fit parameters from the stellar-to-halo mass fitting procedure for the Equation 1.3, where  $\log(M_1) = 11.884M_\odot$ ,  $(m/M)_0 = 0.0282$ ,  $\beta = 1.057$  and  $\gamma = 0.556$ . The SHM relation of [Moster et al. \(2010\)](#) is shown in Fig. 1.9. The shape of the SHM relation is influenced by several different physical processes that prevent the gas in the dark matter halo from cooling and forming stars, where the contribution of each process varies for different mass systems. For example, feedback from supernova-driven winds can be very strong in low-mass galaxies (e.g., Scd-Sd) that can easily expel large amounts of gas from haloes with low escape velocities (e.g., [Larson 1974](#); [Dekel & Silk 1986](#); [Oppenheimer & Davé 2008](#); [Puchwein et al. 2012](#)).

Additionally, the amount of cooled gas also can be reduced due to a UV and an X-ray background ([Navarro & Steinmetz 1997](#); [Gnedin 2000](#); [Benson et al. 2002](#); [Hambrick et al. 2011](#)) and cosmic rays ([Jubelgas et al. 2008](#); [Wadepuhl & Springel 2011](#)). For different halo masses, these effects have different efficiencies such that the low-mass slope of the SHM relation can change at the halo mass, where the two processes cross.

Star formation efficiency in massive haloes (e.g., giant ellipticals) is thought to be lowered by feedback from active galactic nuclei (AGN; [Springel et al. 2005](#); [Bower et al. 2006](#); [Croton et al.](#)

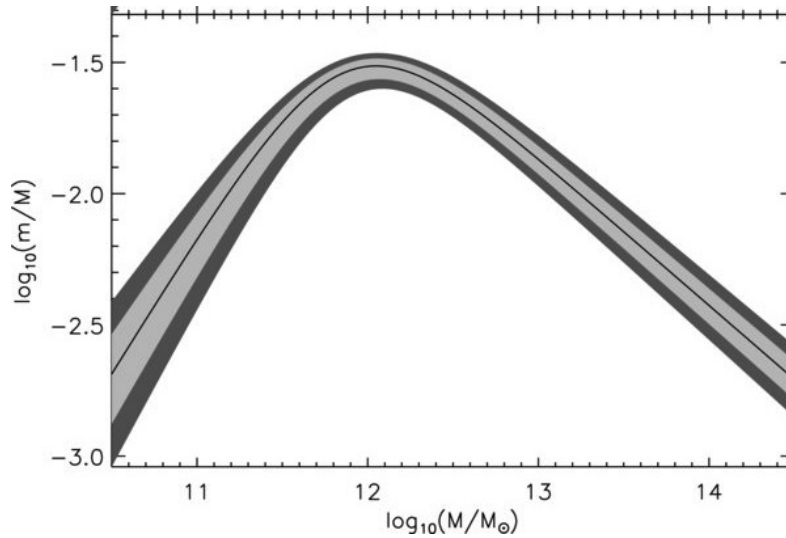


**Figure 1.9:** Derived relation between stellar mass and halo mass. The light shaded area shows the  $1\sigma$  region while the dark and light shaded areas together show the  $3\sigma$  region. The upper panel shows the SHM relation, while the lower panel shows the SHM ratio. (Credit: Moster et al. 2010)

2006; Somerville et al. 2008; Hambrick et al. 2011; Teyssier et al. 2011; Martizzi et al. 2012; Puchwein et al. 2012) which can heat the gas in the halo and prevent it from cooling.

## 1.9.2 LOCAL PHOTOIONIZATION FEEDBACK SHAPES THE ROTATION CURVES

The rotation curves of the galaxies can be shaped by ongoing feedback processes. For example, Kannan et al. (2014) simulate a Milky Way-like galaxy using the local photoionization model that forms  $\sim 40$  per cent fewer stars than a simulation that only includes a standard uniform background UV field.

They found that the local photoionization model decreases star formation by increasing the cooling time of the gas in the halo and increasing the equilibrium temperature of dense gas in the disc. Further, the coupling of the local radiation field to gas cooling from the halo provides a preventive feedback mechanism which keeps the central disc light and produces slowly rising rotation curves without resorting to extreme feedback mechanisms. These results show that the effect of local photoionizing sources is significant in models of galaxy formation (see Fig. 1.10).

Radiative cooling is one of the most important processes of galaxy formation, because the cooling rate of the halo gas defines the star formation. It might slow down due to a number of factors including thermal pressure (Binney 1977; Rees & Ostriker 1977) and the incident radiation field (Rees 1986; Efstathiou 1992; Cantalupo 2010; Gnedin & Hollon 2012). Photoionization can

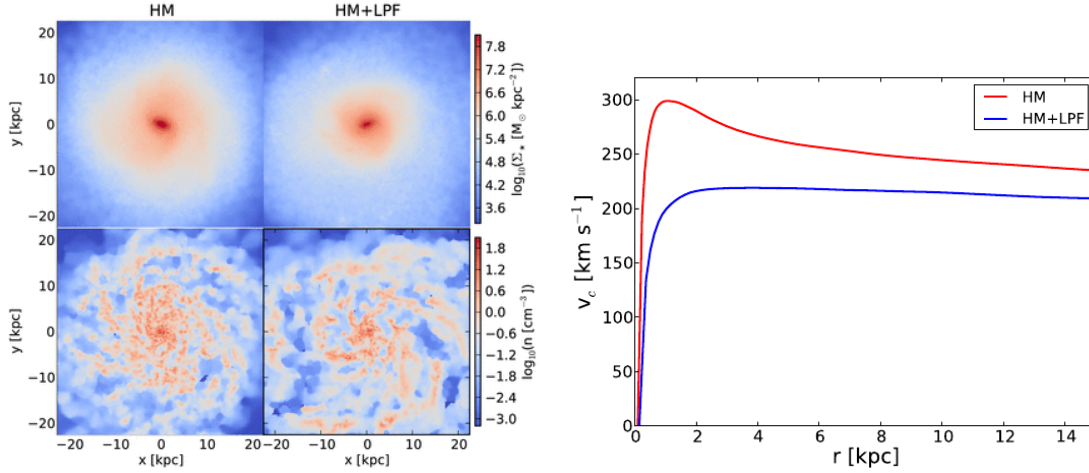


**Figure 1.10:** *Left:* The face-on projection view of the stellar (top panels) and gaseous (bottom panels) components of the MW-like galaxy simulations with a local photoionization feedback (right-hand panels) and without (left-hand panels). *Right:* The rotation curves of the galaxy adopting a local photoionization feedback (blue) and without (red) at  $z=0$ . The local photoionization feedback stop cooling of the gas and forming of stars giving a slow-rising shape of the rotation curve. (Credit: Kannan et al. 2014)

prevent the gas from cooling into low-mass halos (Rees 1986; Efstathiou 1992).

## 1.10 OUTLINE OF THE THESIS

This thesis focuses on dynamical modeling of 26 (E–Sd) galaxies across Hubble sequence using integral-field spectroscopic data. The SAURON and CALIFA two-dimensional stellar kinematic maps allow us to derive reliable mass distributions of galaxies, and hence to investigate the connection between their dark matter contents, ordered-over-random motions and the shape of the rotation curves.

In Chapter 2, we provide details about the data and the applied models. First, we present the sample selection and the spectroscopic instruments of the observations. Further, we describe the extraction of stellar kinematics and the photometry of the objects. Later, we present the multi-Gaussian Expansion (MGE) method to derive the surface brightness of the galaxies, and the two dynamical models. They are the asymmetric drift correction (ADC) and Jeans axisymmetric MGE (JAM) model approaches.

In Chapter 3, we compare ADC and JAM dynamical models in their application to galaxies with different morphologies. We investigate if all galaxies can be approximated with the thin disc assumption of the asymmetric drift correction or if a full line-of-sight integration is necessary as

it is provided by JAM approach to infer their gravitational potential.

In Chapter 4, we derive the stellar, gas and dynamical mass profiles of the galaxies. Our goal is to infer their dark matter contents and build up dynamical scaling relations in order to better understand the mass distribution of galaxies. We also classify our galaxies based on their kinematics and rotation curves' shapes.

In Chapter 5, we summarize our results and discuss prospects for a possible new galaxy formation scenario. Finally, we present the prospects for a related future work.

## ABSTRACT

We present SAURON (Spectroscopic Areal Unit for Research on optical Nebulae) and CALIFA (Calar Alto Legacy Integral Field spectroscopy Area) two-dimensional integral-field spectroscopic data of 18 Sb–Sd and 8 E–Sb galaxies, respectively. We describe the main techniques and model approaches applied to their photometry and stellar kinematics in order to obtain inner dynamical mass profiles and dark matter fractions. The Multi-Gaussian Expansion model represents the galaxies’ light distribution via fitting two-dimensional gaussians to the surface brightness. The estimation of the baryonic mass distribution is given by the stellar population analysis related to the stellar mass and a universal neutral gas profile to the gas mass. The commonly applied dynamical model approach for inferring the mass distribution of spiral galaxies is the asymmetric drift correction with axisymmetric thin disk approximation, while a full line-of-sight integration, as provided by solutions of the axisymmetric Jeans equations, is needed for ellipticals due to their triaxial shape.

## 2.1 INTRODUCTION

As we observed in Chapter 1, many galaxy components are not spherical or even axisymmetric, but triaxial: spiral galaxies embed large bulges that are often, including the one in the Galaxy, triaxial (Stark 1977, Gerhard et al. 1989, Häfner et al. 2000); and bars naturally strongly triaxial (Kent 1990, Merrifield & Kuijken 1995, Bureau & Freeman 1999). Giant ellipticals are known to be slowly-rotating triaxial structures (Binney 1976, Binney 1978, Davies & Illingworth 1983b, Bender & Nieto 1990, de Zeeuw & Franx 1991). Simulations routinely produce triaxial dark

halos (Barnes 1994, Weil & Hernquist 1996).

Determining the distribution of intrinsic triaxial shapes, the connection between internal velocity distributions and structure shapes, and the relation between the kinematics of stars (and gas) and dark matter content, might shed new light on to the processes of galaxy formation and evolution (Franx et al. 1991, Bak & Statler 2000).

However, solutions to these problems require kinematical, morphological and stellar population studies of galaxies along the Hubble sequence, together with advanced imaging techniques and dynamical modeling, adequate to structures with non-trivial shapes.

Indeed, kinematically, triaxial galaxy components can show complex structures, that are difficult to map with traditional long-slit spectroscopy (Arnold et al. 1994, Statler 1991, Statler 1994, de Zeeuw 1996). Long-slit spectroscopy has in fact insufficient spatial coverage to resolve the kinematics and line-strength distributions of the full disk of galaxies, since it is limited to a single position angle.

This makes two-dimensional integral-field spectroscopy (hereafter: IFS) of stars and gas highly desirable for deriving the dynamical structure of these systems and for determining their formation and evolution as there is no need to select any particular axis. An IFS produces spectra over a two-dimensional field (e.g., Bacon et al. 1995a, Weitzel et al. 1996, Allington-Smith et al. 1997).

As shown in Fig. 2.1, the major techniques for constructing IFS are: Lenslet arrays, Lenslet-Fiber reformatters, and Image slicers. A lenslet array (Fig. 2.1, top row) is positioned at the telescope focus, and guides the light from each spatial element onto a spectrograph. In the Lenslet-Fiber reformatters configuration a Fiber bundle is put at the telescope focus, which then leads the light from each spatial element into a spectrograph. The fiber bundle is put behind a lenslet array to increase the amount of light going into the spectrograph without losing resolution (Fig. 2.1, middle row). Finally, the concept of an image slicer (Fig. 2.1, bottom row) is similar to that of normal long-slit spectroscopy, but using several slits at the same time.

The final product of these systems is a three-dimensional datacube with spatially resolved spectra for a grid of points across the FoV (Bacon et al. 1988). Kinematic information is then extracted for each lens result in two-dimensional velocity maps covering the entire field of view of the galaxy. Recent studies have demonstrated that IFUs are superior to long-slit spectroscopy for studies of galactic dynamics. de Zeeuw et al. (2002) showed that early-type galaxies display a variety of kinematic structures which appear richer than expected. Decoupled cores, central stellar disks, minor-axis rotation, and non-axisymmetric and counter rotating gaseous disks were observed. It was also observed that the line-strength distributions appear to follow the surface brightness distribution closely. Moreover, Verolme et al. (2002) compared models constrained

by data along 4 slits extracted from the full data set and IFU data-derived mass models of M32. The authors found that mass model parameters like mass-to-light ratio, black hole mass, and, in particular, inclination were better constrained with the full two-dimensional data than with slits.

To obtain precisely dynamical information on the different galaxy types, in this thesis, we use two sets of integral-field unit data. The first one consist of 18 late-type (Sb-Sd) spiral galaxies, probing their inner parts with SAURON (Spectroscopic Areal Unit for Research on optical Nebulae; Bacon et al. 2001a). Then, we complete our study to all morphological types of galaxies using 8 (E–Sb) CALIFA (Calar Alto Legacy Integral Field spectroscopy Area; Sánchez et al. 2012a) survey. These integral field spectrographs are optimized to work in survey-mode and for studies of the kinematics of gas and stars in galaxies, with high throughput and, most importantly, with a large field of view.

The SAURON survey has been extended with ATLAS<sup>3D</sup> (260 early-type galaxies at  $z < 0.01$ ; Cappellari et al. 2011b), CALIFA has released for public use the 200 datacubes corresponding to the first 100 objects observed. Other on-going surveys are: PINGS project (Rosales-Ortega et al. 2010) at the CAHA 3.5m of  $\sim 12$  very nearby galaxies (10 Mpc) and the currently ongoing study of 70 (U)LIRGS at  $z < 0.26$  using different IFUs (Arribas et al. 2008). Finally, the VIRUS-P instrument is currently used to carry out two small IFS surveys, namely VENGA (30 spiral galaxies, Blanc et al. 2010a) and VIXENS2 (15 starbursts). In the future, MANGA will enable the spectral measurements across the face of each of  $\sim 10.000$  nearby galaxies.

In the case of the elliptical galaxies, due to their oblate/triaxial shape, advanced modeling is necessary, i.e, line-of-sight integration via axisymmetric Jeans equations or orbit-based modeling. However, in recent studies, it is not clear whether or not one can use the simpler asymmetric drift correction approach for inner mass modelings of spiral galaxies, requiring an assumption for thin axisymmetric disks. The late-type galaxies usually have small bulges and thin disk approximations have to be reasonable assumptions.

## 2.2 DATA AND SAMPLE SELECTION

The SAURON sample consists of 18 Sb–Sd nearby late-type spiral galaxies with Hubble types ranging from Sb to Sd. The sample selection, observations, and data reduction are presented in detail in Ganda et al. (2006, 2009). The galaxies were chosen from imaging projects with the Hubble Space Telescope, thus WFPC2 and/or NICMOS data were available (Carollo et al. 1997, 1998, 2002; Laine et al. 2002; Böker et al. 2002). All targets had to be brighter than  $B_T = 12.5$  according to the values listed in the de Vaucouleurs (1991) catalogue, where interacting and Seyfert galaxies were discarded. Additionally, visibility constraints have been applied.

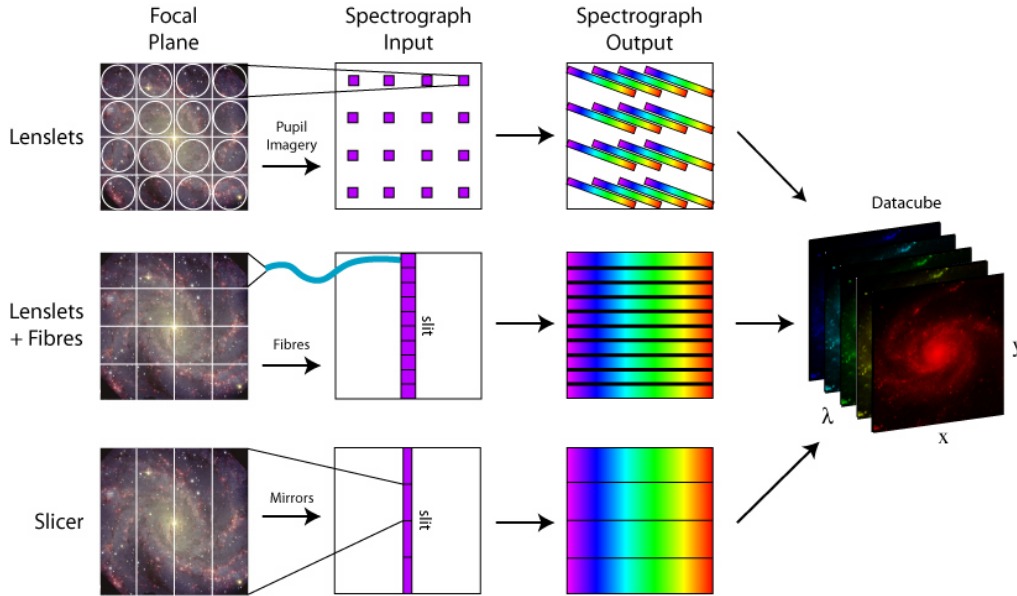


**Figure 2.1:** The main techniques for achieving integral field spectroscopy (credit: <http://ifs.wikidot.com/what-is-ifs>).

To complete the SAURON sample across Hubble sequence, we choose 8 E–Sb galaxies from the observed CALIFA targets (Sánchez 2006; Husemann et al. 2013) based on the following criterias: different morphological types (from elliptical to Sb spirals), inclination that allows us to avoid dust obscuration at maximum ( $25^\circ < i < 80^\circ$ ), and available kinematic data with sufficient signal-to-noise ratio ( $20 < S/N < 60$ ).

### 2.2.1 SAURON AND CALIFA INTEGRAL-FIELD SPECTROSCOPY

The dynamical modeling could be simple if the galaxy components had spherical shapes. However, many of them are axisymmetric or even triaxial (Binney 1976, Binney 1978, Davies & Illingworth 1983b, Bender & Nieto 1990, de Zeeuw & Franx 1991). It is difficult to map them with the traditional long-slit spectroscopy (e.g., STIS on the Hubble Space Telescope, Woodgate et al. 1998; Davies & Birkinshaw 1988; Statler & Smecker-Hane 1999). The two-dimensional integral-field spectroscopy of stars and gas is essential for deriving the dynamical structure of these systems and understanding their formation and evolution. Integral-field unit (IFU) indicates an instrument, providing spectra at each position on the sky and maintaining the information on the spatial location from which each light beam originated (Bacon et al. 2001b; Sánchez et al. 2012b). The output is a three-dimensional datacube with spatial and spectral information, giving information about the stellar kinematics and populations of the galaxies.

SAURON characteristic	HR mode
spatial sampling	0''.94
field of view	33'' × 41''
spectral resolution (FWHM)	4.2 Å
instrumental dispersion	108 km s <sup>-1</sup>
spectral sampling	1.1 Å pixel <sup>-1</sup>
spectral range	4800-5400 Å
emission features	H $\beta$ , [OIII],[NI]
absorption features	H $\beta$ , Fe5015, Mgb

**Table 2.1:** Specifications of SAURON spectrograph in its low-resolution mode.

CALIFA characteristic		
sample		SDSS DR7, $\delta > 7^\circ$
redshift		$0.005 < z < 0.03$
diameter		$45'' < D_{25} < 80''$
field of view		74'' × 64'' hexagon
spatial resolution		~ 2'' (FWHM)

Grating	V500	V1200
3 $\sigma$ depth	~ 23.0 mag/arcsec <sup>2</sup>	~ 22.8 mag/arcsec <sup>2</sup>
wavelength	3745-7300 Å	3400-4750 Å
spectral resolution	~ 6.5 Å (FWHM)	~ 2.7 Å (FWHM)

**Table 2.2:** Specifications of CALIFA spectrograph in V500 and V1200 mode.

The 18 spiral galaxies were observed with the integral-field unit spectrograph SAURON at the 4.2-m William Herschel Telescope of the Observatorio del Roque de los Muchachos on La Palma, Spain. It presents a larger field of view with respect to its predecessors: integral-field spectrograph TIGER and OASIS at the Canada-France-Hawaii telescope to study galactic nuclei (Bacon et al. 1995b, 2000). It consists of a filter, which selects a fixed wavelength range and an enlarger that images the sky on a lenslet array (Bacon et al. 2001b). Each lenslet produces a micropupil. Its light, first passes through a collimator and then dispersed by a grism. Finally, the resulting spectra are imaged on a CCD camera. The instrument measures the mean streaming velocity  $V$ , the velocity dispersion  $\sigma$  and the velocity profile (or line-of-sight velocity distribution, LOSVD) of the stellar absorption lines and the emission lines of the ionized gas, the two-dimensional distribution of line-strengths and line-ratios. In this thesis, we focus on the measured  $V$  and  $\sigma$  of the stellar absorption lines for dynamical modeling.

The SAURON IFU (Bacon et al. 2001b) has a  $33'' \times 41''$  field-of-view (FoV), sampled by an array of  $0.94'' \times 0.94''$  square lenses. It corresponds to a radial extent of 1/5 to 1/3 of the galaxy's half-light radius ( $R_e$ ). The spectral resolution is  $4.2 \text{ \AA}$  (FWHM), corresponding to an instrumental dispersion of  $105 \text{ km s}^{-1}$  in the selected spectral range 4800–5380  $\text{\AA}$  ( $1.1 \text{ \AA}$  per pixel). This range includes a number of absorption features at the redshift of the selected galaxies – Fe, Mgb and  $H\beta$ , which we use to measure the stellar kinematics. Emission lines like [OIII], [NI] and  $H\beta$  can be used to probe the ionised gas properties (see Table 2.1).

The observations were reduced by Ganda et al. (2006) using the dedicated software XSAURON (Bacon et al. 2001b). To obtain a sufficient signal-to-noise ratio (S/N), we spatially binned the data cubes using the Voronoi 2D binning algorithm of Cappellari & Copin (2003). The Voronoi Binning method optimally solves the problem of preserving the maximum spatial resolution of general two-dimensional data, given a constraint on the minimum signal-to-noise ratio. We created compact bins with a minimum S/N  $\sim 60$  per spectral resolution element. In the central regions many individual spectra have S/N  $> 60$  and thus remained un-binned.

Together with the SAURON data, we use the most recent integral-field spectroscopic survey CALIFA (Sánchez 2006; Husemann et al. 2013) with the 3.5-m telescope at Calar Alto Observatory to extend our study on the mass distribution of galaxies from the stellar kinematics. The final sample of the survey includes around 600 nearby galaxies. CALIFA is the largest and the most comprehensive wide integral-field unit (IFU) survey of galaxies carried out to date. CALIFA will increase our knowledge of the baryonic physics of galaxy evolution: star formation, AGN, shocks; measurement of ionized oxygen and nitrogen abundances in the galaxies; measurement of stellar population properties; measurement of galaxy kinematics in gas and stars.

The observations of the 8 (E–Sb) galaxies have been made by using the integral-field spectroscopic instrument PMAS/PPAK on the Calar Alto 3.5-m telescope. Each galaxy has been targeted with a mid-resolution (V1200) prism covering the nominal wavelength range 3850–4600  $\text{\AA}$  at a Full Width at Half Maximum (FWHM) spectral resolution of  $\sim 2.3 \text{ \AA}$ , i.e.,  $\sigma \sim 85 \text{ km s}^{-1}$  and a  $74'' \times 64''$  hexagonal field-of-view (FoV). The exposure time per pointing has been fixed to 1800 s, split into 2 or 3 individual exposures (Sánchez 2006; Husemann et al. 2013; see Table 2.2).

The PMAS/PPAK integral-field unit provides a three-dimensional datacube with spatially resolved spectra for a grid of points across the FoV (Husemann et al. 2013). Here, we spatially binned our datacube using the Voronoi 2D binning algorithm of Cappellari & Copin (2003) to obtain signal-to-noise ratio of  $\sim 20$  and, hence, better stellar kinematics.

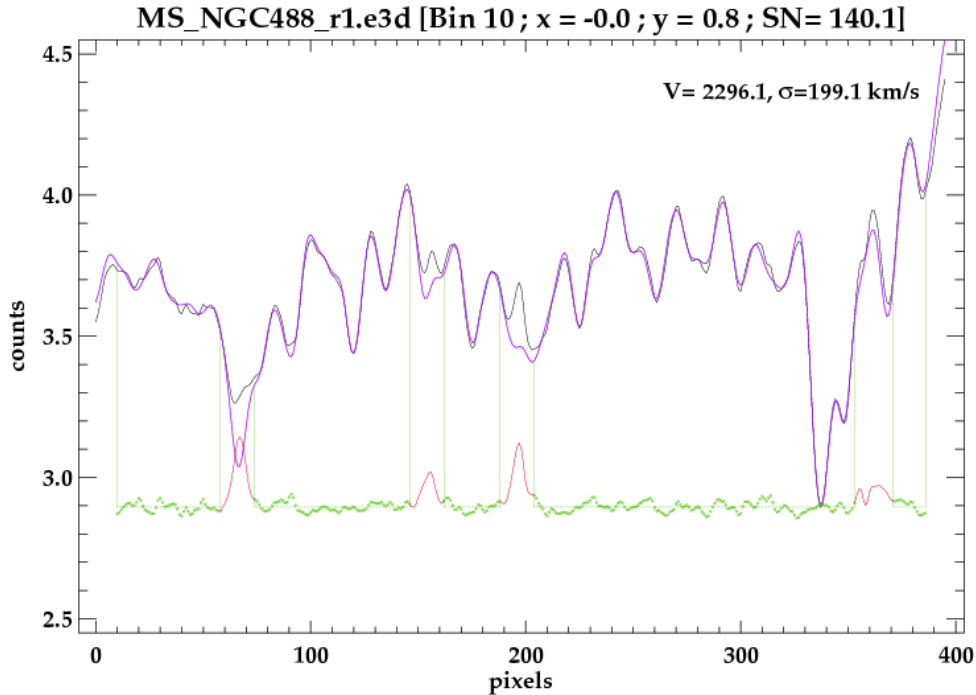


**Figure 2.2:** pPXF fit (magenta) to SAURON spectra (black) of NGC 488 galaxy in the wavelength region 480-538nm. The fit residuals are plotted in green and the non-fitted gas emission lines in red.

## 2.3 STELLAR KINEMATICS EXTRACTION

Stellar kinematics is a study about the movement of the stars within the galaxy. It does not require information about how the stars acquired their motions, e.g. taking in account gravitational effects, to construct a reliable mass distribution of the galaxies. The first step in the exploring the inner kinematics of galaxies is made by [Slipher \(1914\)](#) detecting inclined lines of M31. Later, [Rubin \(2000\)](#) discover the observational evidence about the gas and star rotation around the center of the galaxies. The recent studies about the stellar kinematics are made via spectroscopic observations ([Bacon et al. 2001b](#); [Cappellari et al. 2011a](#); [Sánchez et al. 2012b](#)).

Each (unresolved) star contributes to the galaxy's spectrum and its absorption lines appear shifted with respect to its line-of-sight velocity, according to the Doppler effect. However, the stars have generally different velocities and direction of motions in the galaxy. Therefore, the absorption lines in the observed spectrum will appear broadened as result of the integration over many stars ([Binney & Tremaine 1987](#)).

The distribution of the stellar velocities along the line-of-sight can be expressed by a broadening function, called 'line-of-sight-velocity distribution' (LOSVD; [Rix & White 1992](#); [Kuijken &](#)

Merrifield 1993; van der Marel 1994; Saha & Williams 1994; Merritt 1997; Gebhardt et al. 2000; Kelson et al. 2000). LOSVD are generally close to Gaussians, so a small number of Gauss-Hermite terms will provide a reliable and compact description of the motion of the galaxies. The Gauss-Hermite series are orthogonal functions that describe the LOSVD. The most relevant terms of the expansion are the mean velocity  $V$ , the velocity dispersion  $\sigma$  and the Gauss-Hermite coefficients  $h_3$  and  $h_4$ , that measured respectively the asymmetric and symmetric deviations of the LOSVD from a Gaussian (Gerhard 1993; van der Marel & Franx 1993).

In the described way, we extract the stellar kinematics of the 26 E–Sd SAURON and CALIFA galaxies using the penalized pixel-fitting (pPXF) method of Cappellari & Emsellem (2004), see Fig. 2.2. We then fitted a non-negative linear combination of single stellar population (SSP) models, convolved with a Gauss–Hermite series (van der Marel & Franx 1993), to each galaxy spectrum by  $\chi$ -square minimization. The spectral regions that are affected by nebular emission (corresponding to the  $H\beta$ , O III, N I lines) are masked out during the fitting procedure.

A low-order polynomial (generally of order six) is also included in the fit to account for small differences in the flux calibration between the galaxy and the template spectra. Thus we obtained the velocity,  $V$ , and velocity dispersion,  $\sigma$ , for each bin (see Fig. 2.3). The errors on the stellar kinematics are obtained by Monte-Carlo simulations for each bin of our data (e.g., Falc3n-Barroso et al. 2006).

## 2.4 NEAR-INFRARED IMAGING

To parametrise the light distribution of the SAURON galaxies, we use the surface brightness profiles obtained by Ganda et al. (2009). They used archive grand-based H-band images from Two-Micron All Sky survey (hereafter, 2MASS) complemented with near-infrared Hubble Space Telescope (HST) NICMOS/F160W images for 11 cases and optical HST WFPC2/F814W for the remaining 7 galaxies (NGC 1042, NGC 2805, NGC 3346, NGC 3423, NGC 4487, NGC 4775, NGC 5668). To obtain an accurate determination of the sky level and the galaxy disc geometry, DSS (Digitised Sky Survey) images were used for the outer parts of the same galaxies.

Ganda et al. (2009) derived the global parameters using the *ellipse* task in IRAF package with the centre, position angle and ellipticity as free parameters. Photometric profiles were extracted from the combined images, keeping the latter parameters fixed. In the end, there were three photometric profiles and their combination gave a single near-infrared H-band profile with the maximum extension and inner spatial resolution allowed by the data. The error introduced by this combination of optical and infrared images was negligible (Ganda et al. 2009, Sec.3.3) and, thus, do not effect our analysis.

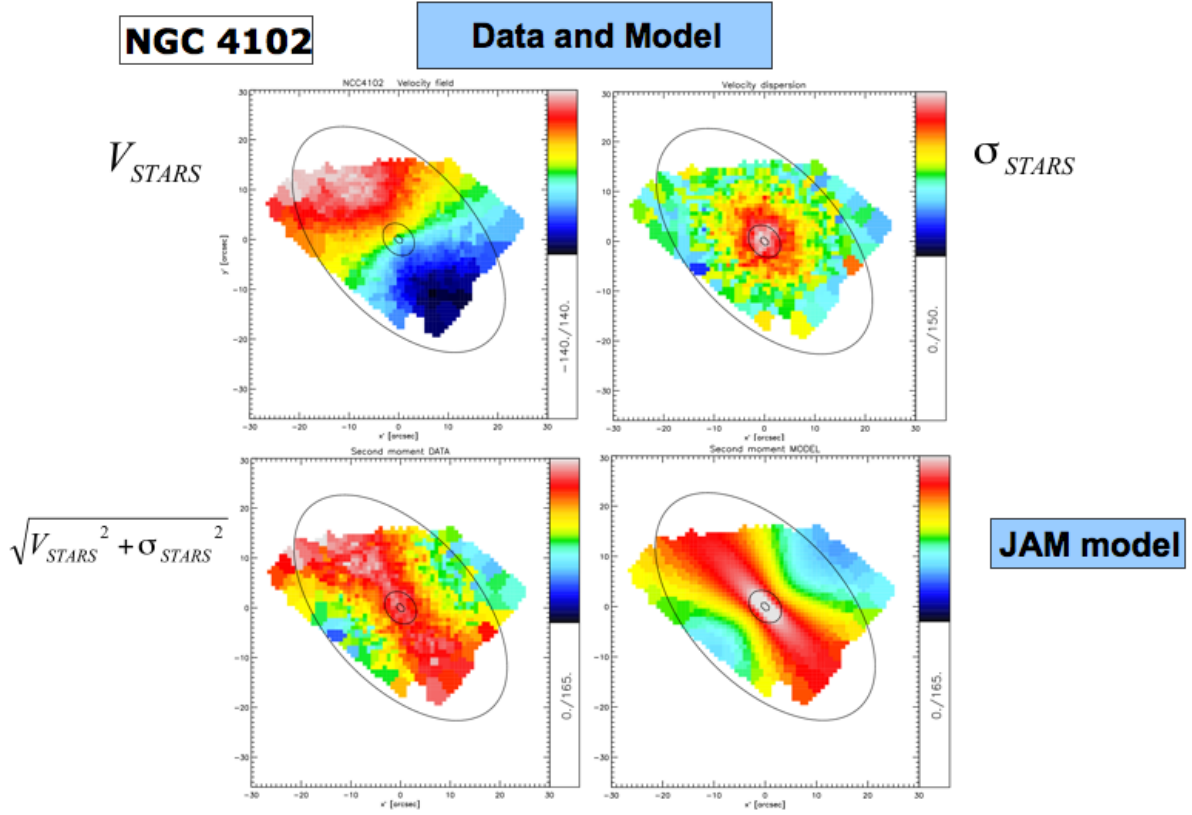


**Figure 2.3:** Oblate axisymmetric dynamical model of NGC 4030. Maps of the mean velocity  $V$  (top left) and velocity dispersion  $\sigma$  (top-right) are combined into the second velocity moment of the data  $V_{\text{rms}} = \sqrt{V_{\text{stars}}^2 + \sigma_{\text{stars}}^2}$  (bottom left), which is then fitted by a solution of the Jeans equations based on the de-projected stellar light distribution multiplied with a constant mass-to-light ratio  $\Upsilon_{\text{dyn}}$ . The resulting second velocity moment of the model  $V_{\text{rms}} = \sqrt{V_{\text{mod}}^2 + \sigma_{\text{mod}}^2}$  (bottom right) represents well the observations.

For CALIFA galaxies, we use the available online source for photometric images of Sloan Digital Sky Survey (SDSS)<sup>1</sup> to obtain the surface brightness of the galaxies. The SDSS data comes from the Data Release 8 (DR8)<sup>2</sup> of the survey,  $r$ -band photometry with applied flux calibration and sky subtraction.

We used *ellipse* task in the IRAF package to smooth the light distribution of the CALIFA galaxies before modeling their surface brightness distribution with the multi-Gaussian expansion method (MGE; Monnet et al. 1992; Emsellem et al. 1994). This was necessary especially in the case

<sup>1</sup><http://www.sdss.org/>

<sup>2</sup><http://www.sdss3.org/dr8/>

of spiral galaxies with complex structure and features like bars, rings and material arms. We constructed the smooth light models by fitting ellipses to the surface brightness of the galaxy with fixed center, position angle and ellipticity.

## 2.5 PHOTOMETRIC AND MASS MODELLING METHODS

The stellar mean velocity and velocity dispersion maps for most of the 26 E–Sd galaxies are consistent with axisymmetry. The effect of bars in half of the galaxies seems to be rather weak. This justifies the assumption of a stationary axisymmetric stellar system for the inner parts of our galaxies.

### 2.5.1 AXISYMMETRIC JEANS EQUATIONS

In the case of steady state axisymmetry, both the potential  $\Phi(R, z)$  and distribution function (DF) are independent of azimuth  $\phi$  and time. By Jeans' theorem (Jeans 1915) the DF depends only on the isolating integrals of motion:  $f(E, L_z, I_3)$ , with energy  $E = (v_R^2 + v_\phi^2 + v_z^2)/2 + \Phi(R, z)$ , angular momentum  $L_z = Rv_\phi$  parallel to the symmetry  $z$ -axis, and a third integral  $I_3$  for which in general no explicit expression is known. However, usually<sup>3</sup>  $I_3$  is invariant under the change  $(v_R, v_z) \rightarrow (-v_R, -v_z)$ . This implies that the mean velocity is in the azimuthal direction ( $\overline{v_R} = \overline{v_z} = 0$ ) and the velocity ellipsoid is aligned with the rotation direction ( $\overline{v_R v_\phi} = \overline{v_\phi v_z} = 0$ ). Schwarzschild (1979) introduced a method that sidesteps our ignorance about the non-classical integrals of motion. It finds the set of weights of orbits computed in an arbitrary gravitational potential that best reproduces all available photometric and kinematic data at the same time. The method has proved to be powerful in building detailed spherical, axisymmetric (e.g. Rix et al. 1997; van der Marel & van den Bosch 1998; Gebhardt et al. 2003; Valluri et al. 2004; Cappellari et al. 2006; Thomas et al. 2007) as well as triaxial models of nearby galaxies (van de Ven et al. 2006; van den Bosch et al. 2006) and globular clusters (e.g. van de Ven et al. 2006; van den Bosch et al. 2006). However, as higher-order stellar kinematic measurements are necessary to constrain the large freedom in this general modelling method, we instead construct simpler, but still realistic dynamical models based on the solution of the axisymmetric Jeans equations (Cappellari 2008; van de Ven et al. 2010).

When we multiply the collisionless Boltzmann equation in cylindrical coordinates by respec-

<sup>3</sup>If resonances are present,  $I_3$  may lose this symmetry.

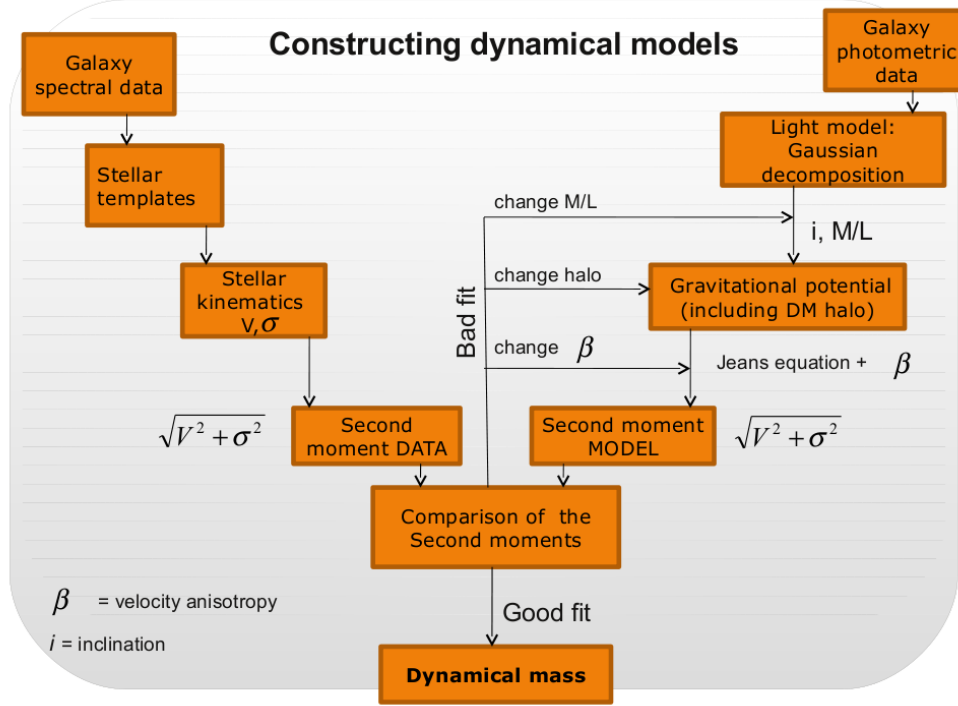


**Figure 2.4:** Scheme of the Jeans axisymmetric dynamical model fitting procedure.

tively  $v_R$  and  $v_z$  and integrate over all velocities, we obtain the two Jeans equations, (Jeans 1915)

$$\frac{\partial(Rv\overline{v_R^2})}{\partial R} + R\frac{\partial(v\overline{v_R v_z})}{\partial z} - \overline{v\overline{v_\phi^2}} + Rv\frac{\partial\Phi}{\partial R} = 0, \quad (2.1)$$

$$\frac{\partial(Rv\overline{v_R v_z})}{\partial R} + R\frac{\partial(v\overline{v_z^2})}{\partial z} + Rv\frac{\partial\Phi}{\partial z} = 0, \quad (2.2)$$

where  $v(R, z)$  is the intrinsic luminosity density. Due to the assumed axisymmetry, all terms in the third Jeans equation, that follows from multiplying by  $v_\phi$ , vanish.

We thus have two Jeans equations (2.1) and (2.2), but four unknown second order velocity moments  $\overline{v_R^2}$ ,  $\overline{v_z^2}$ ,  $\overline{v_\phi^2}$  and  $\overline{v_R v_z}$ . This means we have to make assumptions about the velocity anisotropy, or in other words the shape and alignment of the velocity ellipsoid. In case the velocity ellipsoid is aligned with the cylindrical  $(R, \phi, z)$  coordinate system  $\overline{v_R v_z} = 0$ , so that we can readily solve equation (2.2) for  $\overline{v_z^2}$ . If we next assume a constant flattening of the velocity ellipsoid in the meridional plane, we can write  $\overline{v_R^2} = \overline{v_z^2}/(1 - \beta_z)$  and solve equation (2.1) for  $\overline{v_\phi^2}$ . This assumption provides in general a good description for the kinematics of real disc galaxies (Cappellari 2008). When  $\beta_z = 0$ , the velocity distribution is isotropic in the meridional plane, corresponding to the

well-known case of a two-integral DF  $f(E, L_z)$  (e.g. Lynden-Bell 1962; Hunter 1977).

Knowing the intrinsic second-order velocity moments, the line-of-sight second-order velocity moment for a stellar system viewed at an inclination  $i > 0$  away from the  $z$ -axis follows as

$$\overline{v_{\text{los}}^2} = \frac{1}{I(x', y')} \int_{-\infty}^{+\infty} \nu \left[ \left( \overline{v_R^2} \sin^2 \phi + \overline{v_\phi^2} \cos^2 \phi \right) \sin^2 i + \overline{v_z^2} \cos^2 i - \overline{v_R v_z} \sin \phi \sin(2i) \right] dz',$$

where  $I(x', y')$  is the (observed) surface brightness with the  $x'$ -axis along the projected major axis. For each position  $(x', y')$  on the sky-plane,  $\overline{v_{\text{los}}^2}$  yields a prediction of the (luminosity weighted) combination  $V_{\text{rms}}^2 = V^2 + \sigma^2$  of the (observed) mean line-of-sight velocity  $V$  and dispersion  $\sigma$ .

Under the above assumptions, besides the anisotropy parameter  $\beta_z$  (and possibly the inclination  $i$ ), the only unknown quantity is the gravitational potential  $\Phi(R, z)$ , which via Poisson's equation is related to the total mass density  $\rho_{\text{tot}}(R, z)$ . We may estimate the latter from the intrinsic luminosity density  $\nu(R, z)$ , derived from deprojecting the observed surface brightness  $I(x', y')$ , once we know the total mass-to-light ratio  $\Upsilon_{\text{tot}}$ . It is common in dynamical studies of the inner parts of galaxies to consider  $\Upsilon_{\text{tot}}$  as an additional parameter and to assume its value to be constant, i.e., mass follows light (e.g. Cappellari et al. 2006). Since  $\Upsilon_{\text{tot}}$  may be larger than the stellar mass-to-light ratio  $\Upsilon_*$ , this still allows for possible dark matter contribution, but with a constant fraction (see Fig. 2.4).

## 2.5.2 MULTI-GAUSSIAN EXPANSION

We use the Multi-Gaussian Expansion method (MGE; Monnet et al. 1992; Emsellem et al. 1994) to parameterise the observed surface brightness  $I(x', y')$  by a sum of  $N$  Gaussian components

$$I(x', y') = \sum_{j=0}^N I_{0,j} \exp \left\{ -\frac{1}{2\sigma_j'^2} \left[ x'^2 + \frac{y'^2}{q_j'^2} \right] \right\}, \quad (2.3)$$

each with three parameters: the central surface brightness  $I_{0,j}$ , the dispersion  $\sigma_j'$  along the major  $x'$ -axis and the flattening  $q_j'$ . Even though Gaussians do not form a complete set of functions, the surface density distributions are accurately reproduced generally. Representing also the point-spread function (PSF) by a sum of Gaussians, the convolution with the PSF becomes straightforward (see Fig. 2.5). Moreover, the MGE-parameterisation has the advantage that the deprojection can be performed analytically once the viewing angle is given. Also, many intrinsic quantities, including the gravitational potential, can be calculated by means of simple one-dimensional integrals (Emsellem et al. 1994eq. 39). Similarly, the calculation of  $\overline{v_{\text{los}}^2}$  in equation (2.3) reduces from the (numerical) evaluation of a triple integral to a straightforward single integral (Cappellari

2008eq. 27). The circular velocity in the equatorial plane follows upon (numerical) evaluation of the single integral

$$v_{c,\text{JAM}}^2(R) = \int_0^1 \sum_k \frac{2GM_k R^2}{\sqrt{2\pi}\sigma_k \sigma_k^2} \exp\left(-\frac{u^2 R^2}{2\sigma_k^2}\right) \times \frac{u^2}{\sqrt{1 - (1 - q_k^2)u^2}} du, \quad (2.4)$$

where  $M_k = \Upsilon_k L_k$  is the total mass per Gaussian component with luminosity  $L_k = 2\pi\sigma_k^2 q_k' I_{0,k}$  and corresponding mass-to-light ratio  $\Upsilon_k$ . In case of oblate axisymmetry, the intrinsic dispersion and flattening of the Gaussian components in equation (2.3) fitted to the observed surface brightness, follow from the observed dispersion and flattening as  $\sigma_k = \sigma_k'$  and  $q_k^2 \sin^2 i = q_k'^2 - \cos^2 i$ , for a given inclination  $i$  (ranging from  $i = 0^\circ$  face-on to  $i = 90^\circ$  edge-on).

Here, we assume that mass follows light in the inner part of the spiral galaxies, so that  $\Upsilon_k = \Upsilon_{\text{tot}}$  is the same for all Gaussian components. Whereas this still allows for the presence of a constant dark matter fraction, a dark matter halo can also be explicitly included by expressing its mass density distribution by a set of  $N_{\text{dm}}$  additional Gaussian components. Setting  $\Upsilon_k = \Upsilon_\star$  for the  $N$  'luminous' Gaussian components, the  $N_{\text{dm}}$  'dark' Gaussian components are then added to yield the total mass density  $\rho_{\text{tot}}$ , corresponding gravitational potential  $\Phi$  and circular velocity  $v_{c,\text{JAM}}$  by summing over all  $N + N_{\text{dm}}$  Gaussian components in equation (2.4). We adopt a NFW spherical halo (Navarro et al. 1997a) to our sample of galaxies with the core and scale radius as free parameters. However, we do not find a significant improvement from the mass follows light fits (not unexpected because our kinematics only extends in radius of 1/5 to 1/3 from the half-light radius).

### 2.5.3 ASYMMETRIC DRIFT CORRECTION

Instead of solving both Jeans equations (2.1) and (2.2), we can also evaluate the first equation in the equatorial plane ( $z = 0$ ) and use  $v_c^2 = R(\partial\Phi/\partial R)$  and  $\partial v/\partial z = 0$  by symmetry to rewrite it as

$$v_{c,\text{ADC}}^2(R) = \overline{v_\phi}^2 + \sigma_R^2 \left[ \frac{\partial \ln(v\sigma_R^2)^{-1}}{\partial \ln R} + \left( \frac{\sigma_\phi^2}{\sigma_R^2} - 1 \right) - \frac{R}{\sigma_R^2} \frac{\partial \overline{v_R v_z}}{\partial z} \right]. \quad (2.5)$$

Here,  $\overline{v_\phi}$  is the intrinsic mean velocity (or streaming motion), and  $\sigma_\phi^2 = \overline{v_\phi^2} - \overline{v_\phi}^2$ ,  $\sigma_R^2 = \overline{v_R^2}$  are (the square of) the intrinsic mean velocity dispersions.

In case of a dynamically cold tracer such as atomic or neutral gas, observed through HI and CO emission at radio wavelengths, the mean velocity is typically much larger than the velocity dispersion ( $V \gg \sigma$ ), so that the circular velocity is directly proportional to the (deprojected)

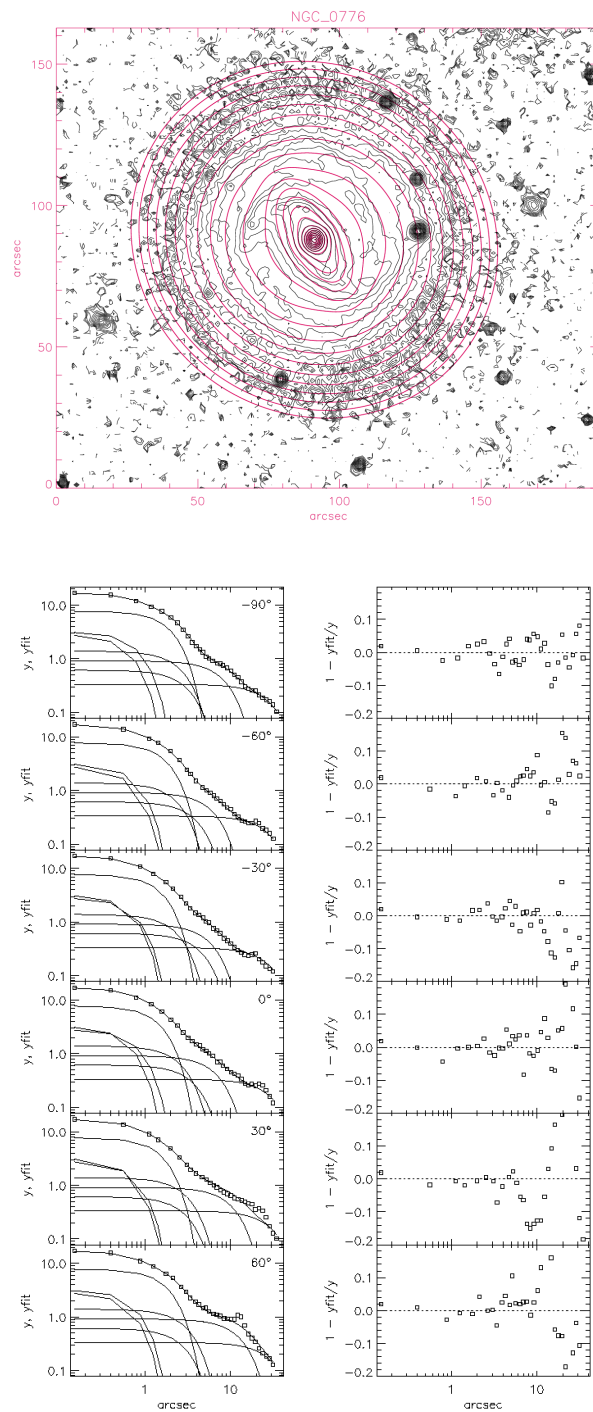


**Figure 2.5:** Multi-Gaussian Expansion (MGE) method applied to the surface brightness of galaxy NGC 0776. *Top:* MGE contours overlapped on the galaxy image. *Bottom:* MGE best fit profiles (left) and their residuals (right).

observed rotation,  $v_c \simeq \overline{v_\phi}$ . However, if the velocity dispersion is not anymore negligible, the observed rotation only captures part of the circular velocity and the velocity dispersion needs to be taken into account. The latter so-called asymmetric drift correction (ADC) can even become dominant in case of dynamically hot ( $V \ll \sigma$ ) tracers like stars.

As can be seen from equation (2.5), the correction depends on the two intrinsic velocity dispersions  $\sigma_R$  and  $\sigma_\phi$ , and the cross term  $\overline{v_R v_z}$ , which together define the so-called velocity ellipsoid. Following Appendix A of Weijmans et al. (2008), we can represent the velocity ellipsoid by the radial logarithmic gradient of the intrinsic mean velocity,  $\alpha_R$ , the flattening of the gravitational potential,  $q_\phi$ , and a parameter  $\kappa$  that controls its orientation in the meridional plane (with  $\kappa = 0$  and  $\kappa = 1$  corresponding to alignment with respectively the cylindrical and spherical coordinate system).

Under the assumption of a 'thin disc' with  $\partial \ln v / \partial \ln R \approx d \ln I / d \ln R$ , the expression of the circular velocity then reduces to

$$v_{c,\text{ADC}}^2(R) = \overline{v_\phi}^2 + \sigma_R^2 \left\{ \frac{\partial \ln (I \sigma_R^2)^{-1}}{\partial \ln R} - (1 - \alpha_R) \times \left[ \frac{1}{2} + \frac{\kappa}{\kappa q_\phi^2 (1 + \alpha_R) + (1 - \alpha_R)} \right] \right\}. \quad (2.6)$$

We adopt here  $q_\phi = 1.0$  and  $\kappa = 0.5$ , but show in Appendix A that the circular velocity depends only weakly on (reasonable values of) these parameters. Thus, with the deprojected surface brightness profile  $I$  (using MGE parametrisation),  $\overline{v_\phi}$  and  $\alpha_R$  from the (observed) mean line-of-sight velocity  $V$ , and  $\sigma_R$  from the (observed) line-of-sight velocity dispersion  $\sigma$  (see Sec. 3.4.2), the latter equation provides an estimate of  $v_{c,\text{ADC}}$ , which traces the underlying gravitational potential  $\Phi$  and thus yields the total mass density  $\rho_{\text{tot}}$ .

## 2.6 SUMMARY

In this Chapter, we present two sets of spectroscopic data, SAURON and CALIFA. They consist of 18 Sb–Sd late-type and 8 E–Sb galaxies, respectively. Their stellar kinematics can be extracted from the 3D data cubes of the observations via using penalized pixel-fitting (pPXF) method of Cappellari & Emsellem (2004) with a set of single age and metallicity stellar population models.

Later, we discuss the two modeling approaches to derive mass distributions of galaxies, and particularly their circular velocity curves.

The first approach is an oblate axisymmetric dynamical model, where the contribution of the stellar mass to the gravitational potential can be obtained by de-projecting and modeling the surface photometry of the galaxy. One can use the multi-Gaussian expansion method for this

purpose. Then the gravitational potential is derived by a simple integration based on the intrinsic density, stratified on similar triaxial ellipsoids and mass-follows-light assumptions. Further, the solutions of the Jeans equations in the axisymmetric case fitted the observed second velocity moment  $V_{\text{rms}} = \sqrt{V^2 + \sigma^2}$  (where  $V$  is the mean velocity and  $\sigma$  is the velocity dispersion of the galaxy) with several assumptions. As a result, the obtained from best-fit model mass distribution, through Poisson's equation, is related to the gravitational potential; the circular velocity follows as  $V_{\text{circ}}^2 = R \frac{\partial \Phi}{\partial R} |_{z=0}$ .

An alternative and simpler dynamical modeling is the asymmetric drift correction, assuming that most of the galaxies can be represented by a thin disk. To apply this model, one first need to extract  $V$  and  $\sigma$  profiles along the projected major axis from the corresponding kinematic maps. Then, the values for the inclination must be corrected to infer the azimuthal velocity  $\bar{v}_\phi$  and the radial velocity dispersion  $\sigma_R$ . Furthermore, the circular velocity is  $V_{\text{circ}}^2 = \bar{v}_\phi^2 + \sigma_R^2 \left[ \partial \ln (I \sigma_R^2)^{-1} / \partial \ln R + A \right]$ , where  $I$  is the surface brightness of the galaxy and  $A$  is a relative small contribution depending on the velocity anisotropy.

In the next Chapter 3, we will compare the two dynamical model approaches and will draw conclusions for their reliability across galaxy's morphology.

# AXISYMMETRIC JEANS EQUATIONS VERSUS ASYMMETRIC DRIFT CORRECTION

## ABSTRACT

We infer the total mass distribution of 26 E–Sd galaxies by fitting a solution of the axisymmetric Jeans equations to stellar kinematic maps of their inner parts obtained with the integral-field spectrographs SAURON and PMAS/PPAK. We compare the corresponding circular velocity curves with those estimated with the commonly applied asymmetric drift correction (ADC). We find agreement for only one galaxy, whereas the ADC yields masses that are typically up to 3–4 times lower. We conclude that when locally  $V/\sigma \lesssim 1.5$  the ADC approach can significantly underestimate the circular velocity curve and hence enclosed mass. A full line-of-sight integration as provided by solutions of the axisymmetric Jeans equations (or an orbit-based model) is therefore needed to reliably infer galaxy mass distributions.

## 3.1 INTRODUCTION

The non-Keplerian rotation curves of spiral galaxies provided the first observational evidence that galaxies are embedded in extensive dark matter haloes (Bosma 1978; Rubin & Ford 1983; van Albada et al. 1985; Begeman 1987). Historically, the 21-cm emission from atomic neutral hydrogen gas (HI) has been the main tool to derive galaxy rotation curves, because of its capability to trace the gravitational field beyond the optical stellar disc. However, the central rotation curve is often poorly constrained due to insufficient spatial resolution as well as the lack of HI gas in the elliptical galaxies (e.g., Longair 1998) and inner parts of disk galaxies (e.g., Noorder-

meer et al. 2007). The interstellar medium in the centre of disk galaxies is instead dominated by gas in the molecular and ionised phases (e.g., Leroy et al. 2008).

Unfortunately, gas settles in the galaxy disc plane (or polar plane) and is thus insensitive to the mass distribution perpendicular to it, and above all due to its dissipative nature easily disturbed by perturbations in the plane from for example a bar or spiral arm. Indeed, rotation curves derived through CO emission, the common tracer for the molecular gas distribution, often show non-axisymmetric signatures such as wiggles (Wada & Koda 2004). The hot ionised gas has the additional disadvantage that the observed rotation alone is often insufficient to trace the total mass distribution so that also its velocity dispersion needs to be taken into account, which however is also influenced by a typically unknown contribution from non-gravitational effects such as stellar winds and shocks (e.g., Weijmans et al. 2008). Stars, on the other hand, are present in all galaxy types, are distributed in all three dimensions, and as they are collisionless much less sensitive to perturbations.

However, to use stars as tracers of the underlying gravitational potential, we need to know both their ordered as well as random motions. Moreover, their random motion can be different in all three directions, which is also referred to as velocity anisotropy, so that more challenging observational as well as modelling techniques are required to uncover the total mass distribution. Nowadays, integral-field spectrographs like SAURON (Bacon et al. 2001b) and PMAS/PPAK (Sánchez et al. 2012b) used in this study, allow us to extract high-quality stellar kinematic maps. Similarly, dynamical modelling approaches like Schwarzschild's orbit-superposition method enable us to fit the stellar kinematics in detail and infer the velocity anisotropy and intrinsic total mass distribution (e.g., van den Bosch et al. 2008).

Even so, for the galaxies a common approach is to apply the so-called asymmetric drift correction (ADC; Binney & Tremaine 2008) to infer the circular velocity curve from the measured stellar mean velocity and velocity dispersion profiles. This approach is rather straightforward as the velocity and dispersion profiles can also be obtained from long-slit spectroscopy and no line-of-sight integration is required due to the underlying thin-disc assumption. Aside from the inclination needed to deproject, only the velocity anisotropy remains as free parameter but typically only has a small effect. As such, this ADC approach is still widely adopted in studies that use the stellar kinematics to infer the circular velocity curve. For example, when investigating the Tully-Fisher relation for earlier-type spirals (e.g., Bottema 1993, Neistein et al. 1999; Williams et al. 2010), the speed of bars (e.g., Aguerrri et al. 1998; Buta & Zhang 2009), as well as the inner dark matter distribution of galaxies (e.g., Kregel et al. 2005; Weijmans et al. 2008).

In this paper, we infer the total mass distribution of 26 E–Sd spiral galaxies by fitting a solution of the axisymmetric Jeans equations to stellar mean velocity and velocity dispersion fields of their inner parts obtained with the integral-field spectrographs SAURON and PMAS/PPAK. These Jeans

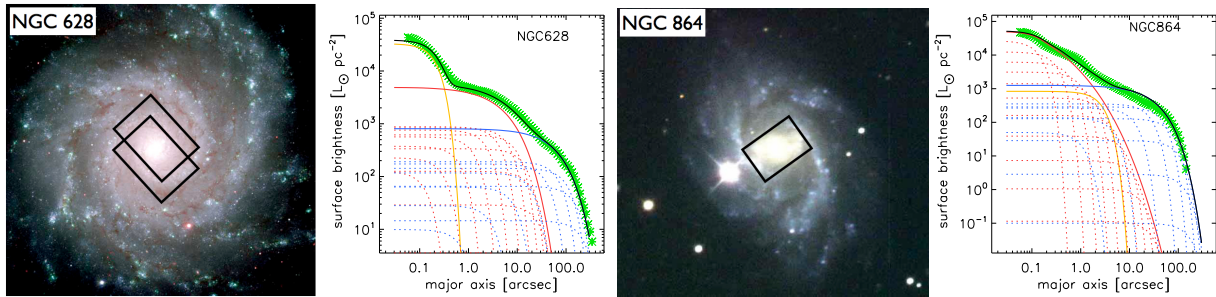


**Figure 3.1:** Multi-colour SDSS images, with the SAURON field-of-view overlaid (black rectangles), and multi-Gaussian expansion models of the galaxies NGC 628 (left panels) and NGC 864 (right panels). Green asterisks represent the observed luminosity profiles. The black thick curves show the sum of the individual gaussians (dotted curves) of the three components: nucleus (yellow), Sérsic bulge (red) and exponential disc (blue).

models are less general than orbit-based models, but are much less computationally expensive and still provide good descriptions of galaxies dominated by stars on disc-like orbits even if dynamically hot as in lenticular galaxies (e.g., Cappellari 2008). On the other hand, the Jeans models take into account the two-dimensional information in the stellar kinematic maps as well as integration along the line-of-sight. In this way, we compare the resulting circular velocity curves with those obtained through ADC to investigate the validity of the assumptions underlying the simpler ADC approach.

In Section 3.2, we adopt the multi-Gaussian expansion (MGE) method to the surface brightness of the galaxies. Their stellar kinematics are estimated in Section 3.3. The applications of axisymmetric Jeans equations and asymmetric drift correction are presented in Section 3.4.1 and Section 3.4.2. In Section 3.5, we then compare the circular velocity curves from both modelling approaches. The possible reasons for the significant differences we find are discussed in Section 4.6, and we draw our conclusions in Section 3.7.

## 3.2 SURFACE BRIGHTNESS PARAMETRISATION

We parameterise each galaxy’s stellar surface brightness through the multi-Gaussian expansion (MGE) method described in Section 2.5.2, using the implementation of Cappellari (2002). We use the near-infrared  $H$ -band surface brightness profiles derived by Ganda et al. (2009) of the 18 SAURON galaxies. However, we use the online available source for photometric images of Sloan Digital Sky Survey (SDSS)<sup>1</sup> to obtain the surface brightness of CALIFA galaxies. The SDSS

<sup>1</sup><http://www.sdss.org/>

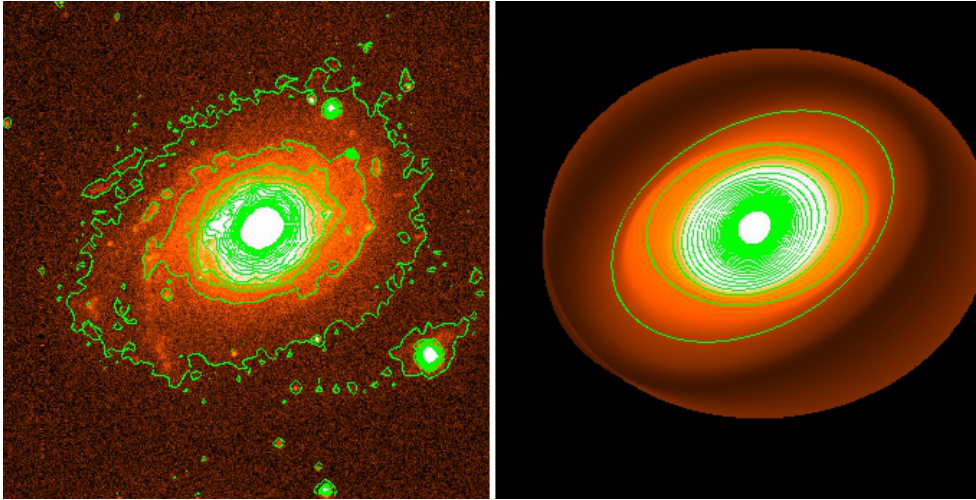


**Figure 3.2:** *Left:* r-band SDSS image of CALIFA galaxy NGC 0001, with surface brightness contours overlaid. *Right:* Smooth light distribution of the surface brightness of NGC 0001 obtained by *ellipse* task of IRAF package, aiming to discard the presence of bars, rings, spiral arms and foreground stars. Overplotted are the contours of the multi-Gaussian expansion models.

data come from the Data Release 8 (DR8)<sup>2</sup> of the survey, *r*-band photometry with applied flux calibration and sky subtraction.

The galaxies in our sample often contain a significant amount of interstellar dust, which is mostly transparent at near-infrared wavelengths (Rieke & Lebofsky 1985). Additionally, the near-infrared is a better tracer of the stellar mass in galaxies as the light is dominated by old stars (Frogel 1988; Rix & Zaritsky 1995; Lilly 1989).

**SAURON galaxies:** Ganda et al. (2009) decompose each galaxy’s profile as the superposition of an exponential disc and a Sérsic bulge. Most of the galaxies (16 out of 18) display a clear light excess above the Sérsic fit to the bulge, which can be attributed to a bright nuclear star cluster (Böker et al. 2002). To construct the MGE models of SAURON galaxies, we fit one-dimensional gaussians to the analytical surface brightness profiles of Sersic bulge and exponential disc, including an one additional circular gaussian fit to the light excess in the centre. We used 10 gaussians for each disc, a range between 13 and 19 for the bulges. The calculated galaxy inclination (eq. 3.1) from the flattening of the ellipticity, measured separately for bulge and disc, we deproject the one-dimensional gaussians into two-dimensional via the galaxy’s inclination. We converted the resulting peak surface brightnesses of the gaussians into physical units of  $L_{\odot}\text{pc}^{-2}$  using the absolute magnitude of the Sun  $M_{H,\odot} = 3.32$  (Binney & Merrifield 1998b).

In Figure 3.1, we show the MGE light models of two representative galaxies in our sample. The green asterisks indicate their observed light profiles. The black thick curves represent the sum of

<sup>2</sup><http://www.sdss3.org/dr8/>

the individual gaussians (dotted lines) of the three components: nucleus (yellow), Sérsic bulge (red), and exponential disc (blue). NGC 628 (left panels) is an example of a very good fit to the data, which is typical for the majority of our galaxies. However, there are a few exceptions with mismatches due to bars or prominent spiral arms. These are NGC 864 (Figure 3.1, right panel), NGC 772, and NGC 1042. Nevertheless, we considered the MGE fits to these three galaxies to be satisfactory for our needs, because fitting non-symmetric features could lead to uneven representation of the galaxies' surface brightness profiles, and hence, gravitational potentials.

**CALIFA galaxies:** We used *ellipse* task of IRAF package to smooth the light distribution of the 8 galaxies before modeling their surface brightness distribution with the multi-Gaussian expansion method (Monnet et al. 1992; Emsellem et al. 1994). This is needed in the case of galaxies with complex structure or having features like bars, rings and spiral arms. We construct their light models by fitting ellipses to the surface brightness of the galaxy with fixed center, position angle and ellipticity. At last, on the smooth light models of the CALIFA galaxies, we applied the multi-Gaussian expansion method to parameterize their observed surface brightness (e.g., see Fig. 3.2).

In order to deproject the surface density distributions, we estimate the inclination  $i$  of each galaxy in the complete sample. A usual procedure to derive  $i$  from the axial ratio of the disc is (Hubble 1926):

$$\cos^2 i = \frac{q^2 - q_o^2}{1 - q_o^2}, \quad (3.1)$$

where  $q = 1 - \epsilon$  is the observed ratio of minor-to-major diameter of the disc ( $\epsilon$  is the observed ellipticity) and  $q_o$  is the relative size of the smallest axis of the three-dimensional galaxy disc (assumed to be an oblate spheroid). We adopt the value  $q_o = 0.2$  for our galaxies (Holmberg 1958). For the majority of the galaxies we used the ellipticity of the disc to infer the inclination, but in the cases where the bulge was flatter (e.g. NGC 3346, NGC 4487, NGC 4775 and NGC 5668), we used its ellipticity instead. Our inferred inclinations are listed in Table 3.1 for both samples.

### 3.3 STELLAR KINEMATIC MAPS

We measured the stellar kinematics using the penalised pixel-fitting (pPXF) method of Cappellari & Emsellem (2004). As spectral templates for SAURON galaxies we used a sub-sample of the MILES stellar library (Sánchez-Blázquez et al. 2006; Falcón-Barroso et al. 2011), containing  $\sim 115$  stars that span a large range in atmospheric parameters like surface gravity, effective temperature and metallicity. Instead, we use  $\sim 60$  MILES single stellar population models as spectral templates for CALIFA sample (Vazdekis et al. 2010; Falcón-Barroso et al. 2011). In this case, the stellar emission is a result of the combination of different single-stellar populations (SSP), and/or the result of a particular star-formation history (Sánchez et al. 2012b).

**Table 3.1:** Properties of our sample of 18 galaxies: (1) Galaxy name; (2) Hubble type of CALIFA galaxies (Husemann et al. 2013) and SAURON galaxies (NASA/IPAC Extragalactic Database, NED); (3) Galactocentric distance in Mpc (NED); (4) Photometric position angle in degrees from SDSS images (Ganda et al. 2009); (5) Inclination in degrees (see Sect. 3.2); (6) Systemic velocity in  $\text{kms}^{-1}$ , measured using the enforce point-symmetry method (Sect. 3.3); (7) galaxy MGE effective radius in kpc (Sect. 2.5.2).

Name (1)	Type (2)	D (3)	PA (4)	$i$ (5)	$V_{\text{sys}}$ (6)	$R_e$ (7)
CALIFA						
NGC 6125	E	68.6	42	63	4689	5.3
NGC 6411	E	54.9	77	66	3705	4.9
NGC 5966	E	63.1	157	63	4498	4.9
NGC 1167	SA0	69.1	43	57	4704	10.1
NGC 0776	SBb	68.8	45	64	4842	6.7
NGC 0036	SBb	84.3	82	67	5954	7.5
IC 1683	SABb	68.7	71	69	4815	3.2
NGC 0001	SABc	64.7	108	78	4495	3.3
SAURON						
NGC 488	SA(r)b	32.1	5	41	2299	8.4
NGC 772	SA(s)b	35.6	126	50	2506	9.3
NGC 4102	SAB(s)b	15.5	42	58	838	1.1
NGC 5678	SAB(rs)b	31.3	5	60	1896	3.7
NGC 3949	SA(s)bc	14.6	122	52	808	1.4
NGC 4030	SA(s)bc	21.1	37	42	1443	3.1
NGC 2964	SAB(r)bc	20.6	96	59	1324	2.1
NGC 628	SA(s)c	9.8	25	37	703	4.3
NGC 864	SAB(rs)c	21.8	26	48	1606	4.1
NGC 4254	SA(s)c	19.4	50	44	2384	4.9
NGC 1042	SAB(rs)cd	18.1	174	46	1404	6.4
NGC 3346	SB(rs)cd	18.9	100	42	1257	5.1
NGC 3423	SA(s)cd	14.7	41	41	1001	3.8
NGC 4487	SAB(rs)cd	14.7	77	55	1016	3.5
NGC 2805	SAB(rs)d	28.2	125	42	1742	9.0
NGC 4775	SA(s)d	22.5	96	35	1547	3.2
NGC 5585	SAB(s)d	8.2	38	52	312	2.8
NGC 5668	SA(s)d	23.9	120	38	1569	4.4

The pPXF method fits a non-negative linear combination of these stellar template spectra, convolved with Gaussian velocity distribution, to each galaxy spectrum by chi-square minimisation. The spectral regions affected by emission lines were masked out during this process. A low-order polynomial (generally of order six) is included in the fit to account for small differences in the flux calibration between the galaxy and the template spectra. Thus we obtain the stellar mean velocity ( $V$ ) and stellar velocity dispersion ( $\sigma$ ) for each bin. Their errors are estimated through Monte-Carlo simulations with noise added to the galaxy's spectrum.

The PMAS/PPAK instrumental resolution is  $\sim 85 \text{ km s}^{-1}$  and the measured velocity dispersions of the 8 CALIFA galaxies is comparable and above this level. However, the measured velocity dispersions of the 18 late-type galaxies in many cases are well below the level of the SAURON instrumental resolution of  $105 \text{ km s}^{-1}$ . One might be concerned that velocity dispersions significantly below the instrumental resolution cannot be reliably measured. This problem was successfully resolved by Emsellem et al. (2004). They tested the uncertainties on the measured  $\sigma$  via Monte-Carlo simulations. The results showed that for a spectrum with  $(S/N) \approx 60$  and  $\sigma \approx 50 \text{ km s}^{-1}$ , the pPXF method will output velocity dispersions differing from the intrinsic ones by  $10 \text{ km s}^{-1}$ , a value within the measured errors.

In Fig. 3.3 and Fig. 3.4 we show the stellar kinematics maps of our complete sample of 26 E–Sd galaxies. The first column shows the stellar flux in arbitrary units and in logarithmic scale. The next two columns display  $V$  and  $\sigma$  maps in  $\text{km s}^{-1}$  respectively. We over-plotted the surface brightness contours of the galaxies as derived from their intensity maps.

For some of our galaxies the centre was not accurately determined during the data reduction due to foreground stars and dust lanes, which in some cases caused a significant offset in the measurement of the systemic velocity  $V_{\text{sys}}$ . Therefore, we use the velocity field symmetrisation method described in Appendix A of van den Bosch & de Zeeuw (2010) to estimate a robust  $V_{\text{sys}}$ . This method assumes that the velocity field is orthogonal in respect to the galaxy centre, uncorrelated and varies linearly along the spatial coordinates. Then, for each spaxel that has a counterpart, it computes their weighted mean velocities and combined errors (upper limit of  $2.0 \text{ km s}^{-1}$ ). In this way we obtain a robust estimate of  $V_{\text{sys}}$  for each galaxy (see Table 3.1). Galaxies with more concentrated light distribution generally have larger central peaks in their velocity dispersion fields. Elliptical galaxies usually have outwards decreasing  $\sigma$  (D'Onofrio et al. 1995) and this is also the case for many early-type spirals, as a result of a centrally concentrated bulge. But for the latest type spirals we expect  $\sigma$  field to be flat due to their lower bulge-to-disc ratios or with a central dip, because of cold components or counter-rotating discs (Falc3n-Barroso et al. 2006). In comparison with early-type galaxies, the bulges of the late-type spirals are smaller and have lower surface brightness (Yoachim & Dalcanton 2006; Ganda et al. 2009).

Most of our Sb–Sc galaxies have regular velocity fields with well defined axisymmetric rotation

and high amplitude, while Sd velocity fields show more complex structure and lower amplitude of rotation. In our complete sample we have three types of  $\sigma$  behaviour: decreasing outward (e.g., NGC 0036, IC 1683, NGC 488, NGC 4102), a central  $\sigma$ -dip (e.g., NGC 6411, NGC 772, NGC 5678, NGC 4030) or flat (e.g., NGC 6125, NGC 5966, NGC 628, NGC 4255).

## 3.4 DYNAMICAL MODELING

### 3.4.1 AXISYMMETRIC JEANS EQUATIONS

As described in Sect. 2.5, we use a solution of the axisymmetric Jeans equation based on a Multi-Gaussian Expansion (MGE) of the intrinsic luminosity density to predict the observed second velocity moment  $V_{\text{rms}} = \sqrt{V^2 + \sigma^2}$  (Cappellari 2008), with the following parameters: inclination  $i$ , constant meridional plane velocity anisotropy  $\beta_z$  and constant mass-to-light ratio  $\Upsilon_{\text{tot}}$  within the galaxy. In the fourth and fifth column of Fig. 3.3 we show the observed and the best fitting  $V_{\text{rms}}$  maps with over-plotted MGE contours. The MGE contours are aligned with the surface brightness contours for all of the galaxies.

To obtain our best fit models, we vary  $\beta_z$  within the range of  $-0.6$  to  $+0.6$  and apply the  $\chi^2$ -minimisation method to test the goodness of the fits. In Fig. 3.5 and Fig. 3.5 we present well defined  $\chi^2$ -minima for all CALIFA galaxies and more than half of SAURON galaxies within  $3\text{-}\sigma$  confidence level (dashed curve). For the rest, we assume an isotropic Jeans model, i.e.,  $\beta_z = 0$  (NGC 772, NGC 4030, NGC 628, NGC 4254, NGC 3346, NGC 5585, NGC 5668). In Table 3.2 are listed the best fitting  $\Upsilon_{\text{tot}}$  in r- and H-band for CALIFA and SAURON galaxies, respectively, with the corresponding velocity anisotropy  $\beta_z$ .

Our second velocity moment  $V_{\text{rms}}$  best fits are in the cases of E–Sc galaxies (e.g. NGC 4102, NGC 5678, and NGC 2964, characterised by a fast rotating disc) and getting worse for Scd and Sd galaxies. The median value of the residual  $V_{\text{rms}}$  map varies from E–Sd with  $\sim 5\%$ – $25\%$ . This might be due to an increased galaxy’s non-axisymmetry throughout the Hubble sequence.

### 3.4.2 ASYMMETRIC DRIFT CORRECTION: RADIAL PROFILES

To obtain circular velocity curves for our sample of galaxies using the asymmetric drift correction (ADC, see Sect. 2.5.3), we need their kinematic profiles along the projected major axis. We used the kinemetry package of Krajnović et al. (2006) that is based on harmonic expansion of two-dimensional maps along ellipses. We extracted the observed mean line-of-sight  $V$  and  $\sigma$  profiles

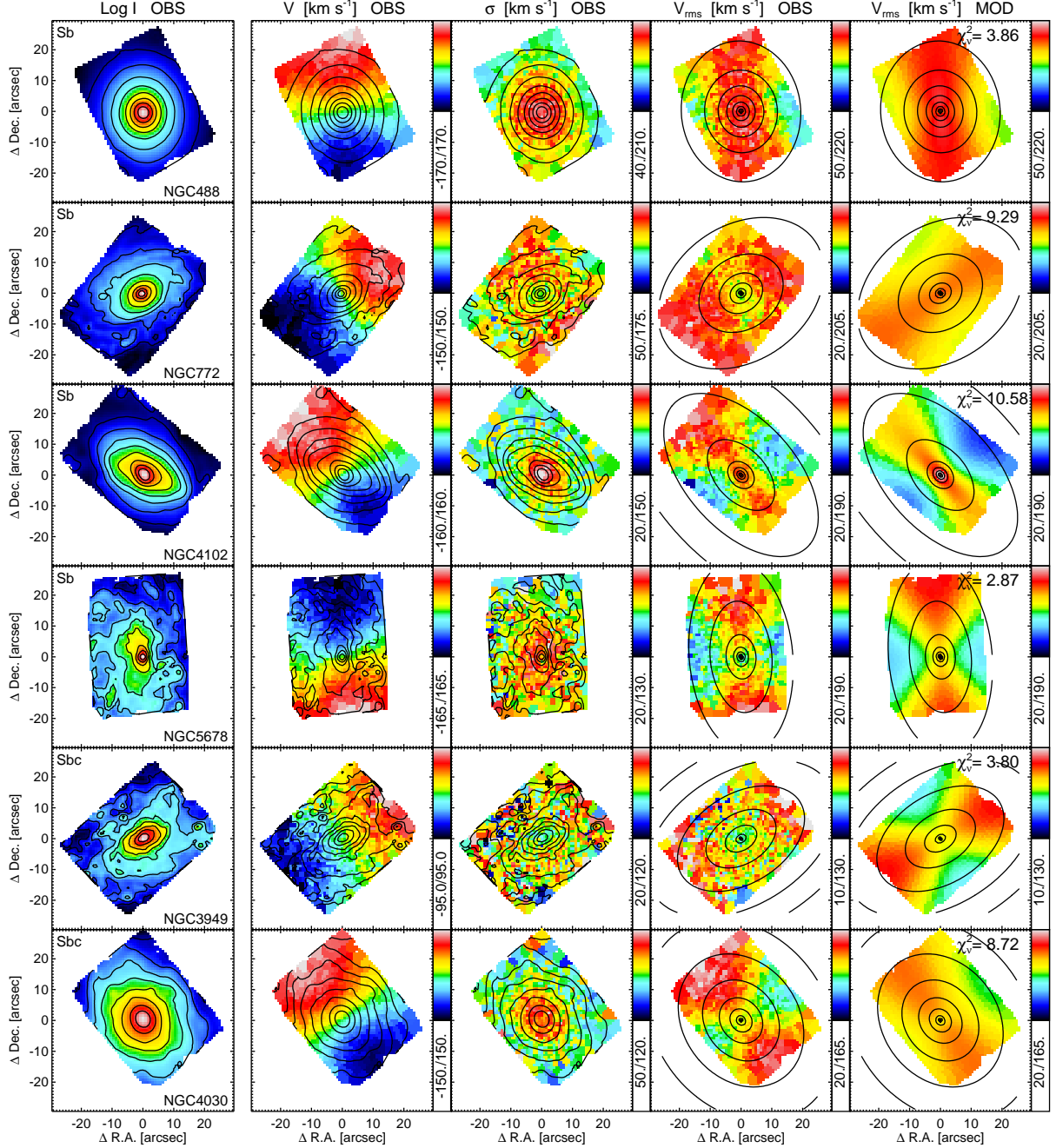


**Figure 3.3:** Stellar kinematics and second moment maps of SAURON sample of 18 galaxies. First column: stellar flux derived from the collapsed data cubes; second and third column: observed mean line-of-sight velocity and velocity dispersion; fourth and fifth column: second moment maps  $V_{\text{rms}} = \sqrt{V^2 + \sigma^2}$  of the data and the model with overplotted MGEs contours.

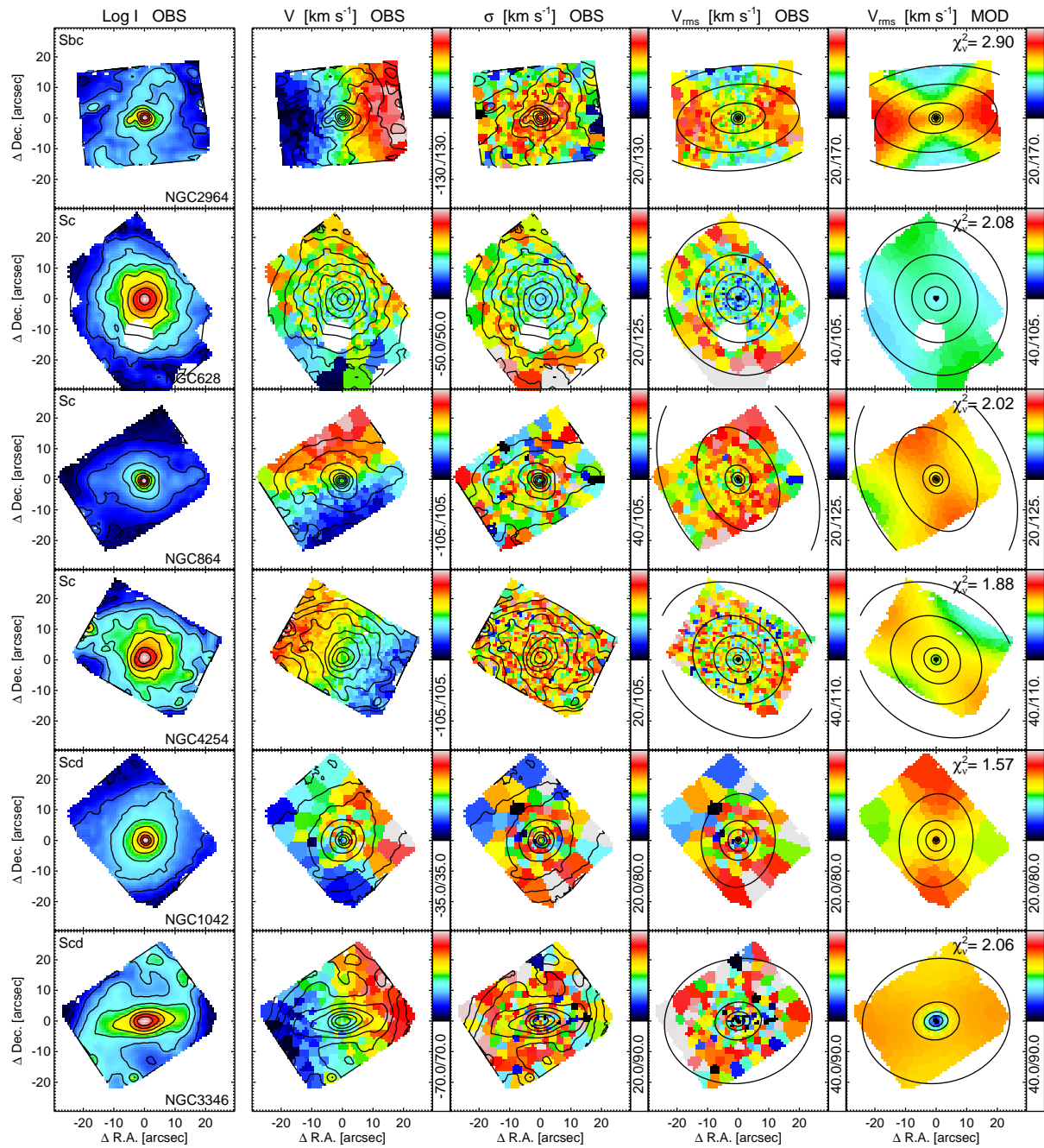


Figure 3.3: – continuation

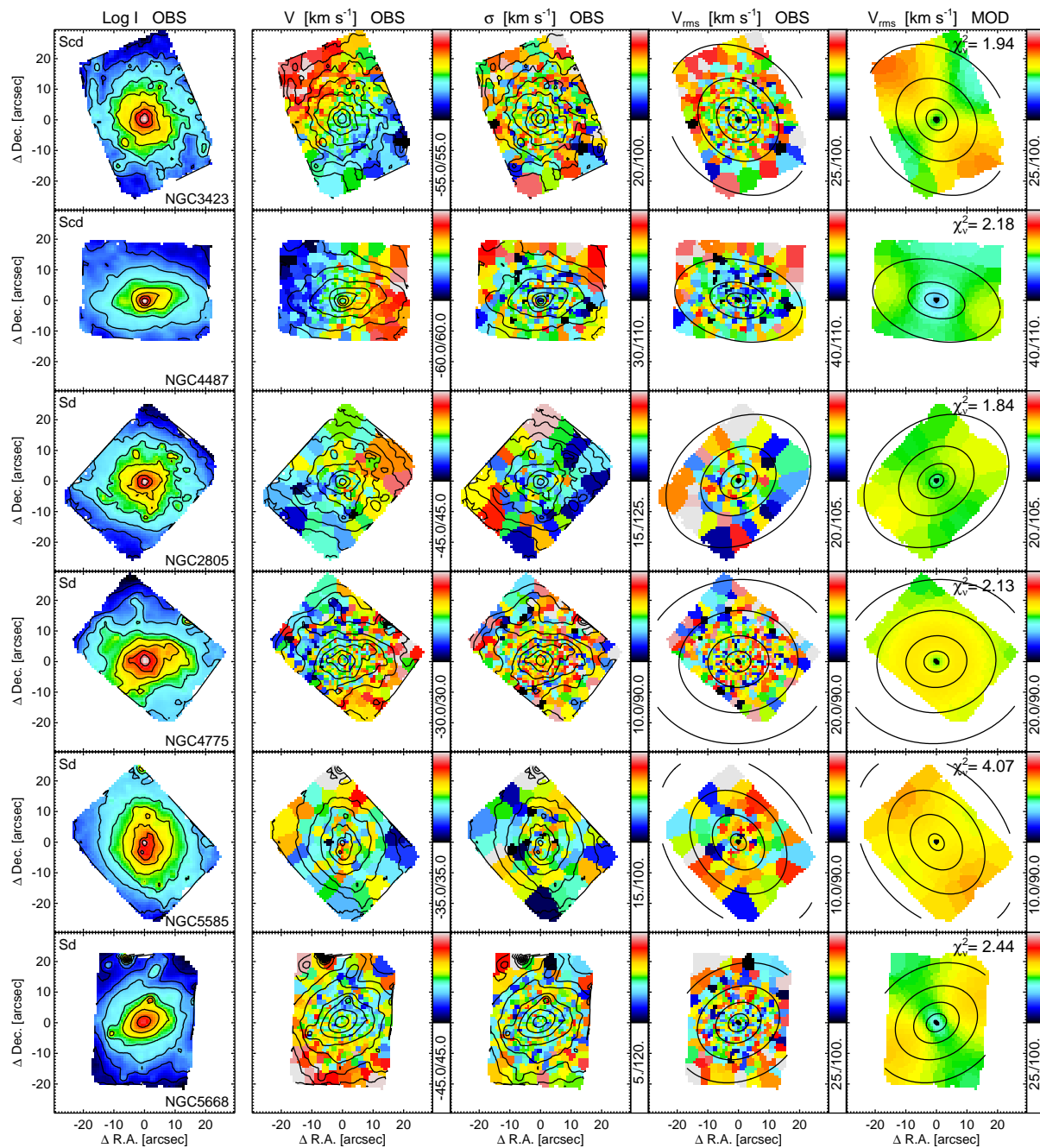
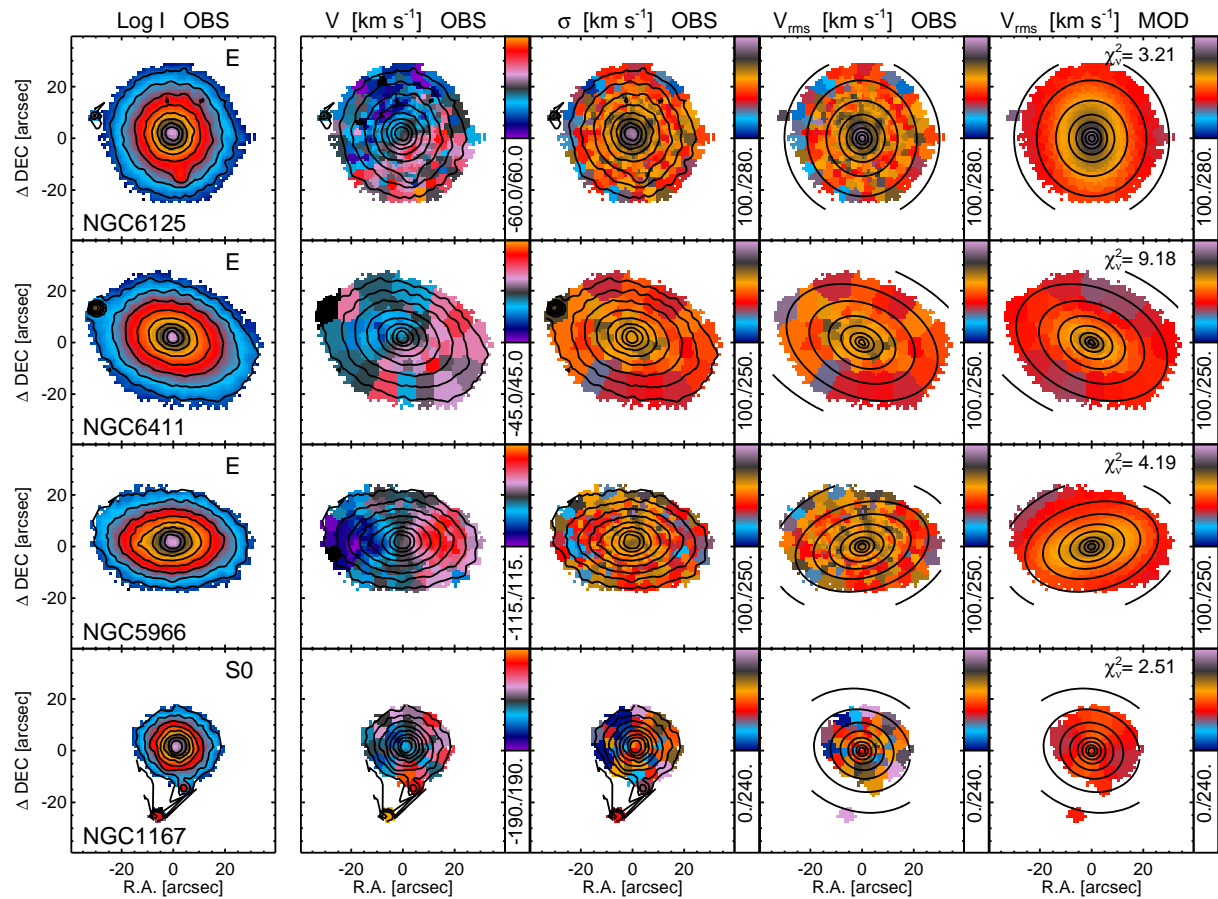


Figure 3.3: – continuation



**Figure 3.4:** Stellar kinematics and second moment maps of CALIFA sample of 8 galaxies. First column: stellar flux derived from the collapsed data cubes; second and third column: observed mean line-of-sight velocity and velocity dispersion; fourth and fifth column: second moment maps  $V_{\text{rms}} = \sqrt{V^2 + \sigma^2}$  of the data and the model with overplotted MGEs contours.

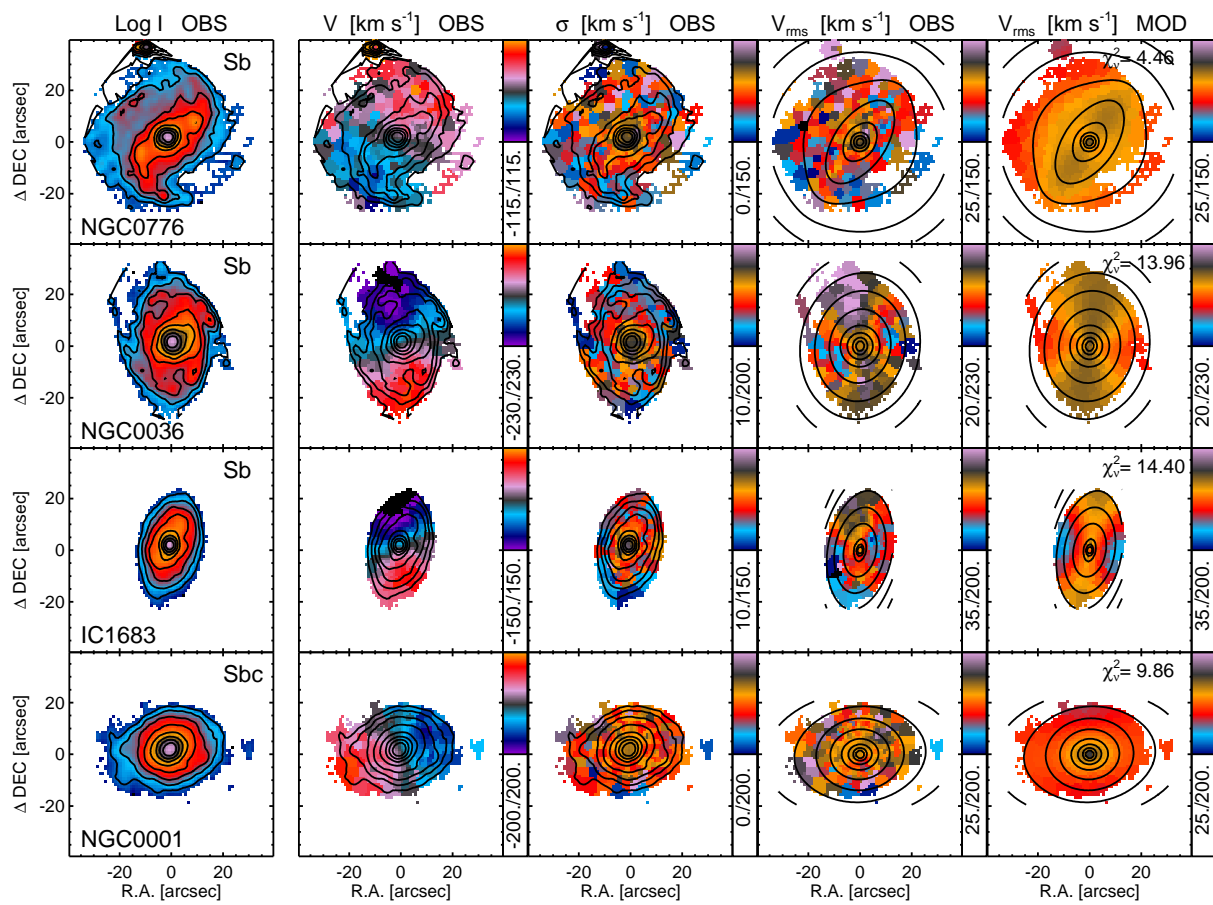
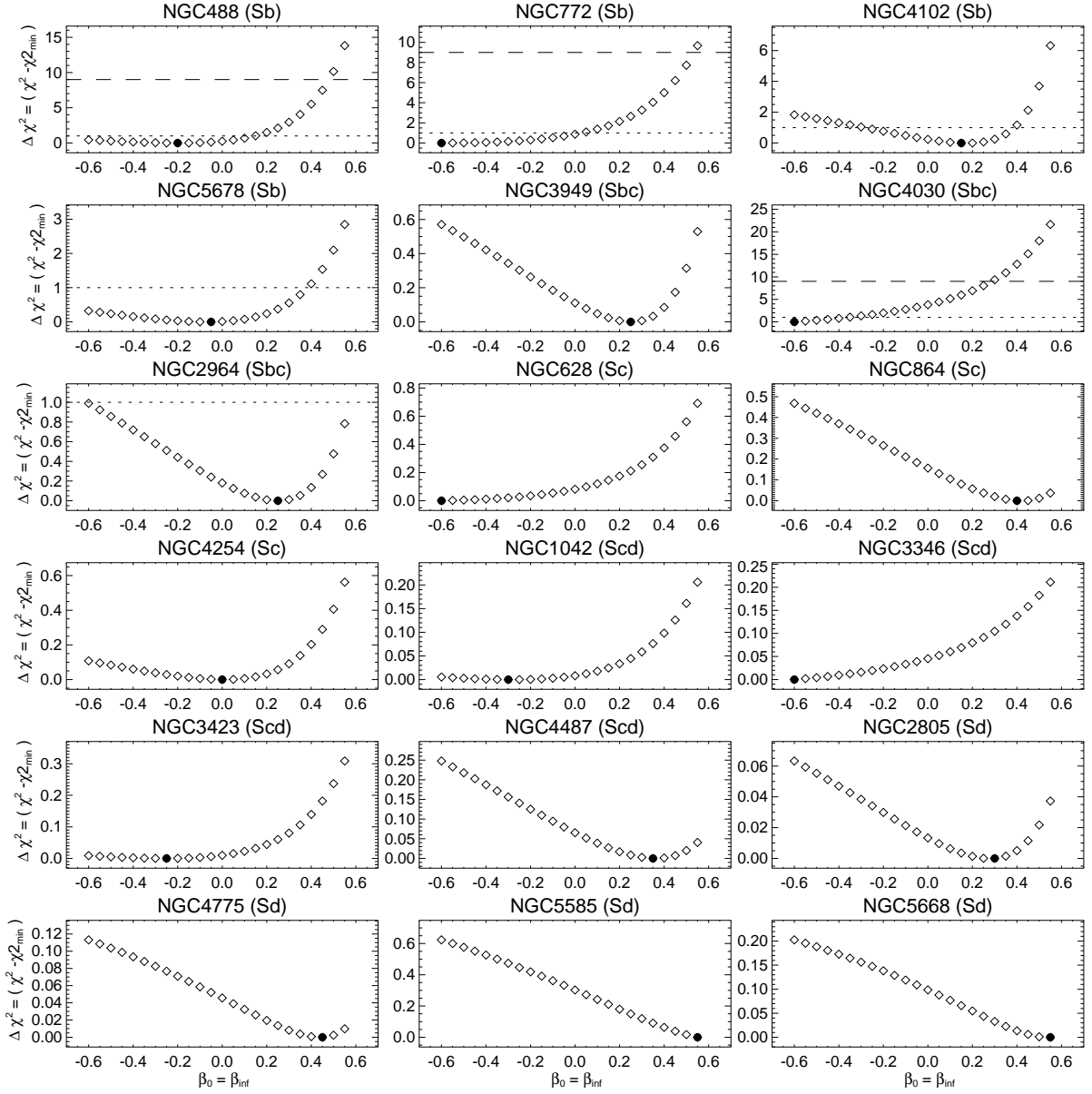
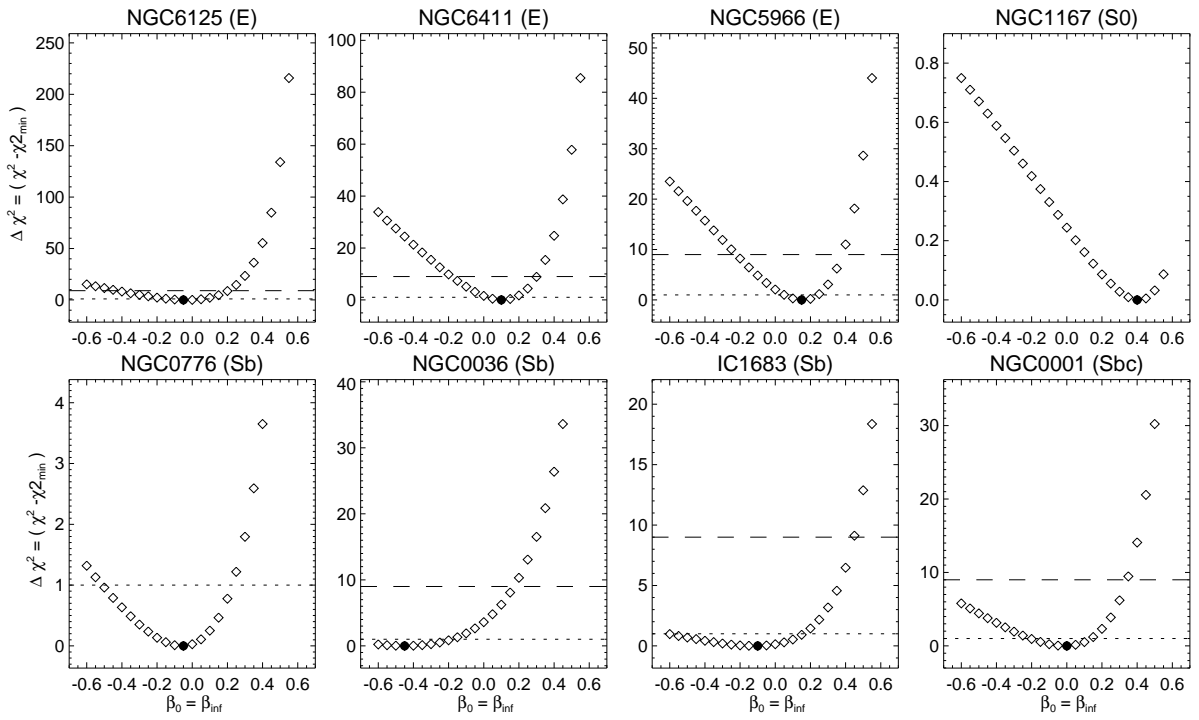


Figure 3.4: – continuation



**Figure 3.5:** Best-fitting Jeans anisotropy of SAURON galaxies.  $\Delta\chi^2 = \chi^2 - \chi^2_{min}$ , describing the agreement between the data and the models, is plotted against the velocity anisotropy parameter  $\beta_z$ . The open squares represents the  $\chi^2$  of the Jeans models. The filled squares show the minimum of the  $\chi^2$  value. The dotted and dashed lines indicate the level  $\Delta\chi^2 = 1$  and  $\Delta\chi^2 = 9$ , respectively, which corresponds to the  $1\sigma$  and  $3\sigma$  confidence level for 1 degree of freedom. We assume an isotropic Jeans model, i.e.,  $\beta_z = 0$  for galaxies without clear  $\chi^2$ -minima (NGC 772, NGC 4030, NGC 628, NGC 4254, NGC 3346, NGC 5585, NGC 5668).



**Figure 3.6:** Best-fitting Jeans anisotropy of CALIFA galaxies.  $\Delta\chi^2 = \chi^2 - \chi^2_{min}$ , describing the agreement between the data and the models, is plotted against the velocity anisotropy parameter  $\beta_z$ . The open squares represents the  $\chi^2$  of the Jeans models. The filled squares show the minimum of the  $\chi^2$  value. The dotted and dashed lines indicate the level  $\Delta\chi^2 = 1$  and  $\Delta\chi^2 = 9$ , respectively, which corresponds to the  $1\sigma$  and  $3\sigma$  confidence level for 1 degree of freedom. All galaxies have clear  $\chi^2$ -minima.

**Table 3.2:** Fitting functions' parameters and dynamical modelling results: (1) Galaxy name; (2) Hubble type of CALIFA galaxies (Husemann et al. 2013) and SAURON galaxies (NASA/IPAC Extragalactic Database, NED); (3) and (4)  $\overline{v_\phi}$  power-law fit with  $v_\infty$  in  $\text{km s}^{-1}$  and  $R_c$  in arcsec (see Eq. 3.5); (5)  $\overline{v_\phi}$  linear fit with slope  $k_v$  (see Eq. 3.6); (6) and (7)  $\sigma_R$  linear fit to the deprojected line-of-sight velocity dispersion with y-intercept  $\sigma_0$  in  $\text{km s}^{-1}$  and slope  $k_\sigma$  (see Eq. 3.7); (8) and (9)  $\sigma_R$  exponential fit to the deprojected line-of-sight velocity dispersion with y-intercept  $\sigma_1$  in  $\text{km s}^{-1}$  and scale radius  $h$  (see Eq. 3.8); (10) JAM best fit total dynamical mass-to-light ratio in r-band for CALIFA and H-band for SAURON galaxies in solar units; (11) velocity anisotropy  $\beta_z$ ; (12) mass ratio between  $M_{\text{JAM}}$  and  $M_{\text{ADC}}$  at one-fifth of the MGE effective radius ( $R_e/5$ ).

Name (1)	Type (2)	$v_\infty$ (3)	$R_c$ (4)	$k_v$ (5)	$\sigma_0$ (6)	$k_\sigma$ (7)	$\sigma_1$ (8)	$h$ (9)	$\Upsilon_{\text{tot}}$ (10)	$\beta_z$ (11)	$\frac{M_{\text{JAM}}}{M_{\text{ADC}}}$ (12)
<b>CALIFA</b>											
NGC 6125	E	40.15	8.12	–	263.94	0.74	–	–	6.16	-0.05	1.8
NGC 6411	E	19.36	4.02	–	289.12	-0.53	–	–	5.84	0.10	1.4
NGC 5966	E	122.19	18.70	–	201.95	1.02	–	–	7.54	0.15	2.6
NGC 1167	SA0	–	–	20.33	97.08	2.22	–	–	3.00	0.40	1.7
NGC 0776	SBb	53.52	5.07	–	–	–	129.36	61.48	3.23	-0.05	2.1
NGC 0036	SBb	240.35	8.80	–	–	–	178.86	24.00	6.20	-0.45	1.3
IC 1683	SABb	169.49	7.61	–	–	–	129.52	15.81	4.93	-0.10	1.7
NGC 0001	SABc	129.52	5.82	–	141.57	0.10	–	–	3.51	0.00	2.0
<b>SAURON</b>											
NGC 488	SA(r)b	220.44	8.26	–	234.94	-2.53	–	–	1.16	-0.20	1.3
NGC 772	SA(s)b	180.73	5.81	–	173.79	0.69	–	–	0.95	0.00	1.6
NGC 4102	SAB(s)b	156.29	4.27	–	156.32	-1.67	–	–	0.61	0.15	1.8
NGC 5678	SAB(rs)b	185.40	8.94	–	129.45	-0.70	–	–	1.23	-0.05	2.2
NGC 3949	SA(s)bc	131.66	19.45	–	63.08	2.20	–	–	1.46	0.25	4.1
NGC 4030	SA(s)bc	217.06	9.00	–	101.56	1.60	–	–	0.71	0.00	1.6
NGC 2964	SAB(r)bc	208.42	16.16	–	100.30	0.39	–	–	1.41	0.25	4.8
NGC 628	SA(s)c	–	–	0.96	56.92	1.28	–	–	1.05	0.00	4.6
NGC 864	SAB(rs)c	153.80	12.56	–	79.68	1.14	–	–	1.45	0.40	2.2
NGC 4254	SA(s)c	91.33	12.68	–	75.26	1.18	–	–	0.46	0.00	3.5
NGC 1042	SAB(rs)cd	–	–	1.45	56.97	0.12	–	–	1.92	-0.30	2.8
NGC 3346	SB(rs)cd	–	–	4.29	61.80	-0.09	–	–	2.02	0.00	1.4
NGC 3423	SA(s)cd	126.32	40.69	–	58.36	0.89	–	–	2.18	-0.25	2.9
NGC 4487	SAB(rs)cd	–	–	3.07	67.65	-0.22	–	–	2.31	0.35	1.7
NGC 2805	SAB(rs)d	22.13	2.64	–	90.92	0.13	–	–	1.83	0.30	9.7
NGC 4775	SA(s)d	–	–	1.50	61.08	-0.24	–	–	1.04	0.45	2.0
NGC 5585	SAB(s)d	–	–	0.40	55.27	-0.21	–	–	5.03	0.00	3.0
NGC 5668	SA(s)d	–	–	2.06	55.65	0.53	–	–	1.75	0.00	2.9

along ellipses with fixed kinematic position angle, which matches the photometric PA, given in Table 3.1.

Then under the assumption of a 'thin-disc' ( $\partial \ln v / \partial \ln R \approx d \ln I / d \ln R$ ) we obtain the  $\overline{v}_\phi$  and  $\sigma_R$  from the observed  $V$  and dispersion  $\sigma$  as:

$$V = V_{\text{sys}} + \overline{v}_\phi \cos \phi \sin i, \quad (3.2)$$

$$\sigma^2 = \left( \sigma_R^2 \sin^2 \phi + \sigma_\phi^2 \cos^2 \phi \right) \sin^2 i + \sigma_z^2 \cos^2 i. \quad (3.3)$$

Given the inclination  $i$  and systemic velocity  $V_{\text{sys}}$ ,  $\overline{v}_\phi$  follows directly from  $V$  along the major axis ( $\phi = 0$ ). Following Appendix A of Weijmans et al. (2008), we get

$$\frac{\sigma^2}{\sigma_R^2} = 1 - (1 - \alpha_R) \times \left[ \frac{\cos^2 \phi \sin^2 i}{2} + \frac{\cos^2 i}{\kappa q_\phi^2 (1 + \alpha_R) + (1 - \alpha_R)} \right]. \quad (3.4)$$

Here  $\alpha_R = \partial \ln \overline{v}_\phi / \partial \ln R$  is the logarithmic radial gradient of  $\overline{v}_\phi$ . Given the inclination  $i$  and  $\kappa q_\phi^2 = 1$ ,  $\sigma_R$  follows from  $\sigma$  along the major axis ( $\phi = 0$ ).

In order to avoid numerical noise in the derivatives, we fit simple functional forms to  $\overline{v}_\phi$  and  $\sigma_R$  and use the resulting analytical derivatives. The adopted fitting functions serve mainly as a smooth and analytical parameterisation of the data.

As a fitting function for  $v_\phi$  we use the 'power-law' prescription of Evans & de Zeeuw (1994eq.2.11), which in the thin disc approximation ( $z = 0$ ) and assuming flat rotation curve, becomes

$$\overline{v}_\phi(R) = \frac{v_\infty R}{\sqrt{R_c^2 + R^2}}, \quad (3.5)$$

where  $v_\infty$  is the asymptotic velocity and  $R_c$  is the core radius. This model describes a rotation curve that increases linearly with radius  $\propto (v_\infty/R_c)R$  when  $R \ll R_c$ , and flattens to the value  $v_\infty$  when  $R \gg R_c$ . However, in several cases the velocity profile flattens out only in the last few points or not at all. This means that the core radius  $R_c$  cannot be well constrained and fitting Eq. (3.5) would lead to unphysical values for both  $R_c$  and  $v_\infty$ . Therefore, in those cases we are in the regime  $R \ll R_c$  and we use a linear relation instead

$$\overline{v}_\phi(R) = k_v R. \quad (3.6)$$

where  $k_v$  is the linear coefficient.

The appearance of  $\sigma$  and  $\sigma_R$  profiles are more varied than the  $V$  and  $\overline{v}_\phi$  profiles. Some velocity dispersion profiles show an almost-linear decrease or increase with radius on the whole radial range available, some are quite flat, others have a more complex behaviour that seems difficult

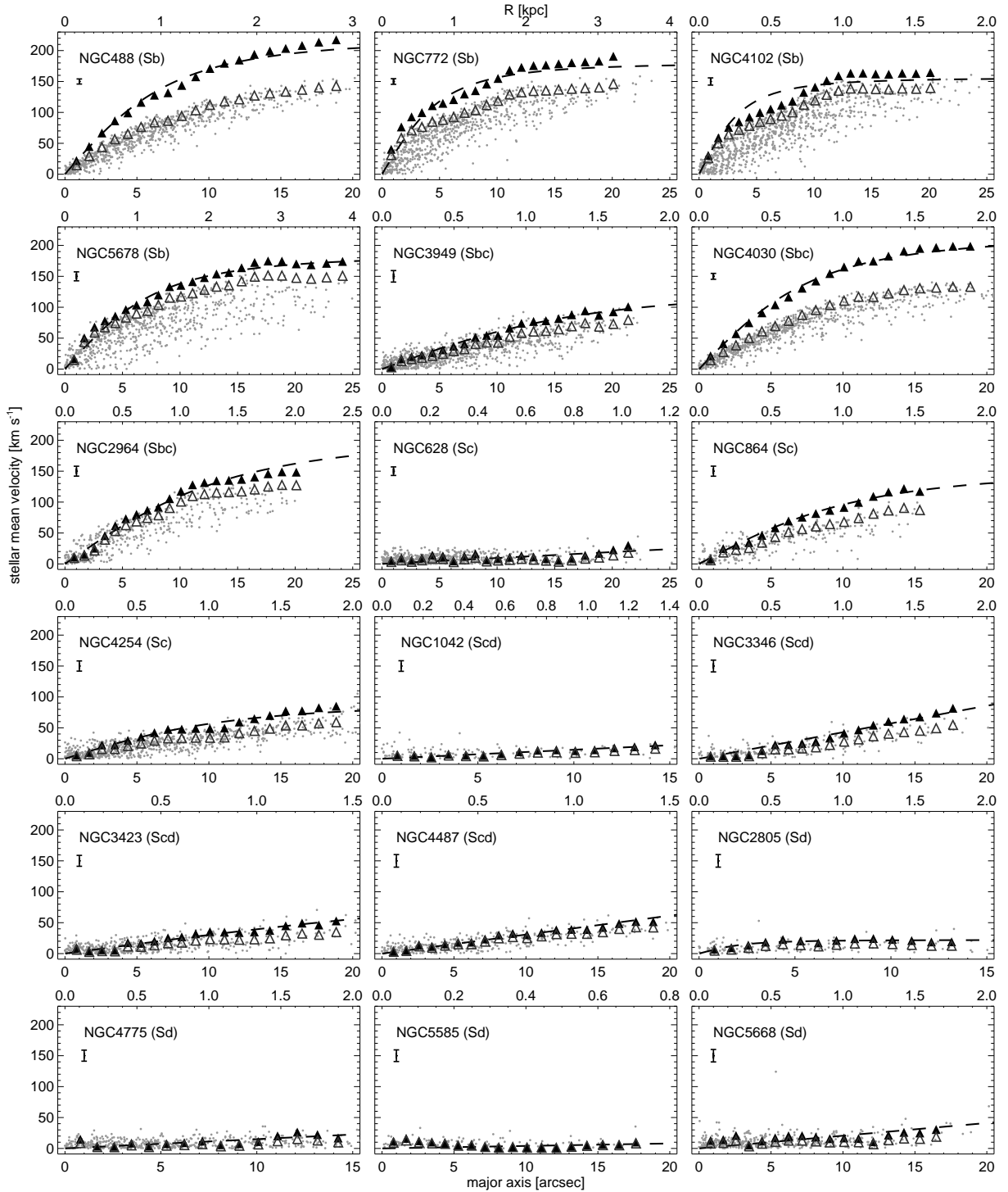


**Figure 3.7:** Profiles of the stellar mean line-of-sight velocity  $V$  (open triangles) and its deprojection  $\overline{v}_\phi$  (filled triangles) of SAURON sample. The grey symbols represent the absolute values of the velocity  $V$  in every bin with subtracted  $V_{sys}$ . The dashed curves are simple analytic fits to the deprojected azimuthal velocity  $\overline{v}_\phi$  profiles used to infer a smooth radial derivative. The bar indicates the uncertainty in the  $V$  profiles.

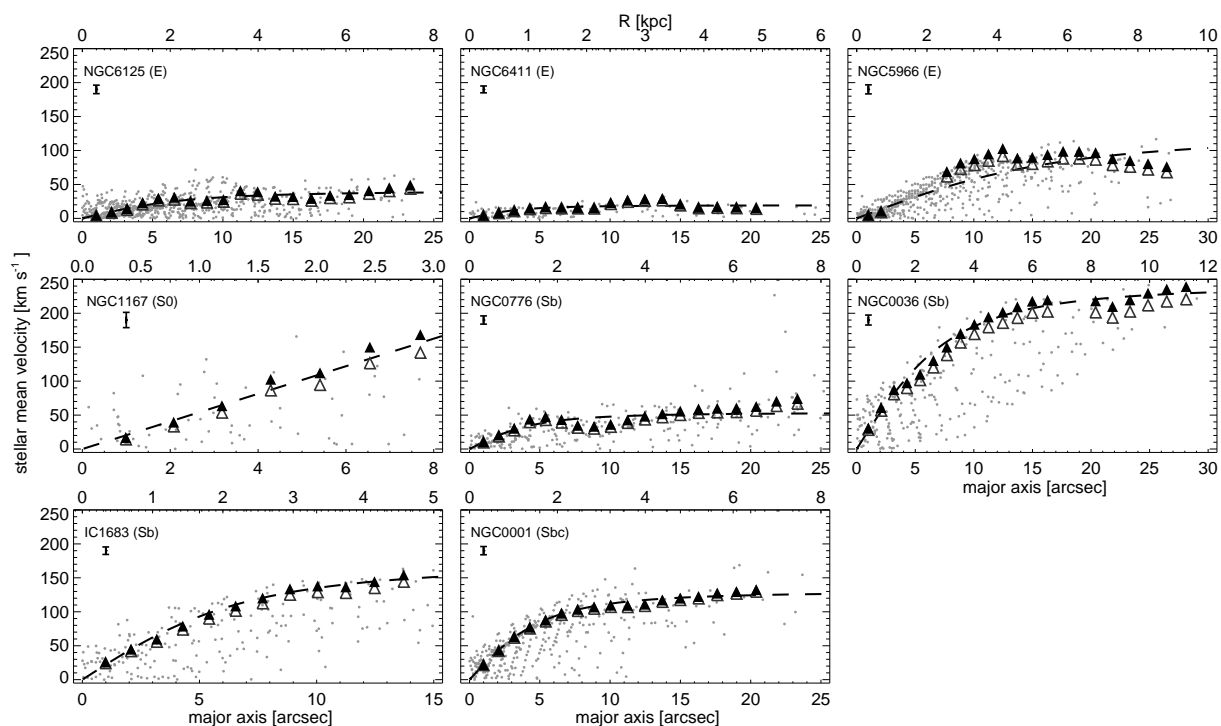


**Figure 3.8:** Profiles of the stellar mean line-of-sight velocity  $V$  (open triangles) and its deprojection  $\overline{v_\phi}$  (filled triangles) of CALIFA sample. The grey symbols represent the absolute values of the velocity  $V$  in every bin with subtracted  $V_{sys}$ . The dashed curves are simple analytic fits to the deprojected azimuthal velocity  $\overline{v_\phi}$  profiles used to infer a smooth radial derivative. The bar indicates the uncertainty in the  $V$  profiles.

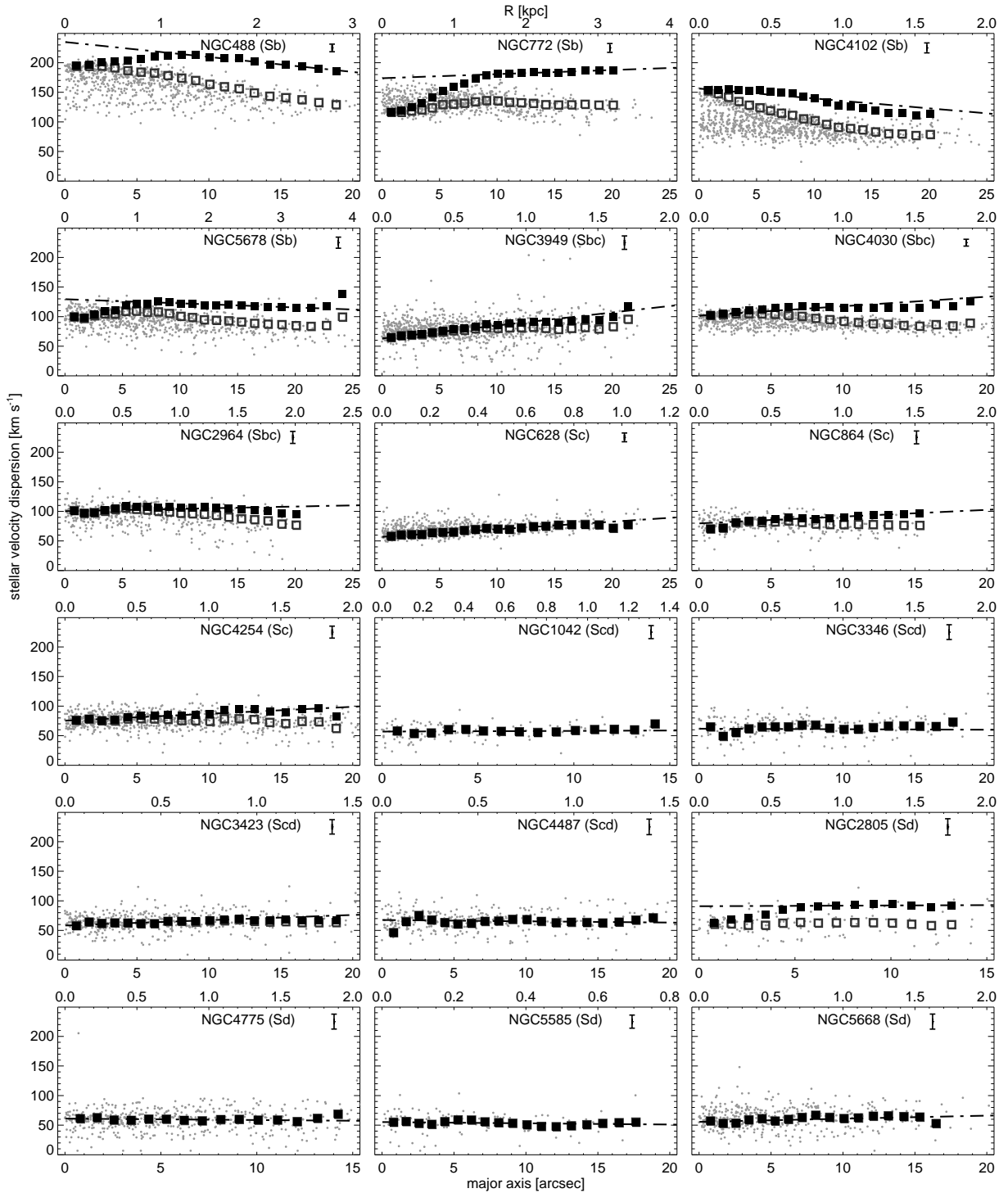


**Figure 3.9:** Profiles of the line-of-sight velocity dispersion  $\sigma$  (open squares) and its deprojection  $\sigma_R$  (filled squares) of SAURON sample. The grey symbols represent the values of the dispersion  $\sigma$  in every bin. The dot-dashed curve is a simple linear fit to the deprojected radial velocity dispersion  $\sigma_R$  profiles used to infer a smooth radial derivative. The bar indicates the uncertainty in the  $\sigma$  profiles.

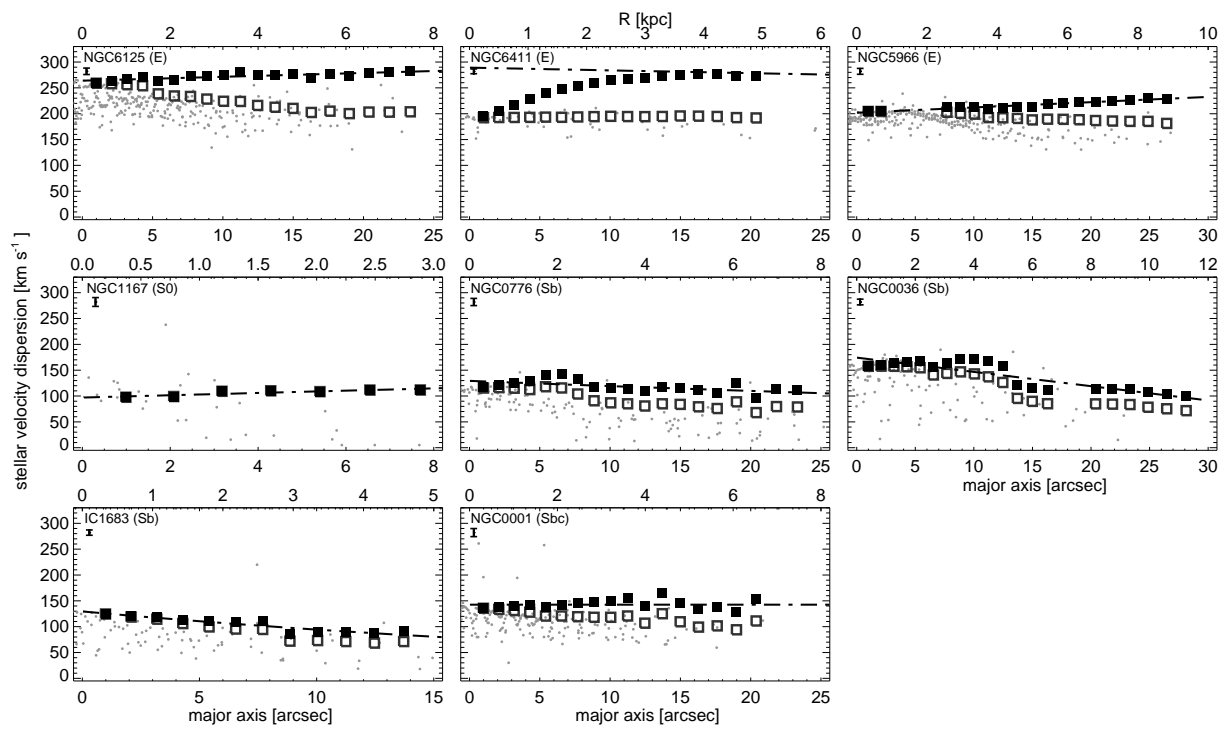


**Figure 3.10:** Profiles of the line-of-sight velocity dispersion  $\sigma$  (open squares) and its deprojection  $\sigma_R$  (filled squares) of CALIFA sample. The grey symbols represent the values of the dispersion  $\sigma$  in every bin. The dot-dashed curve is a simple linear fit to the deprojected radial velocity dispersion  $\sigma_R$  profiles used to infer a smooth radial derivative. The bar indicates the uncertainty in the  $\sigma$  profiles.

to reproduce with a single simple fitting function. Even so, for almost all cases, we fit a linear relation of the form

$$\sigma_R(R) = \sigma_0 + k_\sigma R \quad (3.7)$$

where  $\sigma_0$  and  $k_\sigma$  are free parameters.

For the galaxies NGC 0776, NGC 0036 and IC 1683, we better fit an exponential relation of the form

$$\sigma_R(R) = \sqrt{\sigma_1^2 \exp(-R/h)} \quad (3.8)$$

where  $\sigma_1$  and the scale radius  $h$  are free parameters.

In Fig. 3.7 and Fig. 3.8, we show the observed mean line-of-sight velocity  $V$  (open triangles) and deprojected azimuthal velocity  $\overline{v_\phi}$  (filled triangles) profiles for both SAURON and CALIFA samples. The grey symbols represent the absolute values of the observed velocity  $V$  in every bin. The dashed curves represent the best fit models to the radial profiles with parameters given in Table 3.2. The galaxies are ordered by their morphological type from E to Sbc in CALIFA and from Sb to Sd in SAURON sample. We observe that E–Sc galaxies (at  $R_e/5$ ) have higher observed velocity in contrast to Scd–Sd in the complete sample of 26 galaxies (except the Sb galaxy NGC 0776 that has a slow rotation). We adopt a power-law fitting function to most of the  $v_\phi$  radial profiles, except for the galaxies – NGC 628, NGC 1042, NGC 3346, NGC 4487, NGC 4775, NGC 5585 and NGC 5668, which require a linear function.

In Fig. 3.9 and Fig. 3.10, we present the observed line-of-sight velocity dispersion  $\sigma$  profiles (open squares) and its deprojection  $\sigma_R$  (filled squares) again for the both samples. The grey symbols correspond to the values of the  $\sigma$  in every bin. The dot-dashed curve is the best fit to  $\sigma_R$  with parameters given in Table 3.2. E–Sbc galaxies (at  $R_e/5$ ) are characterised by high observed velocity dispersion  $\sigma$  with respect to Sc–Sd. We consider that the linear fits to the  $\sigma_R$  profiles are descriptive, although we do not fit the central part of the  $\sigma_R$  profiles for some of the galaxies (NGC 6411, NGC 488, NGC 772, NGC 5678, NGC 2964, and NGC 2805). The reason comes from the presence of  $\sigma$  dips in their central parts as a result of a dynamical cold component or counter-rotating disc (Falc3n-Barroso et al. 2006). In these cases, it is difficult to find a suitable  $\sigma_R$  fitting function, which is able to reproduce the data over the full radial extent of the galaxies. However, neglecting the inner parts of these galaxies does not change the global estimation of their gravitational potential, but avoids incorrect determination of their logarithmic gradient slope.

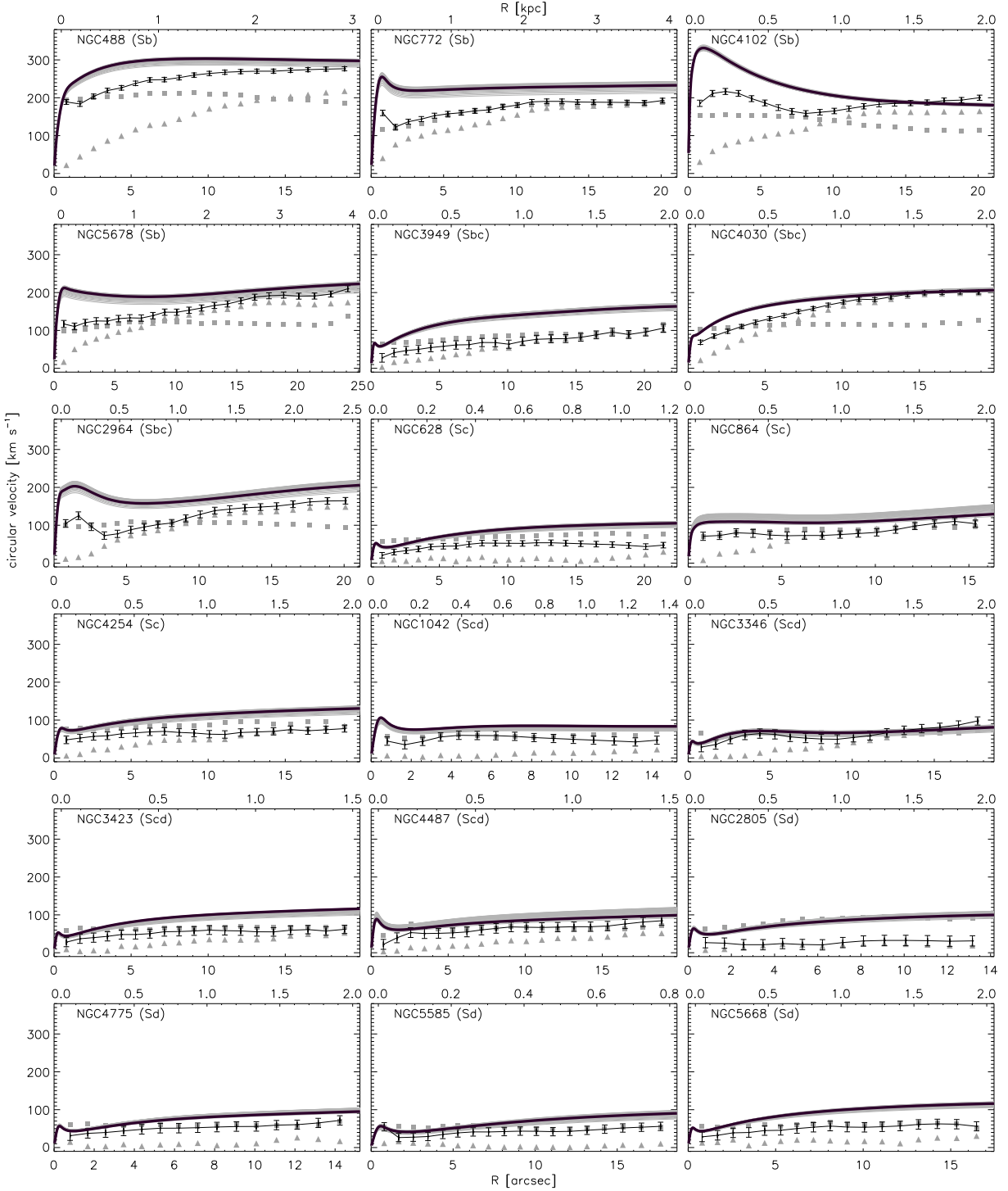


**Figure 3.11:** Circular velocity curves of SAURON galaxies, derived from the deprojected velocity  $\overline{v_\phi}$  and dispersion  $\sigma_R$  profiles along the major axis with triangles and squares, respectively (see Eq. 3.2 and Eq. 3.4). Thin solid curves are the circular velocity curves  $v_{c,ADC}$  from applying asymmetric drift corrections (Sect. 2.5.3), where the bars indicate their uncertainty. Thick solid curves are circular velocity curves  $v_{c,JAM}$  from the best fits ( $\chi^2$ -minimum) of axisymmetric Jeans solutions based on MGE models (Sect. 2.5). Their variation due to different assumed velocity anisotropies ( $-0.6 < \beta_z < +0.6$ ) within  $\Delta\chi^2 = 3\sigma$  confidence level, are given by the grey curves. There is a significant mismatch between the two models although taking into account their uncertainties, and  $v_{c,ADC}$  is always underestimated with respect to  $v_{c,JAM}$  (except for galaxy NGC 3346).

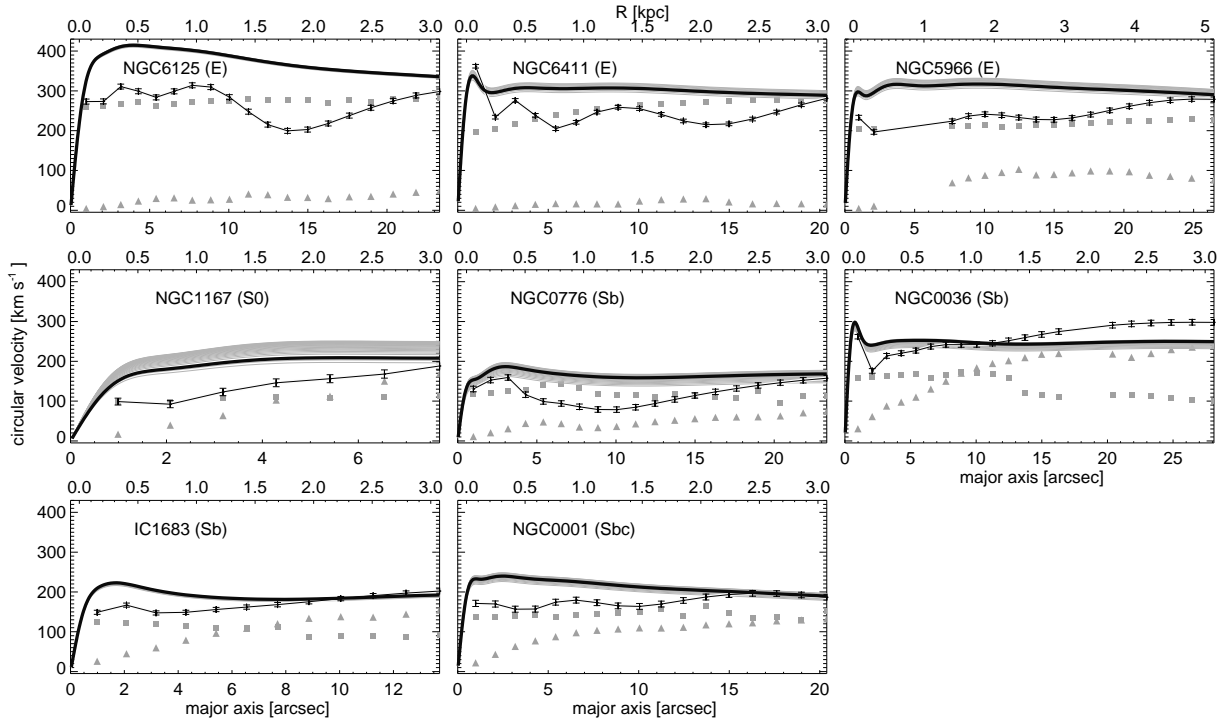


**Figure 3.12:** Circular velocity curves of CALIFA galaxies, derived from the deprojected velocity  $\overline{v_\phi}$  and dispersion  $\sigma_R$  profiles along the major axis with triangles and squares, respectively (see Eq. 3.2 and Eq. 3.4). Thin solid curves are the circular velocity curves  $v_{c,ADC}$  from applying asymmetric drift corrections (Sect. 2.5.3), where the bars indicate their uncertainty. Thick solid curves are circular velocity curves  $v_{c,JAM}$  from the best fits ( $\chi^2$ -minimum) of axisymmetric Jeans solutions based on MGE models (Sect. 2.5). Their variation due to different assumed velocity anisotropies ( $-0.6 < \beta_z < +0.6$ ) within  $\Delta\chi^2 = 3\sigma$  confidence level, are given by the grey curves. There is a significant mismatch between the two models although taking into account their uncertainties, and  $v_{c,ADC}$  is always underestimated with respect to  $v_{c,JAM}$  (except for galaxy NGC 0036).

### 3.5 COMPARING CIRCULAR VELOCITY CURVES

Having constructed axisymmetric Jeans models (JAM) that fit the combined observed stellar mean velocity and velocity dispersion fields, we use equation (2.4) to obtain the circular velocity curve per galaxy. The resulting  $v_{c,\text{JAM}}$  curves from the best-fit JAM model are plotted as thick solid curves in Fig. 3.11 and Fig. 3.12, while the underlying grey curves indicate the spread due to varying the velocity anisotropy parameter  $\beta_z$  within  $3\sigma$  from the best-fit value. On the other hand, combining the measured stellar deprojected velocity profile  $\overline{v_\phi}$  (grey triangles) and radial dispersion profile  $\sigma_R$  (grey squares) the asymmetric drift correction (ADC) formula in equation (2.6) yields the circular velocity curves  $v_{c,\text{ADC}}$  indicated by the thin solid curves with propagated error bars.

Only for the galaxy NGC 3346 (Scd), the ADC and JAM modelling approaches yields circular velocity curves that are consistent with each other over the full radial range covered by the stellar kinematics. For all other galaxies, the ADC approach underestimates the circular velocity curve obtained from JAM models for at least part of the radial range. There is only one case, in the outer parts of galaxy NGC 0036, where  $v_{c,\text{ADC}}$  curve goes higher than  $v_{c,\text{JAM}}$ . This might be explained by non-suitable fitting functions during derivation of  $v_{c,\text{ADC}}$  or non-constant mass-to-light ratio in the assumptions of  $v_{c,\text{JAM}}$ . To quantify these differences, we plot in Fig. 3.13 and Fig. 3.14 the ratio between the enclosed mass profiles inferred from both modelling approaches via their respectively circular velocity profiles, i.e.,  $M_{\text{JAM}}/M_{\text{ADC}} = v_{c,\text{JAM}}^2/v_{c,\text{ADC}}^2$ , where  $M(< R) = v_c^2 R/G$ . Overall, the mass ratio for SAURON Sb–Sbc galaxies is larger in the inner parts ( $R < R_e/5$ ) and decreases in the outer parts ( $> R_e/5$ ), while for Scd–Sd galaxies the mass ratio is rather constant or even increases in the outer parts. Similar for the 8 E–Sbc CALIFA galaxies, where the mass ratio is larger in the inner parts ( $R < R_e/2$ ) and decreases in the outer parts ( $> R_e/2$ ).

At  $R_e/5$ , the mass ratio varies from 1 to 10 with an average of around 3-4, i.e., adopting the simpler ADC approach underestimates the total mass in the inner parts of our 26 E–Sd galaxies by a factor  $\sim 3-4$  compared to that inferred from the JAM models.

### 3.6 DISCUSSION

The significant differences we found between the circular velocity curves from the two modelling approaches have a strong impact on the inferred total mass distribution and thus also on any follow-up inference like the amount of dark matter in the inner parts of these 26 E–Sd galaxies. Henceforth, in what follows we discuss the different assumptions adopted in both the axisymmetric Jeans models (JAM) and the asymmetric drift correction (ADC), and argue that the

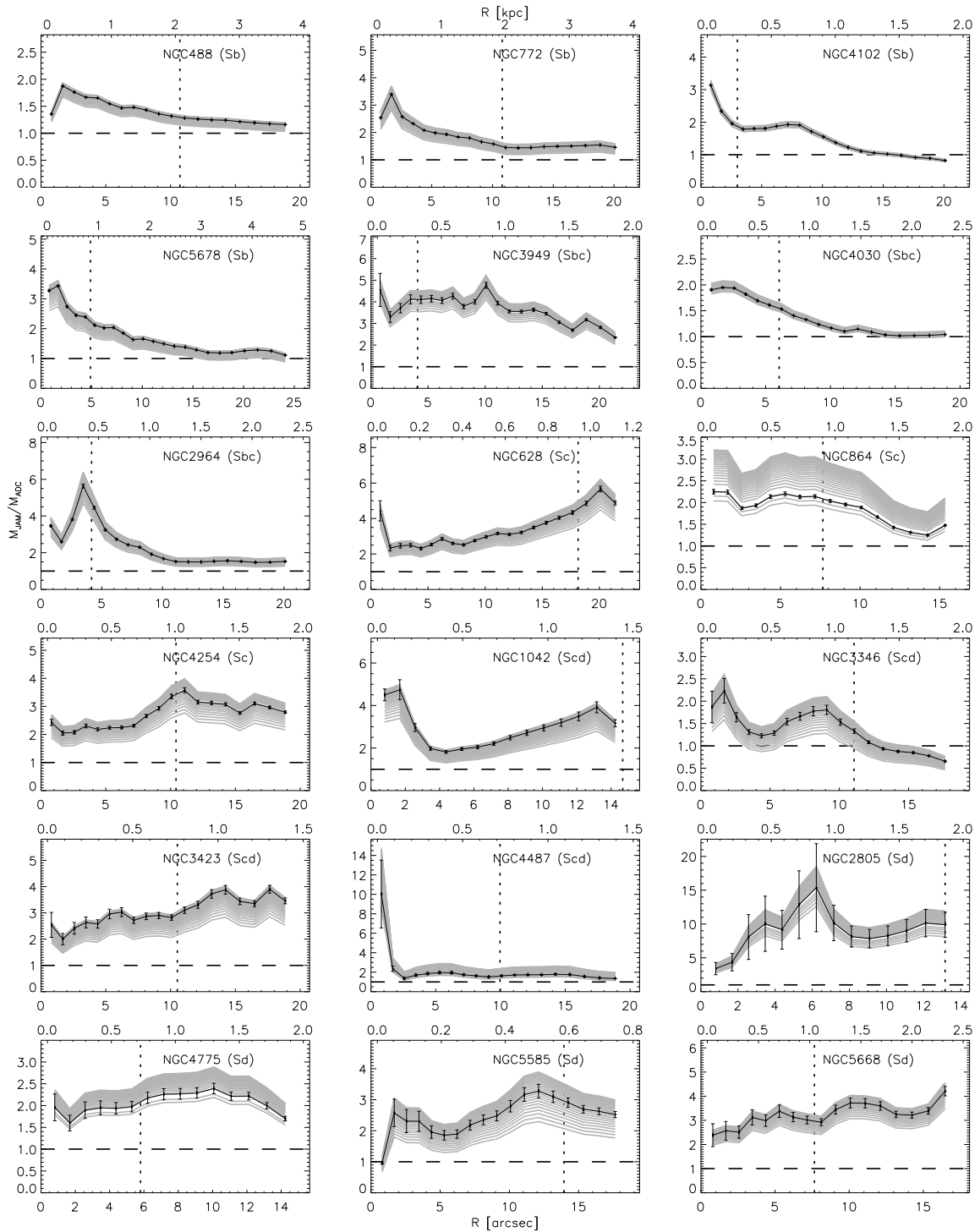


**Figure 3.13:** SAURON mass ratio between the circular velocity profiles of  $M_{\text{JAM}}$  best fit ( $\chi^2$ -minimum) and  $M_{\text{ADC}}$ , where the bar indicates its uncertainty. The shaded areas show the spread in the ratio profiles of  $M_{\text{JAM}}$  when varying the velocity anisotropy ( $-0.6 < \beta_z < +0.6$ ) within  $\Delta\chi^2 = 3\sigma$  confidence level. Over-plotted are the limit of the one-fifth of the galaxy MGE effective radius  $R_e/5$  (dotted line) and the one-to-one relation of the mass ratio (dashed line). The significant mismatch of the two models comes from the bulge in the very central parts of Sb-Sbc ( $< R_e/5$ ) and possibly a thick disc in the outer parts of Sc-Sd galaxies ( $> R_e/5$ ).

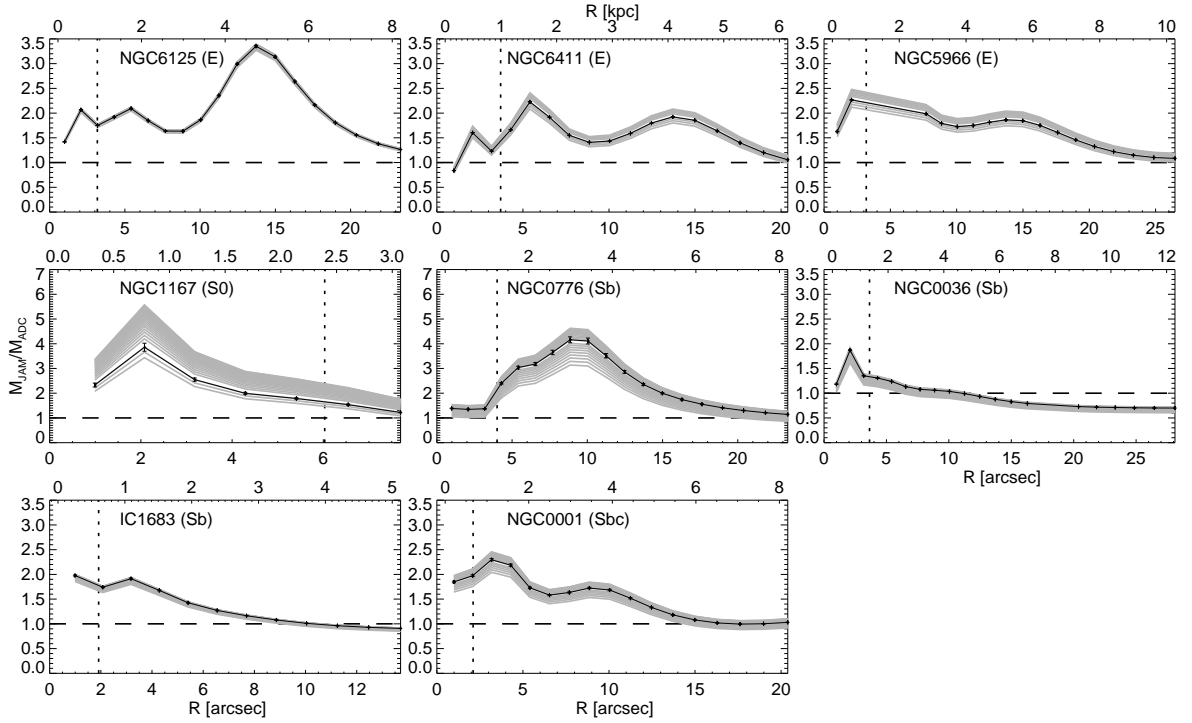


**Figure 3.14:** CALIFA mass ratio between the circular velocity profiles of  $M_{\text{JAM}}$  best fit ( $\chi^2$ -minimum) and  $M_{\text{ADC}}$ , where the bar indicates its uncertainty. The shaded areas show the spread in the ratio profiles of  $M_{\text{JAM}}$  when varying the velocity anisotropy ( $-0.6 < \beta_z < +0.6$ ) within  $\Delta\chi^2 = 3\sigma$  confidence level. Over-plotted are the limit of the one-fifth of the galaxy MGE effective radius  $R_e/5$  (dotted line) and the one-to-one relation of the mass ratio (dashed line). The significant mismatch of the two models comes from the bulge in the very central parts of S0-Sbc ( $< R_e/2$ ), possibly a thick disc in the outer parts of Sc-Sd galaxies ( $> R_e/2$ ) and from the spheroidal shape of the elliptical galaxies.

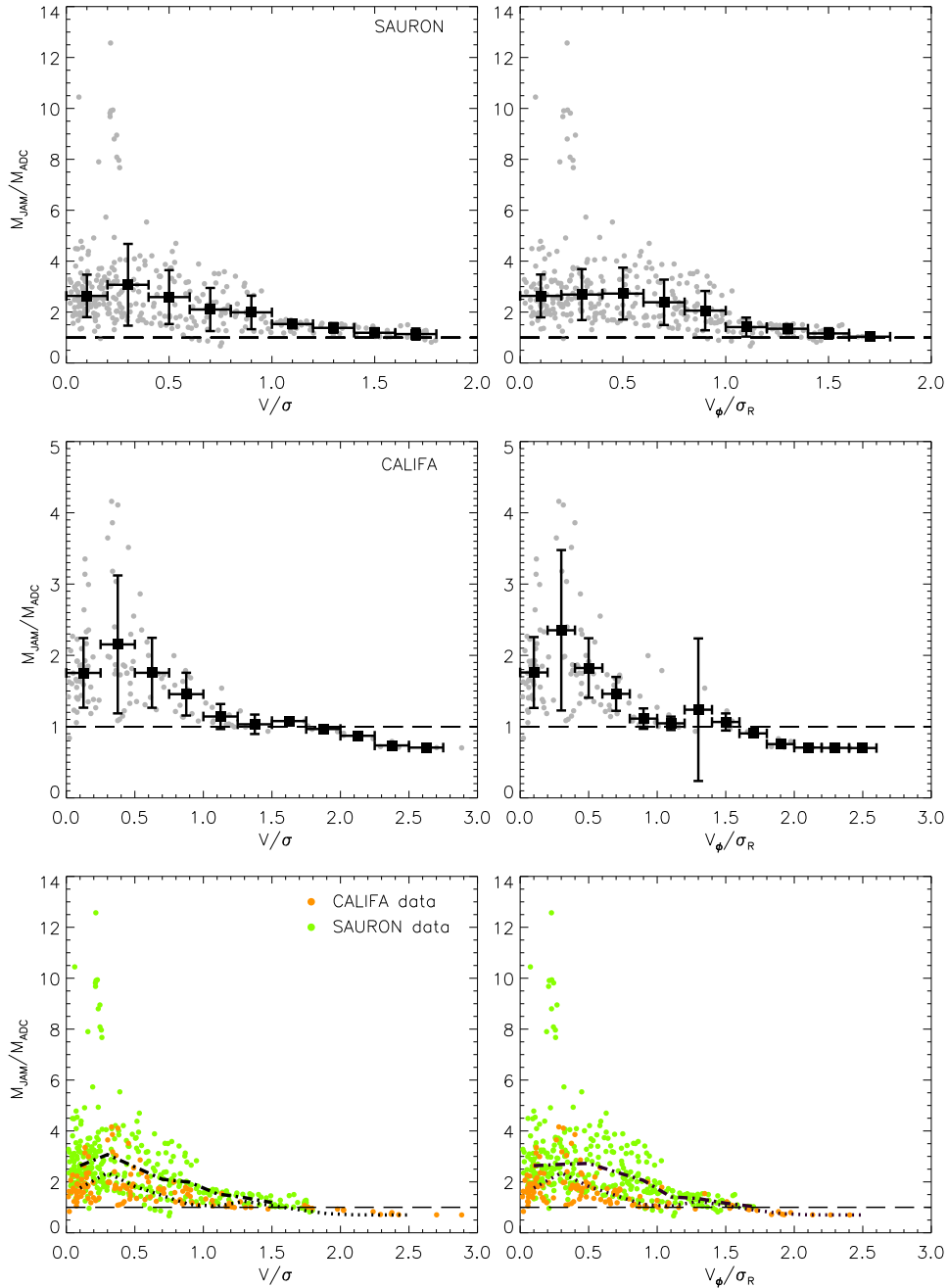


**Figure 3.15:** Mass ratios  $M_{\text{JAM}}/M_{\text{ADC}}$  as measured at different radii versus the ordered-over-random motion at the same radii. Top and middle panels correspond to SAURON and CALIFA galaxies, respectively, while the bottom panels display the comparison between the two samples. Both  $V/\sigma$  (left panels) are directly plotted from the line-of-sight stellar mean velocity and velocity dispersion profiles as well as  $\overline{v}_\phi/\sigma_R$  (right panels) from the deprojected rotation and radial velocity dispersion profiles. The black filled squares with error bars show the biweight mean and standard deviation of the mass ratio per bin with size of 0.2 in  $V/\sigma$ . Bottom panels show a slight difference between the mean values of the samples – SAURON (dash-dotted curve) and CALIFA (dotted curve), which might be explained with their different spatial resolutions. The discrepancy between the ADC and JAM inferred enclosed masses becomes gradually larger for decreasing  $V/\sigma \lesssim 1.5$ , consistent with the spheroidal shapes of the elliptical galaxies, a presence of dynamically hot bulge in the inner parts of spiral galaxies and/or a dynamically hot(ter) and thick(er) disc in late-type galaxies invalidating the thin-disc approximation.

oblate/spherical shape of elliptical galaxies or presence of bulges and possibly also thick discs in the spiral galaxies invalidate the ADC thin-disc assumption and require a full line-of-sight integration as in the JAM modelling approach.

### 3.6.1 ASSUMPTIONS IN THE MASS MODELS

*Mass-follows-light (JAM):* Within the small radial range covered by the stellar kinematics, typically well within a third of  $R_e$ , we expect to be insensitive to variations in mass-to-light due to a dark matter halo. Indeed, when we allow the mass-to-light ratio of the different Gaussian components to vary, the fit does not significantly improve and since the parameters are naturally less well constrained we adopt the mass-follows-light assumption here. Also, Bottema (1993) modelled the stellar kinematics of 12 unbarred high-surface-brightness spirals of type Sa to Sc, and found that the assumption of an approximately constant mass-to-light ratio within the galaxies is consistent with the observations. Sophisticated spherical dynamical models of Rix et al. (1997) and Gerhard et al. (1998) show that the mass-to-light ratio in elliptical galaxies rises outwards beyond about an effective radius  $R_e$  (for comparison, the CALIFA elliptical galaxies extend to  $1 - 1.6 R_e$ ).

*Constant anisotropy in the meridional plane (JAM):* Whereas the velocity anisotropy  $\sigma_\phi/\sigma_R$  in the equatorial plane is inherent in the solution of the axisymmetric Jeans equations (Section 2.5.1), the velocity anisotropy  $\sigma_z/\sigma_R$  in the meridional plane is a free parameter, re-casted as  $\beta_z = 1 - \sigma_z^2/\sigma_R^2$ . We can in principle allow for a radially varying anisotropy by having different  $\beta_z$  values for the Gaussian components, but like for the mass-to-light ratio the fits do not significantly improve over the small radial range covered by the stellar kinematics. This is not unexpected, as Bottema (1993) already argued that for spirals the  $\sigma_z/\sigma_R$  is constant at approximately 0.6, close to the measured value of  $0.53 \pm 0.07$  in the solar neighbourhood (Dehnen & Binney 1998; Mignard 2000). This ratio of the anisotropy is measured also in a few spirals of type Sa to Sbc (Gerssen et al. 1997, 2000; Shapiro et al. 2003), yielding slightly larger constant values between 0.6 and 0.8. Based on long-slit spectra for a sample of 17 edge-on Sb–Scd spirals, Kregel & van der Kruit (2005) also infer constant values, although slightly lower again between 0.5 and 0.7. Gerhard et al. (2001) show that the anisotropy of 21 luminous elliptical galaxies has constant values 0.2 – 0.4 beyond  $0.2 R_e$ .

*Shape of the velocity ellipsoid (JAM, ADC):* The JAM model assumes that the velocity ellipsoid in the meridional plane is aligned with the cylindrical coordinate system so that  $\overline{v_R v_z} = 0$ , whereas in the ADC approach we allow for a tilt of the velocity ellipsoid through the parameter  $\kappa$ . In the Appendix 5.1, we show that the resulting circular velocity curve is only weakly dependent on this tilt and hence we adopt a value  $\kappa = 0.5$ , intermediate between aligned with the cylindrical

( $\kappa = 0$ ) and spherical ( $\kappa = 1$ ) coordinate system. The weak dependence is not unexpected because especially for late-type spiral galaxies most of the stellar mass is concentrated toward the equatorial plane where by the assumption of axisymmetry  $\overline{v_R v_z} = 0$ .

*Dust (JAM, ADC):* The surface brightness distribution of the SAURON and CALIFA galaxies that is used in both JAM and ADC modelling approaches can be strongly affected by extinction due to dust. We have tried to minimise the effects of dust in various ways<sup>3</sup>: (i) selecting galaxies that are away from edge-on where dust extinction is strongest (and away from face-on where the stellar velocity dispersion would be too far below the spectral resolution), (ii) inferring the surface brightness distribution from images in the near-infrared where the extinction is typically orders of magnitude lower than in the optical, (iii) fitting smooth analytical and subsequent MGE profiles to the radial surface brightness profile after azimuthally averaging over annuli to suppress deviations caused by bars, spiral arms as well as regions obscured by dust.

The stellar kinematics are obtained from integral-field spectroscopy in the optical and thus could also be affected if the (giant) stars that contribute along the line-of-sight with different motions are affected by the dust in different ways. For example, if dynamically colder stars closer to the disc plane are relatively more obscured than dynamically hotter stars above the disc plane, the resulting combined ordered-over-random motion could be biased to lower values. However, Baes et al. (2003) show that already a few degrees away from edge-on the effects of dust are strongly reduced. Henceforth, the effects of dust through photometry and kinematics on the inferred circular velocity curves from both modelling approaches are expected to be minimal.

*Thin-disc (ADC):* Circular velocity curves of spirals nearly always come from (cold) gas, which is naturally in a thin disc, but even stellar discs of these late-type spiral galaxies are believed to be thin, with inferred intrinsic flattening  $q \sim 0.14$  (e.g., Kregel et al. 2002). Even the bulges in late-type spiral galaxies are very different from the 'classical' bulges in lenticular galaxies; Sérsic profile fits to their surface brightness, i.e.,  $I(R) \propto \exp(-R^{1/n})$ , show that towards later-types, the bulges are smaller in size, have profiles closer to exponential ( $n = 1$ ) than de Vaucouleur ( $n = 4$ ), and are flatter (e.g., Ganda et al. 2009). Henceforth, the thin-disc assumption adopted in the ADC approaches to spiral galaxies thus also seems to be reasonable. However, in case of bright elliptical galaxies we might expect an invalidation of the thin disk assumption. The reason is because they are dynamically hot, pressure-supported systems and well represented by a spherical, oblate or triaxial basic state (Longair 1998).

---

<sup>3</sup>For SAURON galaxies, steps (i) and (ii) are done by Ganda et al. (2009).

### 3.6.2 BULGES, THICK DISCS AND SPHEROIDS

Although all assumptions above appear reasonable in case of our sample of 26 (E–Sd) galaxies, we suppose that the thin-disc approximation adopted in the ADC modelling approach has the strongest impact on the mismatch with respect to the JAM modelling approach. As can be seen from Fig. 3.11 and Fig. 3.12, the stellar rotation (grey triangles) is of the same order and often even lower than the stellar dispersion (grey squares). The resulting low ordered-over-random motion values implies that the stars are far from dynamically cold as expected for a thin disc.

Since we are probing the inner parts of these galaxies it might well be the presence of spheroids, bulges and/or thick stellar disc that cause a break-down of the thin-disc approximation. For the Sb–Sbc galaxies, the discrepancy in the inferred enclosed mass ratio from the JAM and ADC modelling approaches indeed seems to be larger in the inner parts where the luminosity is dominated by the presence of the bulge. For the Sd galaxies in particular, the presence of a thick(er) disc component in these inner parts may explain the approximately constant discrepancy. For early-type galaxies (E/S0) the discrepancy extends to larger radii ( $\sim 1 R_e$ ) most likely due to their spheroidal shapes.

Independent of the nature of the dynamically hot stellar (sub)system, it seems that the local value of the ordered-over-random motion is an indicator for the validity of the thin-disc approximation. Henceforth, we plot in Fig. 3.15 for all galaxies together (SAURON and CALIFA samples separate due to their difference in spatial resolution) the mass ratios  $M_{\text{JAM}}/M_{\text{ADC}}$  as measured at different radii (from Fig. 3.13 and Fig. 3.14) versus the ordered-over-random motion at the same radii, both  $V/\sigma$  (left panels) directly from the observed stellar mean velocity and velocity dispersion profiles as well as  $\overline{v_\phi}/\sigma_R$  (right panels) from the deprojected rotation and radial velocity dispersion profiles (from Figures 3.7, 3.8, 3.9 and 3.10). The black filled squares with error bars show the (biweight) mean and standard deviation of the mass ratio per bin with size of 0.2 in  $V/\sigma$ .

SAURON : In Fig. 3.15 (top panels), we see that the enclosed mass values of both modelling approaches are consistent for  $V/\sigma \gtrsim 1.5$ , corresponding to those radii in the Sb–Sbc galaxies where the disc luminosity is dominating over the bulge luminosity. The inverse is not true, i.e., in many cases where the exponential disc is dominating in light the mass ratio is not approaching unity. Henceforth, the exponential disc not only needs to be dominating in light but also dynamically cold for the thin-disc approximation to hold and the ADC approach to work. The discrepancy between the ADC and JAM inferred enclosed masses becomes gradually larger for decreasing  $V/\sigma \lesssim 1.5$ , consistent with the presence of a dynamically hot bulge in the inner parts and/or a dynamically hot(ter) and thick(er) disc in particularly the latest-type spiral galaxies invalidating the thin-disc approximation.

CALIFA : In Fig. 3.15 (middle panels), we show that the enclosed mass values of ADC and

JAM modelling approaches are consistent in the range  $1.5 \lesssim V/\sigma \lesssim 2.0$  ( $1.5 \lesssim v_\phi/\sigma_R \lesssim 1.8$ ). However, JAM underestimates the galaxies' masses at  $V/\sigma \gtrsim 2.0$  ( $v_\phi/\sigma_R \gtrsim 1.8$ ) and possible explanation is that the mass-to-light ratios and velocity anisotropies are not constant. Projection effects may play a role too (e.g., spheroidal shapes of the elliptical galaxies or uncertainties in their inclination).

Detailed photometric studies indicate that most disc galaxies contain a thick disc (e.g. [Dalcanton & Bernstein 2002](#); [Seth et al. 2005](#); [Comerón et al. 2011](#)), and in low-mass galaxies with circular velocities  $<120 \text{ km s}^{-1}$ , like our Scd–Sd galaxies, thick disc stars can contribute nearly half the luminosity and dominate the stellar mass. Moreover, recent hydrodynamical simulations that reproduce thick discs show that their typical scale lengths are around 3–5 kpc (e.g. [Doménech-Moral et al. 2012](#)), i.e., twice the typical range covered by our stellar kinematics.

Fig. 3.15 shows that the mean discrepancy in the two mass measurements is smoothly increasing with decreasing  $V/\sigma$ , but the deviation in the discrepancy is large at a given  $V/\sigma$ . Although the deviation is somewhat reduced when using intrinsic  $\overline{v_\phi}/\sigma_R$  values, it is not possible to use the locally measured ordered-over-random motion to estimate the amount at which the ADC underestimates the enclosed mass. This means that if locally  $V/\sigma \lesssim 1.5$ , it is necessary to take into account that the stars are not in a thin disc and do a full line-of-sight integration as in the Jeans models.

### 3.7 CONCLUSIONS

The rotation curves of galaxies, traced by atomic, ionised or molecular gas, provide the most direct path to estimating total galaxy masses. However, gas settles in the equatorial or polar plane and hence is insensitive to the mass distribution perpendicular to it. Also, gas is dissipative and easily disturbed by perturbations in the plane from e.g. a bar or spiral arms or completely absent in ellipticals. Thus stars appear to be a better tracer as they are distributed in all three dimensions and, being collision-less, they are much less sensitive to perturbations. However, stars are not cold tracers as they move in orbits that are neither circular nor confined to a single plane. This fact implies the need of knowing their velocity dispersions, in addition to their velocities, to recover the total mass distribution.

In this paper we compare two different approaches of inferring dynamical masses of 26 E–Sd SAURON and CALIFA galaxies: the commonly used asymmetric drift correction (ADC) and axisymmetric Jeans equations. We used the stellar kinematics derived by integral field spectroscopy, observed with the SAURON and PMAS/PPAK spectrographs. We obtained stellar mean velocity and velocity dispersion maps and derived the galaxies' circular velocity curves by fitting

solutions to the Jeans equations. Using the same data we also derived the circular velocity curves via the ADC technique.

We found that for only one galaxy in our sample (NGC 3346) ADC and Jeans approaches lead to consistent results. For the remaining galaxies, the ADC approach underestimates the circular velocity curves, as compared to the ones derived with the Jeans model. The mass ratio  $M_{\text{JAM}}/M_{\text{ADC}} = v_{c,\text{JAM}}^2/v_{c,\text{ADC}}^2$  for E–Sbc galaxies is larger in the inner parts ( $R < R_e/5$  for SAURON and  $R < R_e/2$  for CALIFA sample) and decreases outwards. However, for Scd–Sd galaxies the mass ratio stays constant and in a few cases increases towards larger radii. There is an only one exception – galaxy NGC 3346, where  $M_{\text{JAM}}/M_{\text{ADC}} < 1$ . It might be explained by non-constant mass-to-light ratios and/or velocity anisotropies. Projection effects may play a role too (e.g., a spheroidal shape, uncertainties in the inclination).

We explain the discrepancy between the two dynamical model approaches ADC and JAM with the spheroidal shape of the elliptical galaxies, presence of bulge and/or thick discs in spiral galaxies.

Whereas various earlier studies have qualitatively indicated that the ADC approach might not be suitable in case of stellar systems that are (locally) not dynamically cold (e.g., Neistein et al. 1999; Bedregal et al. 2006; Williams et al. 2010), our results provide a quantitative statement: when  $V/\sigma \lesssim 1.5$  the ADC approach can significantly underestimate the circular velocity curve and hence enclosed mass.



## MASS DISTRIBUTIONS OF GALAXIES ACROSS HUBBLE SEQUENCE: THE LINK BETWEEN GALACTIC KINEMATICS AND DARK MATTER CONTENT

### ABSTRACT

We infer stellar, gas and dynamical inner mass distributions of 26 E–Sd SAURON and CALIFA galaxies. The dynamical profiles are obtained via a full line-of-sight integration as provided by solutions of the axisymmetric Jeans equations. Further, we derive the stellar profiles using mass-to-light ratios from a stellar population analysis, while the gas mass is modeled adopting a universal exponential profile. As expected, the gas contribution is negligible to the total baryonic mass of the galaxies. The dynamical masses of almost all galaxies, instead, are much larger than their baryonic masses. Elliptical (E) and late-type (Sd) galaxies have particularly high dark matter fractions in contrast to the rest of the Hubble type galaxies. We investigate the maximum circular velocities and qualitative shape of rotation curves across galaxy morphology. Peaked rotation curves are found in high-mass early-type galaxies, while slowly rising rotation curves are typical for low-mass late-type spirals. The rotation curves of the studied galaxies show a smooth transition through the Hubble sequence, increasing their maximum velocities from Sd to E types. We find a correlation between the inner dynamical masses and total stellar masses, where  $M(< R_e/5) \approx 0.02M_\star^{\text{tot}}$ . Dark matter fractions of the galaxies appear anti-correlated with their ordered-over-random motion ratios.

## 4.1 INTRODUCTION

Rotational curves (hereafter: RCs) are generally considered one of the best tools to trace the mass distribution of galaxies. Since the earlier studies (Rubin et al. 1980; Bosma 1981b; Persic & Salucci 1988) it appeared evident from the non-Keplerian shape of the curves that the mass derived with this technique was much higher than the total luminous mass (accounting stars and gas). This suggested that a conspicuous fraction of the galactic matter is constituted by a invisible component called Dark Matter (hereafter: DM), that appears to increase toward the outskirts of the galaxies (Persic & Salucci 1988; Broeils 1992).

Moreover, the shape and the amplitude of rotation curves are closely related to the gravitational potential of the galaxy, and they, therefore, can be used to obtain important information about the different components of the galaxies (see Chapter 1).

In almost all disc galaxies, the stellar disc contribution can be scaled to explain all features of the observed rotation curves out to about two or three disc scale lengths (e.g., Kalnajs 1983; Palunas & Williams 2000). This indicates that the total mass density and luminous mass density are closely connected (e.g., Sancisi 2004; Swaters et al. 2009). In the maximum disc hypothesis, the contribution of the stellar disc to the rotation curve is maximized, and thus the dark matter is minimized (e.g., van Albada et al. 1985; Begeman 1987; Broeils 1992). The disk is sub-maximal when the dark halo is dynamically important in the central parts of the galaxy. The ‘maximality’ of a galaxy is often presented on the basis of the stellar-disk mass fraction,  $f_{\text{disk},\star} = V_{\text{disk},\star}/V_c$ , traditionally measured at  $2.2 h_R$ , and includes the total mass associated with the stellar disk. The most commonly adopted definition of a maximum disk was provided by Sackett (1997), who proposed  $f_{\text{disk},\star}^{2.2h_R} = 0.85 \pm 0.10$  to be an appropriate definition for maximum disks in galaxies of Hubble type similar to the Milky Way (Sb and Sc).

In a study of 30 spiral galaxies as part of DiskMas survey, Martinsson et al. (2013) find that galaxies with high bulge-to-disk ratio ( $B/D > 0.1$ ) have steep rises in their rotation curves, indicating a high central concentration of mass, and tend to have high  $\sigma_z/V_{\text{max}}$  ratio, where  $\sigma_z$  indicates the vertical velocity dispersion and  $V_{\text{max}} = 0.85V_c$ .

This correlation between the light distribution and the inner rise of the rotation curve is well known for spiral galaxies (e.g., Kent 1987; Corradi & Capaccioli 1990). Swaters et al. (2009) have found that dwarf galaxies with a central concentration of light also have rotation curves that rise more steeply in the center than the rotation curves of dwarf galaxies that do not have a central concentration of light. They observed a correlation between the light distribution and the inner rotation curve shape, as seen in both spiral and late-type dwarf galaxies, implying that galaxies with stronger central concentrations of light also have higher central mass densities, and it suggests that the luminous mass dominates the gravitational potential in the central regions,

even in low surface brightness dwarf galaxies.

Avila-Reese et al. (2002) discuss the shapes and decomposition of rotation curves of galaxies formed within growing cold dark matter halos. They find that RC shape correlates mainly with the surface brightness (SB), the luminous mass fraction and the bulge fraction of the galaxies. Further, the higher the galaxy's disk SB is, the steeper the decline shape (presence of high peak) in the RC and the larger the bulge-to-disk ratio. Their high SB models can be maximum disks only when the halos have a shallow core. The low SB models possess sub-maximum disks.

Modern large-scale dark matter simulations predict the properties of dark matter haloes at all cosmic epochs in cold dark matter (CDM) cosmologies (Springel et al. 2005; Boylan-Kolchin et al. 2008; Klypin et al. 2011). Galaxies form by cooling and condensation of gas in the centers of the potential wells of extended virialized dark matter halos (White & Rees 1978; Fall & Efstathiou 1980b; Blumenthal et al. 1984). The galaxy properties such as luminosity and stellar mass depend on the halo potential and thus on the halo mass.

The work by Kannan et al. (2014) indicates that the effect of local photoionizing sources in the galaxies is significant for shaping the rotation curves. A simulation of a Milky Way-like galaxy using a local photoionization model shows the star formation decreases by increasing the cooling time of the gas in the halo and increasing the equilibrium temperature of dense gas in the disc. Coupling the local radiation field to gas cooling from the halo provides a preventive feedback mechanism which keeps the central disc light and produces slowly rising rotation curves without resorting to extreme feedback mechanisms.

Many statistical models are employed to derive the constraints on the relation between galaxy properties and halo mass at a given epoch (White et al. 2007; Conroy et al. 2007; Conroy & Wechsler 2009). The recent work by Moster et al. (2013) used N-body simulations to obtain the halo abundances and assembly histories of galaxies. They identify the progenitors of a given halo at an early epoch and derive the amount of stellar mass accreted onto the central galaxy. Accounting for stellar mass loss, they compute the stellar mass formed through star formation and convert this into a star formation rate (SFR). Then it is straightforward to derive the star formation history (SFH) of the galaxy at the centre of the halo. They present convenient fitting functions for stellar masses, star formation rates, and accretion rates as functions of halo mass and redshift. They show that the stellar-to-halo mass relation increases with increasing halo mass, reaches a maximum around  $\text{Log}(M_{\text{halo}}/M_{\odot}) = 12$  and then decreases again.

From observation of 50 dispersion-supported and 61 rotation-supported galaxies, Kuzio de Naray & McGaugh (2014) probe the dark matter halo in the inner parts of early- and late-type galaxies, deriving dynamical masses enclosed at 500 pc. They find that this dynamical quantity increases only slowly with stellar mass ( $M_{\text{dyn}} (< 500 \text{ pc}) \propto M_{\star}^{0.16}$ ) over  $\sim 9$  decades in baryonic mass and  $\sim 3$  in length scale, with a sudden upturn at the highest masses ( $M_{\star} \gtrsim 10^{10} M_{\odot}$ ). This upturn occurs

for the earliest types (S0 and Sa) of disk galaxies, and is consistent with the additional mass within 500 pc being predominantly stellar. This sudden change may be indicative of different bulge formation mechanisms between early- and late-type disks.

To investigate the connection between kinematics of the galaxies and their dark matter content, in Section 4.2 we derive the dynamical, stellar, gas and dark matter distributions of 26 E–Sd systems. Further, in Section 4.3 we study the inner dynamical masses (at  $R_e/5$  and 500 pc) in order to obtain scaling relations with inner and total baryonic masses that will allow us to predict total dark matter contents of the galaxies. In Section 4.4 we study how the maximality and sub-maximality of the galaxies’ disks are related to their sizes. In Section 4.5 we link the shape of the rotation curves of the galaxies and their dark matter fractions. Possible global dynamical classification of galaxies is discussed in Section 4.6, and we draw our conclusions in Section 4.7.

## 4.2 MASS DISTRIBUTIONS OF GALAXIES ACROSS HUBBLE SEQUENCE

In order to study the dark matter content of the 26 SAURON and CALIFA galaxies across the Hubble sequence, we first need to infer their stellar, gas and dynamical mass profiles. This is accomplished in three different ways.

### 4.2.1 DYNAMICAL MASS

In Chapter 3, we show that a full line-of-sight integration is needed to reliably extract the rotation curves (RC) of the 26 E–Sd galaxies. First, we solve the Jeans equations in the axisymmetric case for a given mass distribution, which we infer from deprojecting the observed surface brightness and multiplying with a constant mass-to-light ratio, i.e.,  $\Upsilon_{dyn}$  (Cappellari 2008). Then we compare the resulting predictions of the second velocity moment  $V_{RMS} = \sqrt{V^2 + \sigma^2}$  to the combined maps of the observed mean velocity  $V$  and velocity dispersion  $\sigma$ . This provides the best-fit model mass distribution, which through Poisson’s equation is related to the gravitational potential; the circular velocity follows as  $V_{circ}^2 = R \frac{\partial \Phi}{\partial R} |_{z=0}$ . Here, we infer the enclosed mass profiles via galaxies’ circular velocity profiles as  $M_{dyn}(< R) = v_{c,JAM}^2 R/G$ , where the  $R$  is radius of the galaxy and the  $G$  is the gravitational constant. In Fig.4.1 and Fig.4.2, we present the inferred dynamical mass profiles with thick black solid curves and variation ranges given by grey bands. The masses of the 26 SAURON and CALIFA galaxies range between  $10^{11} M_\odot$  for E,  $10^{10} - 10^{11}$  for S0–Sc and  $10^9 M_\odot$  for Scd–Sd. Therefore, E–Sc and Scd–Sd types are the higher- and lower-mass galaxies in our sample, respectively.

## 4.2.2 STELLAR MASS DISTRIBUTION

Having obtained the dynamical mass profiles, in order to derive the total baryonic mass we need to estimate the contribution of the stellar and gas mass. Thus, we infer the stellar circular velocity curves from multi-Gaussian Expansion method (see Eq. 2.4) through deprojecting the observed surface brightness and multiplying with a constant mass-to-light ratio ( $\Upsilon_*$ ) derived from stellar population analysis of Ganda et al. (2007) for the SAURON sample and Cid Fernandes et al. (2013) for the CALIFA sample.

Stellar population synthesis is a powerful technique to study star formation histories and the evolution of galaxies that are too distant to be resolved into individual stars. The measurement of absorption line strengths combined with stellar population models has been used to investigate the luminosity-weighted age, metallicity and abundance ratios in integrated stellar populations (Ganda et al. 2007). The stellar mass-to-light ratio  $\Upsilon_*$  is usually estimated by comparing observed stellar population characteristics with predictions from models. In the following we describe the different techniques used to derive the stellar populations of SAURON and CALIFA galaxies.

### SAURON

Given a set of stellar population models, Ganda et al. (2007) select the best-fitting one by simultaneously minimizing the distance between the three model Lick indices  $H\beta$ , Fe5015 and  $Mgb$  and the observed ones, calibrated to the Lick system. Doing this for each spectrum in the SAURON datacube (binned to a minimum signal-to-noise ratio of 60, see Ganda et al. 2006, 2007), they obtain for each corresponding position on the sky the best-fitting stellar population parameters, including  $M_*/L$ . From these maps of stellar  $\Upsilon_*$  using the KINEMETRY algorithm they extract the radial profiles to compare with the dynamical  $\Upsilon_{\text{dyn}}$ . Throughout the analysis a Chabrier IMF is adopted.

### CALIFA

A full spectral fitting analysis is performed comparing combinations of single stellar populations (SSP) spectra with those of our sample galaxies using the Starlight code. The fitting results are processed with the CALIFA pipeline PYCASSO resolving the flux of the galaxies in time and space. Here, the time information is collapsed to produce 2D maps of the stellar mass surface density and light weighted ages, azimuthally averaged to produce radial profiles. Throughout it is adopted a Chabrier IMF.

In Fig.4.1 and Fig.4.2 we present the inferred stellar mass profiles with thick red curves for variation ranges given by the dashed red curves. The stellar masses  $M_*$  ranges between  $10^9 - 10^{10} M_\odot$  for E–Sc to  $10^8 - 10^9 M_\odot$  for Scd–Sd. For almost all galaxies  $M_* < M_{\text{dyn}}$ .

### 4.2.3 GAS MASS MODEL

We complete the estimation of the galaxies' baryonic masses by inferring their total gas content. For 23 disk galaxies from the sample we adopt a universal exponential gas profile described in Bigiel & Blitz (2012), and for the remaining 3 elliptical galaxies a gas ratio from Longair (1998) and Young (2002) is adopted.

Bigiel & Blitz (2012) show that disk galaxies exhibit a tight exponential radial profile of their total gas content, in the case in which the radius is scaled to the optical radius and the surface density of the gas is scaled to the surface density of the gas at the transition radius (radius corresponding to a conversion from HI to H<sub>2</sub>). The scaling relation for disk galaxies then follows as

$$\frac{\Sigma_{\text{gas}}}{\Sigma_{\text{trans}}} = 2.1 \times e^{-1.65 \times \frac{r}{r_{25}}}, \quad (4.1)$$

where  $r_{25}$  is the optical radius of the galaxy defined as the 25 mag arcsec<sup>2</sup> B-band isophote (Schruba et al. 2011).  $\Sigma_{\text{gas}} = \Sigma_{\text{HI}} + \Sigma_{\text{H}_2}$  is the total gas surface density equal to the sum of the atomic hydrogen surface density  $\Sigma_{\text{HI}}$  and the molecular hydrogen surface density  $\Sigma_{\text{H}_2}$  (as traced by <sup>12</sup>CO(J=2-1) emission).  $\Sigma_{\text{trans}}$  is the surface density of the gas at the transition radius. Thus, we can calculate the total gas mass within radius R as

$$M_{\text{gas}}(< R) = 2\pi \int_0^R \Sigma_{\text{gas}} r dr = 2\pi \Sigma_{\text{trans}} \int_0^R 2.1 \times e^{-1.65 \times \frac{r}{r_{25}}} r dr, \quad (4.2)$$

where the mass of the gas  $M_{\text{gas}}$  depends only on the optical radius  $r_{25}$ , i.e. on the size of the stellar disk.  $\Sigma_{\text{trans}}$  has a typical value of about  $14 M_\odot \text{pc}^{-2}$  and does not vary significantly from galaxy to galaxy (e.g., Leroy et al. 2008; Bigiel et al. 2008).

We adopt values for the optical radii  $r_{25}$  of our 23 disk galaxies from RC3<sup>1</sup> (Third Reference Catalog of Bright Galaxies, see Table 4.1). Bigiel & Blitz (2012) show that Eq. (4.2) allows us to predict the total gas mass of a disk galaxy within a factor of two uncertainty, i.e., 50%. Although taking into account this high uncertainty, the contribution of the gas to the stellar and dynamical mass is negligible, between 1% and 10% for early- and late-type spiral galaxies, respectively (i.e., S0–Sd).

<sup>1</sup><http://heasarc.nasa.gov/W3Browse/all/rc3.html>

Ellipticals are not disc galaxies. Therefore we can not adopt the same universal exponential profile and model their gas distribution in that manner. We use instead the value of the neutral hydrogen mass from Longair (1998), where  $M_{\text{HI}} \sim 10^{-4} M_{\text{dyn}}$  and the value of the molecular gas  $M_{\text{H}_2} \sim 10^{-2} M_{\text{dyn}}$  from Young (2002). Following these ratios we estimate the total gas distribution of the 3 elliptical galaxies (NGC 6125, NGC 6411 and NGC 5966).

In Fig.4.1 and Fig.4.2 we present the inferred gas mass profiles of the 26 E–Sd galaxies with thin black curves and variation ranges given by the dashed-dotted curves. The gas masses  $M_{\text{gas}}$  ranges between  $10^8 - 10^9 M_{\odot}$  for E–Sc to  $10^7 - 10^8 M_{\odot}$  for Scd–Sd. For all galaxies,  $M_{\text{gas}} \ll M_{\star}$ ,  $M_{\text{dyn}}$ .

#### 4.2.4 BARYONIC AND DARK MATTER RADIAL PROFILES

In Sec.4.2.1 we inferred the dynamical masses from the best fit of axisymmetric Jeans solutions based on MGE models, while the baryonic masses are the sum of the stellar (Sec.4.2.2) and gas masses (Sec.4.2.3). Next, we derived the dark matter profiles (blue thick curves) as the difference between the total dynamical and baryonic masses.

In Fig.4.3 and Fig.4.4 we present the mass profiles of the dynamical (black curves), baryonic (orange curves) and dark matter (blue curves) radial profiles of our sample of 26 E–Sd galaxies. The uncertainty of these three mass profiles are presented by dashed curves. Marked are one-fifths of the effective radii  $R_e$  by dotted vertical lines. There is a significant dark matter contents in almost all galaxies, where the dynamical masses are much larger than the baryonic ones (except for galaxy NGC 4254 and NGC 1167 that show similar baryonic and dynamical mass profiles). The most dark matter-dominated objects from the sample are ellipticals (E) and late-type (Scd–Sd) galaxies.

In Fig.4.9 (right panel) we derive the dark matter fraction profiles ( $f_{\text{DM}}$ ) of our 26 galaxies in the following way

$$f_{\text{DM}} = (1 - M_{\text{bar}}/M_{\text{dyn}}), \quad (4.3)$$

where the  $M_{\text{bar}}$  is the total baryonic mass (Sec.4.2.4) and  $M_{\text{dyn}}$  is the dynamical mass from Jeans models (Sec.4.2.1). In Fig.4.9 (right) we compare the dark matter fraction radial profiles, normalized on their effective radii ( $R_e$ ) of both SAURON and CALIFA galaxies throughout the Hubble sequence (color coding). These profiles slightly vary within the radius due to the contribution of the gas to the baryonic mass. For example, the inner parts of the latest-type spirals (Scd–Sd) do not have constant dark matter content for this reason, where the gas content is relatively higher in elliptical and Sb galaxies. Instead, the dynamical and stellar mass profiles have identical shapes, because we use mass-follows-light models for their derivation, i.e., we multiply the same light of

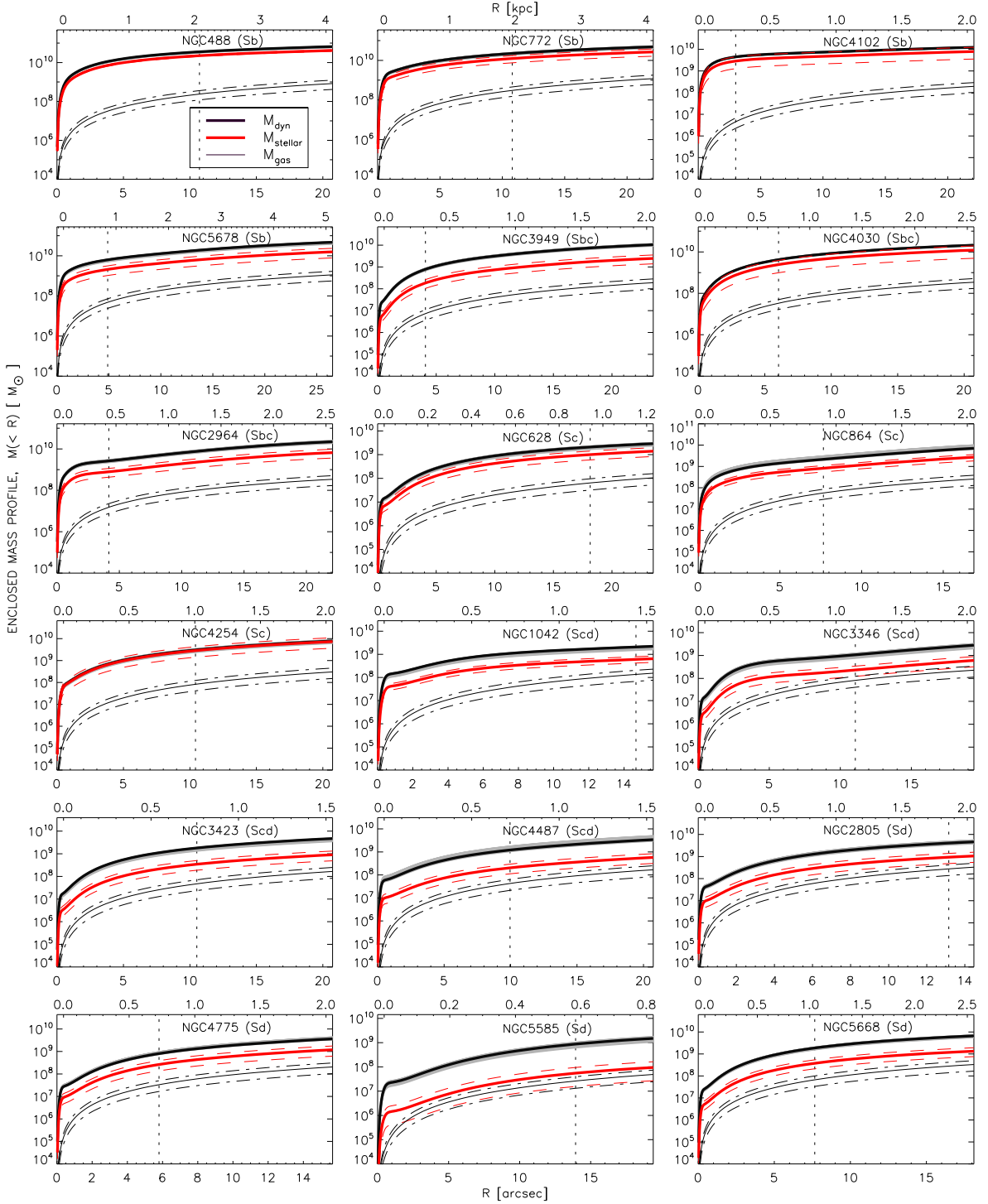


**Figure 4.1:** Enclosed mass profiles of 18 Sb–Sd SAURON galaxies. Thick black solid curves are the inferred dynamical mass profiles from the best fit of axisymmetric Jeans solutions based on MGE models with variation ranges given by the grey band. Thick red curves present the derived stellar mass distribution based on the stellar population analysis of Ganda et al. (2006) with variation ranges given by the dashed red curves. Thin black curves are the modeled gas (HI+H<sub>2</sub>) mass profiles from the universal gas profile of Bigiel & Blitz (2012) for disk galaxies with variation ranges given by the dashed-dotted curves. Overplotted are one-fifth of the effective radii ( $R_e/5$ ), the names and Hubble types of the galaxies.

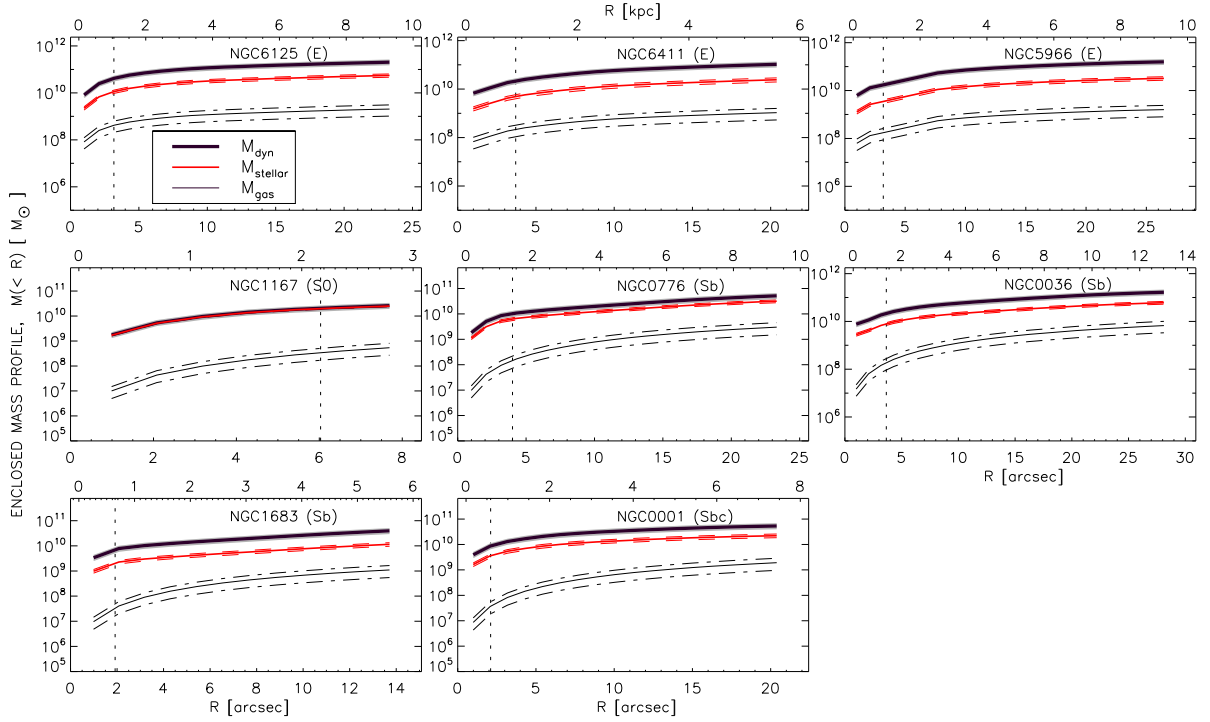


**Figure 4.2:** Enclosed mass profiles of 8 E–Sbc CALIFA galaxies. Thick black solid curves are the inferred dynamical mass profiles from the best fit of axisymmetric Jeans solutions based on MGE models with variation ranges given by the grey band. Thick red curves present the derived stellar mass distribution based on the stellar population analysis of González Delgado et al. (2014) with variation ranges given by the dashed red curves. Thin black curves are the modeled gas (HI+H<sub>2</sub>) mass profiles from the universal gas profile of Bigiel & Blitz (2012) for the 5 Sb-Sbc CALIFA disk galaxies, while the modeled gas for the rest 3 E galaxies is based on the ratios  $M_{\text{HI}}/M_{\text{dyn}}$  of Longair (1998) and  $M_{\text{H}_2}/M_{\text{dyn}}$  of Young (2002). The gas mass variation ranges are given by the dashed-dotted curves. Overplotted are one-fifth of the effective radii ( $R_e/5$ ), the names and Hubble types of the galaxies.

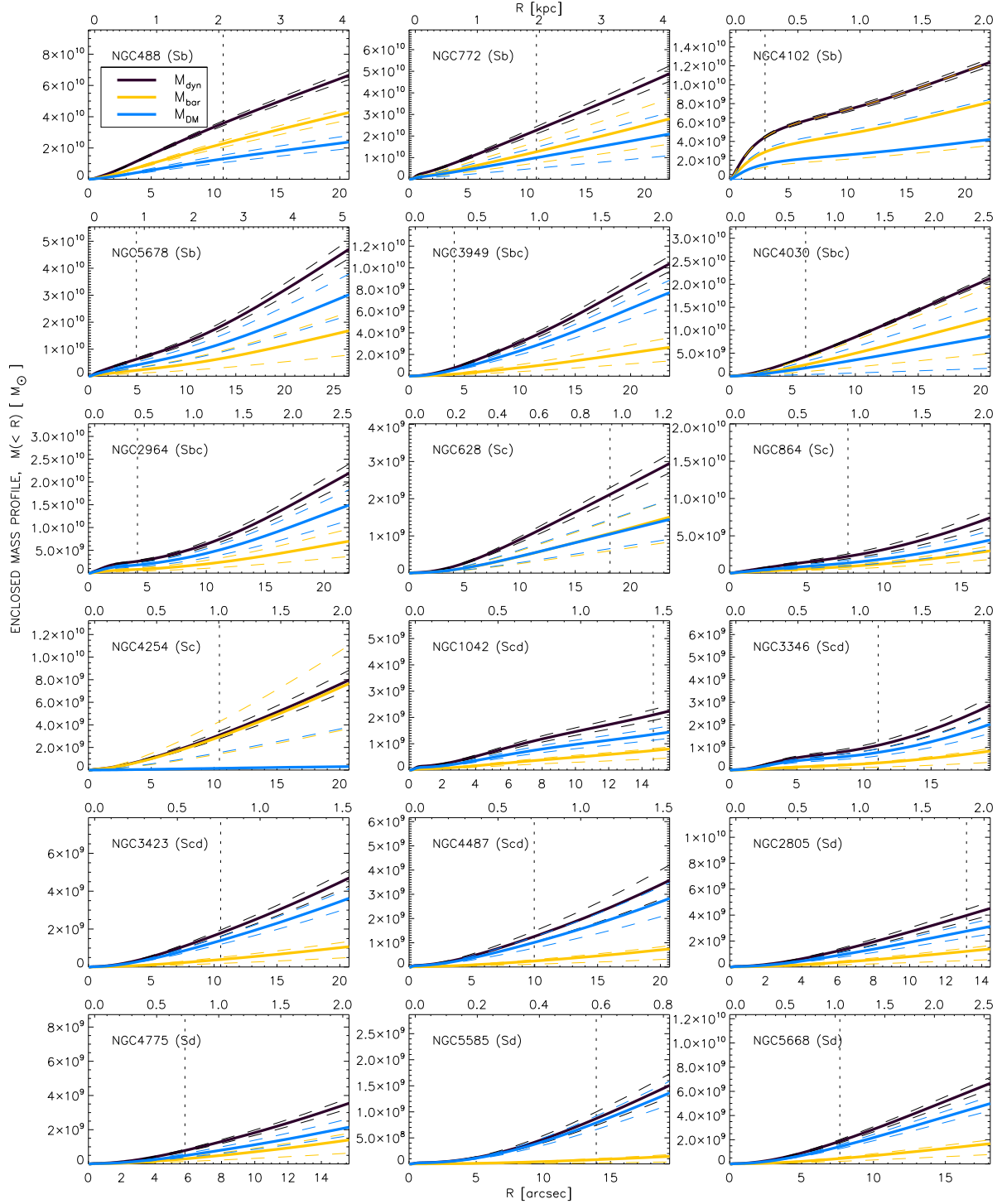
the galaxies by a constant  $\Upsilon_{\text{dyn}}$  and  $\Upsilon_{\star}$ , respectively (see Chap. 3). The comparison shows that elliptical (E) and late-type galaxies (Scd–Sd) have the highest dark matter fractions:  $\sim 70\text{--}90\%$  of their total mass.

### 4.3 INNER DYNAMICAL SCALINGS OF GALAXIES: CORRELATION WITH TOTAL STELLAR MASS

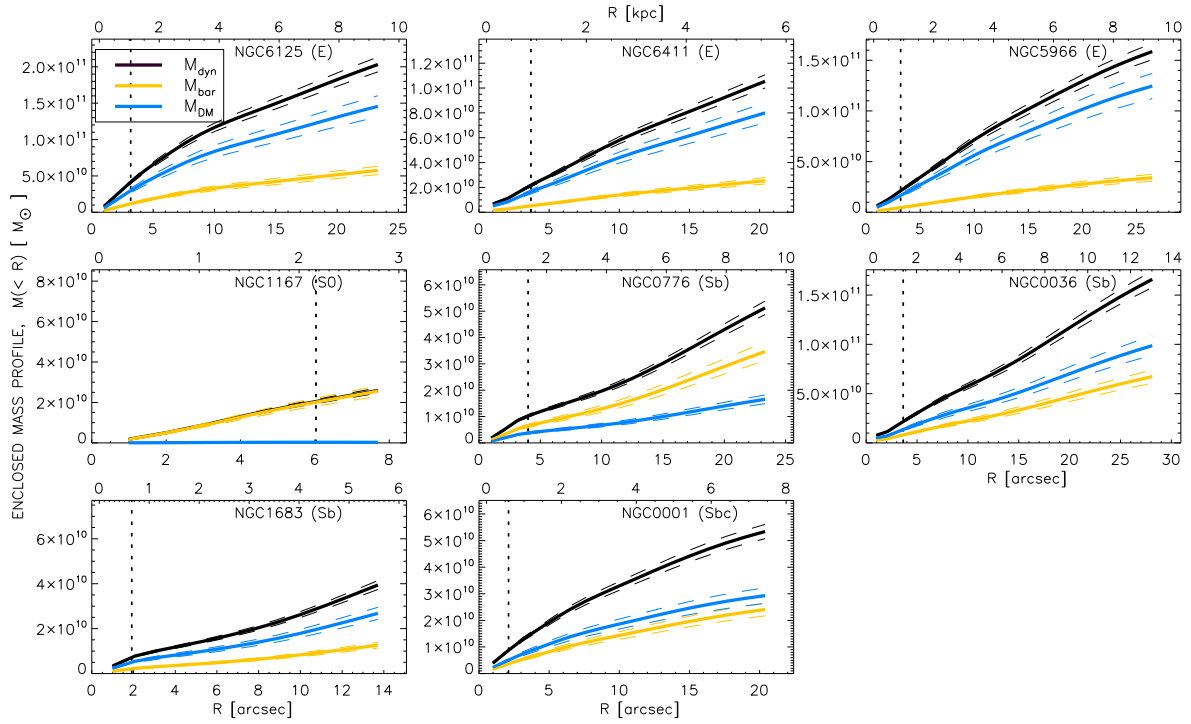
Here, we investigate the connection between dynamical and luminous mass, as well as the relation between kinematics and dark matter content of the 26 E–Sd galaxies. Having inferred the mass profiles in Sec. 4.2, we first build scaling relations of the dynamical mass at  $R_e/5$  with stellar (inner and total), gas and baryonic mass. Further, we derive the ordered-over-random motion ( $V/\sigma$ ) of the galaxies at  $R_e/5$  from the velocity and velocity dispersion profiles, and we then compare their values with the dark matter fractions calculated at the same radius (see Table 4.2 and Table 4.3).

Fig. 4.6 (top panel) presents the dependency of the inner dynamical and stellar mass at  $R_e/5$  with dashed lines of the one-one relations overplotted. The discrepancy between these two masses evidence that the elliptical and Scd–Sd galaxies are mostly dominated by their dark matter halos in contrast with the rest of the galaxies from the sample. Looking at the whole galaxies, in the right panel we compare the total dynamical and total stellar masses. Their ratios do not differ from those of the inner parts, i.e., at  $R_e/5$  (except for Sb galaxy NGC 4102). Additionally, we report that the gas (HI + H<sub>2</sub> contribution to the inner baryonic mass of the galaxy at  $R_e$  is negligible, i.e.,  $10^2 - 10^4 M_{\odot}$ , right bottom panel). For this reason, the baryonic mass fractions of the galaxies at  $R_e$  (left bottom panel) follow the same dependency as the stellar mass fractions (top left).

To complete our investigation about the scaling relations and compare our result with recent studies (Kuzio de Naray & McGaugh 2014), in Fig. 4.7 we probe the dependency of the inner dynamical masses across galaxy morphology with the total stellar masses at 500 pc (left) and at  $R_e/5$  (right). We also find a weak scaling of the dynamical mass at 500 pc ( $M_{\text{dyn}}^{500}$ ) with the total stellar mass in agreement with Kuzio de Naray & McGaugh (2014). The sudden increase in central mass is associated with dominant stellar bulges. This weak scaling is not unexpected, because we compare all galaxies at 500 pc that might have different sizes at this distance, as well as the contribution of different structural components. Therefore, considering the real physical extent of the galaxies, we build the relation at  $R_e/5$  and we find a quite clear scaling of the dynamical masses at  $R_e/5$  with total stellar masses, where  $M_{\text{dyn}}^{\text{Re}/5} \approx (M_{\text{star}}^{\text{tot}})^{0.93}$  (dotted line). This result shows that if we know the total stellar mass of the galaxy, we can predict its inner dynamical



**Figure 4.3:** Dark matter radial profiles of 18 Sb–Sd SAURON galaxies. Thick black solid curves are the inferred dynamical mass profiles from the best fit of axisymmetric Jeans solutions based on MGE models with variation ranges given by the black dashed curves. Thick orange curves presents the total baryonic mass profiles (sum of the stellar and the gas mass profiles) with variation ranges given by the orange dashed curves. Thick blue curves are the dark matter profiles as result of the difference between the dynamical and baryonic mass distributions with variation ranges given by the blue dashed curves. There is a significant dark matter mass in these galaxies, where the dynamical mass is larger than the baryonic one (except for galaxy NGC 4254). The most dark matter-dominated objects are the latest-type galaxies Scd–Sd from SAURON sample.



**Figure 4.4:** Dark matter radial profiles of 8 E–Sbc CALIFA galaxies. Thick black solid curves are the inferred dynamical mass profiles from the best fit of axisymmetric Jeans solutions based on MGE models with variation ranges given by the black dashed curves. Thick orange curves presents the total baryonic mass profiles (sum of the stellar and the gas mass profiles) with variation ranges given by the orange dashed curves. Thick blue curves are the dark matter profiles as resulted from the difference between the dynamical and baryonic mass distributions with variation ranges given by the blue dashed curves. The dark matter fraction is significantly high in these galaxies, where the dynamical mass is larger than the baryonic one (except for galaxy NGC 1167). The most dark matter-dominated objects are the elliptical galaxies E from CALIFA sample.

ical mass. This scaling relation deserves further analysis with a larger sample of galaxies and a bigger field of view of the observations.

To examine the  $(V/\sigma) - f_{DM}$  connection, we need to calculate the ordered-over-random motions of the galaxies and their dark matter fractions at certain radius, i.e., at  $R_e/5$ . In Fig. 4.5 (top panels) we present the velocity ( $V$ , left) and velocity dispersion ( $\sigma$ , right) profiles across Hubble sequence galaxies normalized by their effective radii. Ellipticals (E) and late-type spirals (Scd-Sd) have the lowest values of the rotational velocity in contrast to the S0/Sb-Sc galaxies. However, the velocity dispersion profiles show a smooth transition across the galaxy morphology. It increases from Sd to elliptical galaxies. We also normalize the ordered-over-random motion profiles of the galaxies by their effective radii (bottom left). The  $V/\sigma$  profiles of E and Sd galaxies show consistently low values in contrast to the rest of the galaxies that have steep profiles. The one-to-one relation of  $V/\sigma$  is shown with a dash-dotted line to guide the eye. The right bottom panel shows that dark matter fractions at  $R_e/5$  are anti-correlated with the ratio of the ordered-over-random motion (right), where  $f_{DM}^{R_e/5} = 1 - (V/\sigma)_{R_e/5}$  (dashed line). Dispersion-dominated galaxies, i.e. E and Scd-Sd galaxies, show higher dark matter fractions. Simple kinematic properties directly derivable from observations appear to be a reliable predictor of the dark matter content in the galaxies.

#### 4.4 VELOCITY SCALINGS OF GALAXIES: CONNECTIONS WITH MAXIMAL OR SUB-MAXIMAL DISKS

We can construct scaling relations in the outer parts of the 23 S0-Sd galaxies, e.g. at 2.2 disk scale lengths (see Table 4.1), in order to test the maximal disk theory. To achieve this we need to extrapolate galaxies' circular velocity curves further out from the observational range (see Table 4.1). We assume that the derived rotation curves (RCs) approach their flat parts and investigate if the galaxies have maximal or sub-maximal disks, i.e., if the baryonic mass of the disk or dark matter halo mostly influence the RC shape.

In Fig. 4.8, we compare the stellar  $V_{\star,2.2}$  and dynamical  $V_{dyn,2.2}$  circular velocity curves extrapolated to 2.2 disk scale lengths (top panel). There is a relation for most of our 23 disc galaxies (solid curve), where  $\text{Log}(V_{\star,2.2}) = -1.44 + 1.54 \text{Log}(V_{dyn,2.2})$ . This corresponds to  $V_{\star,2.2} = 0.04 V_{dyn,2.2}^{1.54}$  and differs from the relation  $V_{star,2.2} = 0.85 V_{dyn,2.2}$  expected for “maximal” disks of Sackett (1997) (dashed-dotted curve). There are 7 S0-Sc (mostly Sb) galaxies that approach this relation, while the Scd-Sd late-type spirals differ from it at  $\sim 0.2$  dex. Therefore their rotation curves are mostly driven by the dark matter halo and less by the baryonic mass of the disk, i.e., the disk is sub-maximal.

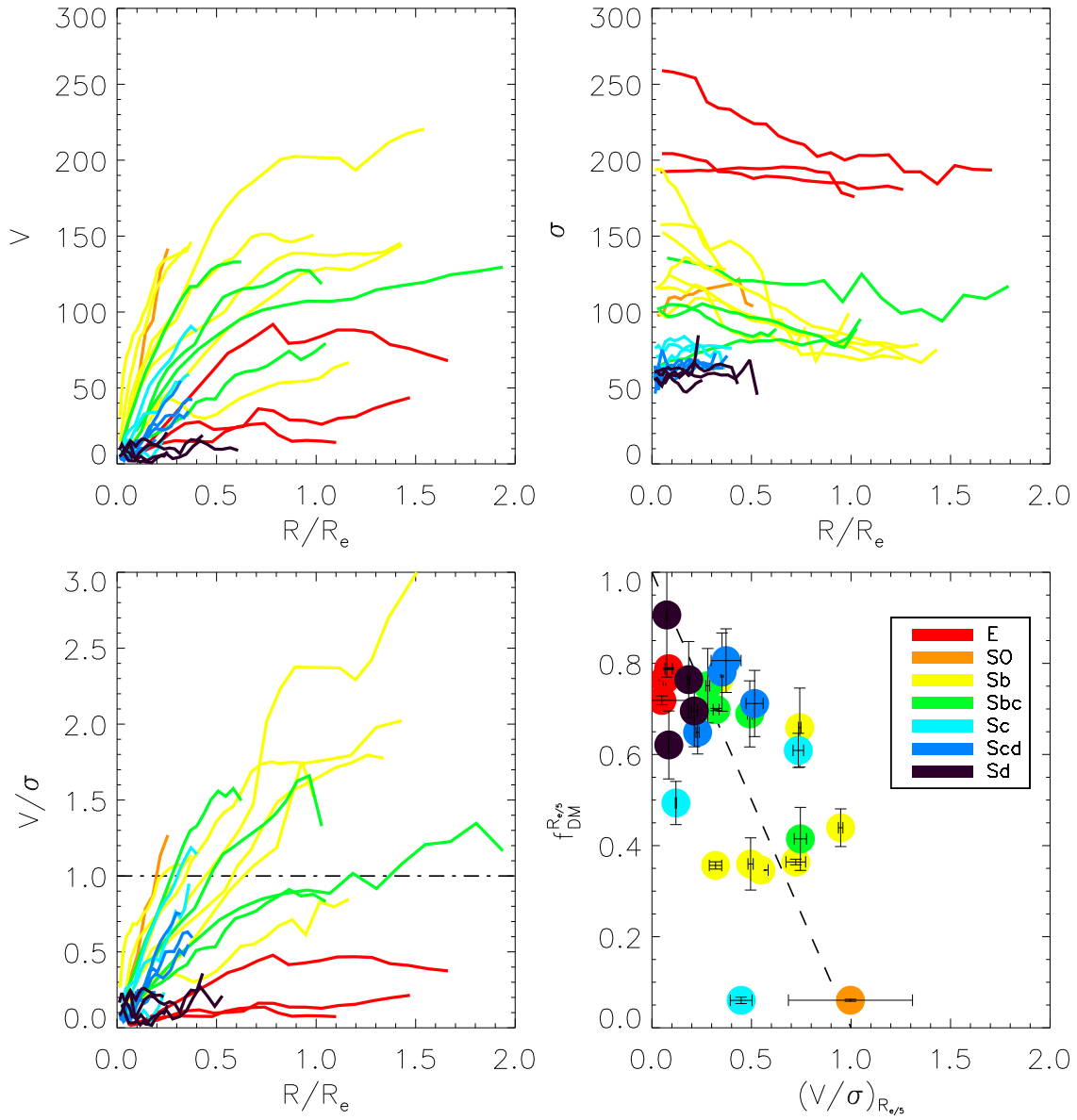


**Figure 4.5:** The link between ordered-over-random motions and dark matter fractions of the 26 E–Sd galaxies at  $R_e/5$ . **Top:** Velocity (left) and Velocity dispersion (right) profiles normalized at the effective radii of the galaxies. The rotation velocity is lower for ellipticals and late-type (Scd–Sd) spirals, while the velocity dispersion increases smoothly across the Hubble sequence from Sd to E galaxies. **Bottom:** The *left panel* presents the ordered-over-random motions of the galaxies normalized at their effective radii. The dash-dotted line corresponds to the one-one relation. The  $V/\sigma$  profiles of elliptical (E) and late-type spiral (Sd) galaxies show constantly low values in contrast to the rest of the galaxies having steep profiles. The *right panel* shows the comparison between the dark matter fractions and ordered-over-random motions at  $R_e/5$ . Elliptical (E) and late-type spiral (Scd–Sd) galaxies are the most dark matter dominated objects, while lenticular (S0) and early-type spirals (Sb) have significantly smaller dark matter fractions. Dark matter fractions are anticorrelated with the ratio of ordered-over-random motion, that is dispersion-dominated galaxies show a higher dark matter fraction. The dashed line corresponds to a linear relation, where  $f_{DM}^{R_e/5} = 1 - (V/\sigma)_{R_e/5}$ .

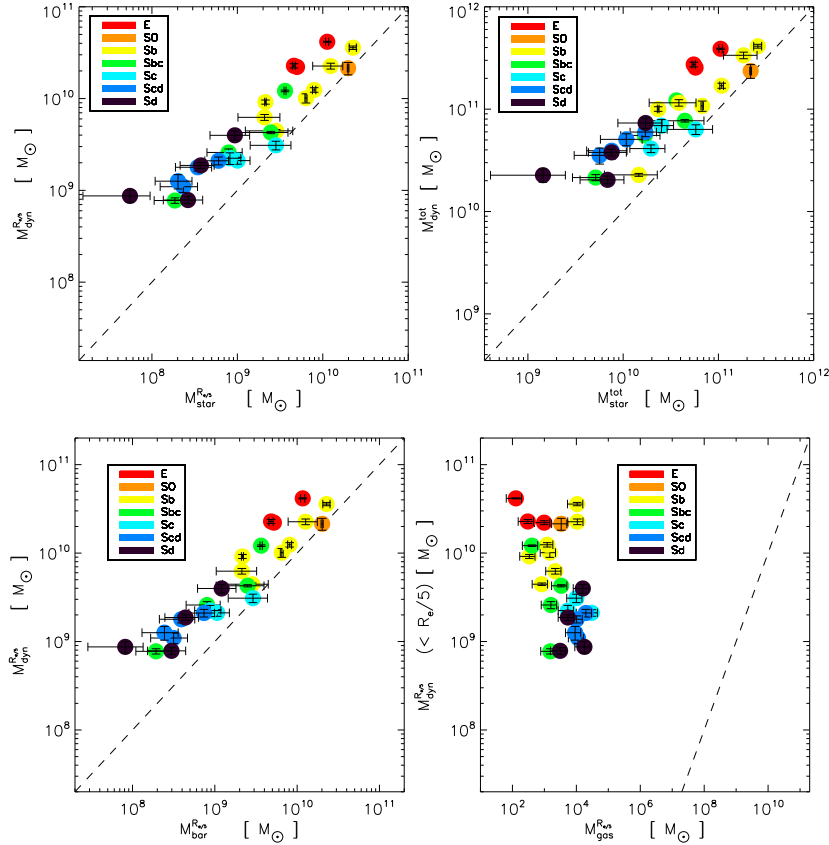


**Figure 4.6:** Inner dynamical and stellar masses of the 26 E–Sd galaxies. The color-coding corresponds to the morphological classification of the galaxies. The one-to-one relations are shown with dashed lines.

*Top:* The left panel presents the relation between inner dynamical masses and inner stellar masses at  $R_e/5$ . The right panel shows the relation between total dynamical masses and total stellar masses. Their comparison evidences that the ratio between the dynamical and stellar mass does not change in the inner and outer parts of the galaxies (except for Sb galaxy NGC 4102). *Bottom:* Dynamical against baryonic (left) and gas (right) masses within  $R_e/5$ . The gas contribution to the inner baryonic mass of the galaxy is negligible (between  $10^2 - 10^4 M_\odot$ ).

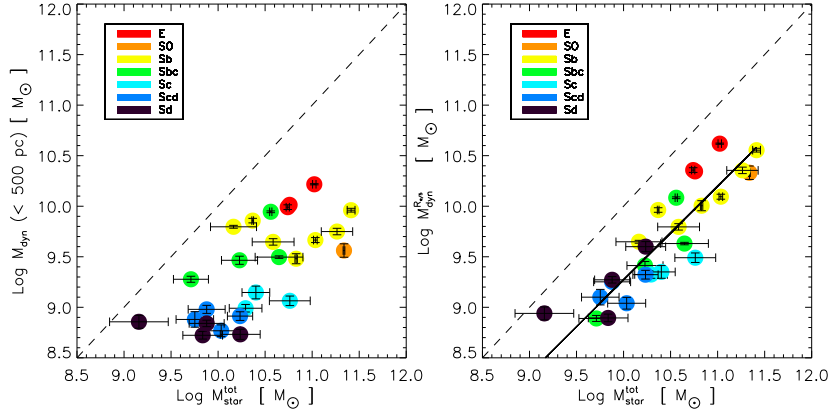


**Figure 4.7:** Scalings of the inner dynamical masses with the total stellar masses at 500 pc (left) and  $R_e/5$  (right). We find a weak scaling of the dynamical mass at 500 pc ( $M_{\text{dyn}}^{500}$ ) with the total stellar mass in agreement with Kuzio de Naray & McGaugh (2014). The sudden increase in central mass is associated with dominant stellar bulges. However, considering the real physical extent of the galaxies, we find a nice scaling of the dynamical masses at  $R_e/5$  with total stellar masses, where  $M_{\text{dyn}}^{\text{Re}/5} \approx (M_{\text{star}}^{\text{tot}})^{0.93}$  (dotted line).

Further, we present a similar analysis in the bottom left panel of Fig. 4.8 including the ratio  $V_{\star,2.2}/V_{\text{dyn},2.2}$  of the galaxies and the total stellar mass of the disk at 2.2 scale lengths. The maximal disk relation of Sackett (1997) is shown with a dashed-dotted curve. Galaxies with higher stellar masses are more close to maximal discs (e.g., S0, Sb galaxies) furnish the upper right corner of the plot, while low-mass galaxies (Scd–Sd) are sub-maximal discs and take the lower left corner. In agreement with the work of Pizagno et al. (2005), we find that  $\text{Log}(V_{\star,2.2}/V_{\text{dyn},2.2}) = -2.17 + 0.27 \text{Log}(M_{\text{disk}})$  (solid line). To make a comparison between our results of external galaxies and the Milky Way, having disk mass of  $(5.3 \pm 0.4) \times 10^{10} M_{\odot}$ ,  $V_{\star,2.2}/V_{\text{dyn},2.2} = 0.83 \pm 0.04$  and stellar disc scale length of  $2.15 \pm 0.14$  (Bovy & Rix 2013), we overplot these values with a triangle symbol above the relation. The Milky Way fits well in the occupation of the rest of the Sb galaxies from the sample.

To study the connection between the size of the disk and the rotation curve, we plot in the bottom right panel of Fig. 4.8 the same dependency between  $V_{\star,2.2}/V_{\text{dyn},2.2}$  and the total stellar disk mass. Here, the color-coding corresponds to the radial scale length of the disk. In our sample, we do not find a clear relation between the maximized contribution of the disk to the rotation curve and its extent. However, the Milky Way better falls along the general trends defined by our sample in contrast to those found by Pizagno et al. (2005) and shown in Bovy & Rix (2013).

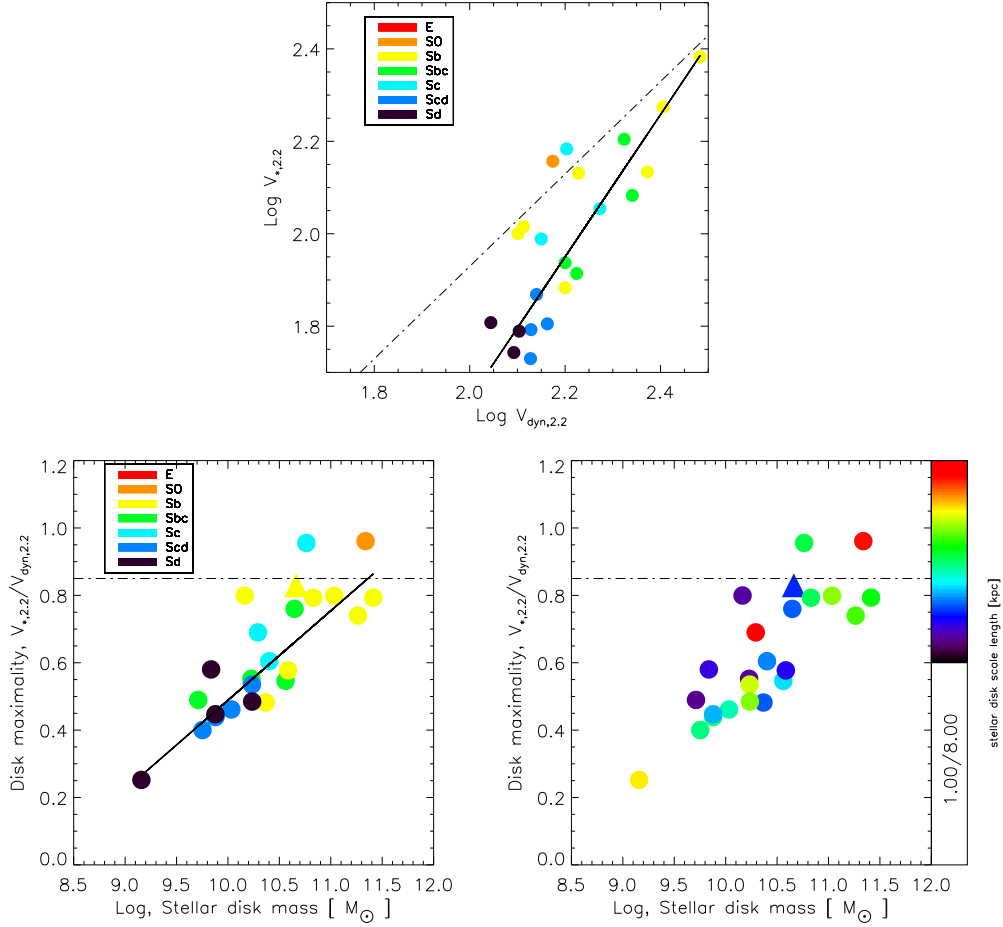


**Figure 4.8:** SAURON and CALIFA disk properties of 23 galaxies (colored points). The dashed-dotted curve shows the relation  $V_{\star,2.2} = 0.85V_{dyn,2.2}$  expected for “maximal” disks (Sackett 1997)

**Top:** Comparison of the stellar  $V_{\star,2.2}$  and the dynamical  $V_{dyn,2.2}$  circular velocity curves at 2.2 disk scale length in logarithmic scale. The solid curve corresponds to a linear fit, where  $\text{Log}V_{\star,2.2} = -1.44 + 1.54 \text{Log}V_{dyn,2.2}$ . The Scd–Sd late-type spiral galaxies significantly differ (with  $\sim 0.2$  dex) from this relation, which means that they are dominated by the dark matter rather than by the baryonic mass of the disk.

**Bottom Left:** Relation between the total stellar mass and the disk’s contribution to the rotation at 2.2 scale lengths (the extent to which the disk is maximal). Points are color-coded by the morphological type. The solid line correspond to a linear fit, where  $\text{Log}(V_{\star,2.2}/V_{dyn,2.2}) = -2.17 + 0.27 \text{Log}(M_{\text{disk}})$ . The Milky Way (from Bovy & Rix 2013) is represented by a triangle.

**Bottom Right:** Relation between the total stellar mass and the disk’s contribution to the rotation at 2.2 scale lengths (the extent to which the disk is maximal). Points are color-coded by the radial scale length of the disk. The Milky Way falls along the general trends defined by these external galaxies, except that its scale length appears short compared to that of similar external galaxies (see also Bovy & Rix 2013). Similar trend of 81 external galaxies is shown in Pizagno et al. (2005). Late-type spirals and low mass galaxies appear dominated by the dark matter halo, while the early-type spirals and high mass galaxies are dominated by the baryonic mass of the disk.

## 4.5 SHAPE OF THE ROTATION CURVES ACROSS HUBBLE SEQUENCE

Similarly to the maximum disk theory, in this section we show that the simple study of rotation curve shapes can be used as a useful alternative to trace the contribution of the luminous mass to the gravitational potential of the galaxies that allow also to include elliptical galaxies.

In Fig.4.9 (left panel), we present the the circular velocity curves of all galaxies normalized at their effective radii ( $R_e$ ). The comparison shows a strong relation between the maximum circular velocities and their morphological types: elliptical galaxies have the highest circular velocities and the value of the rotation curves smoothly decreases towards Sd galaxies. There are approximately four typical ranges for rotational velocity within the 26 galaxies, e.g.,  $\sim 300\text{-}400\text{ km s}^{-1}$  for ellipticals,  $\sim 200\text{-}300\text{ km s}^{-1}$  for Sb,  $\sim 120\text{-}200\text{ km s}^{-1}$  for Sbc and  $\sim 50\text{-}120\text{ km s}^{-1}$  for Sc–Sd. Following the work of Zasov & Kyazumov (1983) and Corradi & Capaccioli (1990), we distinguish four classes of rotation curves depending on their shapes:

*Slow-rising (SR)*: the rotational velocity increases monotonically with the absence of a peak in the centers. This class includes Scd–Sd galaxies.

*Flat(F)*: the rotational velocity is approximately constant within the whole galaxy. This shape is common for Sb–Sbc and maybe S0 galaxies.

*Sharp-peaked (SP)*: the rotational velocity rises steeply and has a round peak by more than 20% of its flat part in the outer parts. E, Sb, Sbc galaxies show this profile.

*Round-peaked (RP)* - the rotational velocity steeply increases and has a round peak by more than 20% of its flat part in the outer parts. This shape is given only by the giant elliptical (gE) galaxy NGC 6125.

There is no relation of the flat and sharp-peaked shapes of the rotation velocity curves with the morphological types of the galaxies. The comparison between the shape of the rotation curves and dark matter fraction profiles (Fig.4.9, right panel) does not show correlation with the morphology of the galaxies. For example, the highest  $f_{DM}$  profiles correspond to E and Scd-Sd galaxies. They also have the highest and the lowest amplitudes of the rotation curve, respectively.

## 4.6 DISCUSSION

The Hubble sequence (Hubble 1936) is a classification of galaxies based on their photometry. In our study of 26 E–Sd galaxies, we note that the galaxies can be also categorized depending on their dynamics. Similar ideas are discussed in various studies (Spitzer & Baade 1951; van den Bergh 1976; Poggianti et al. 1999).

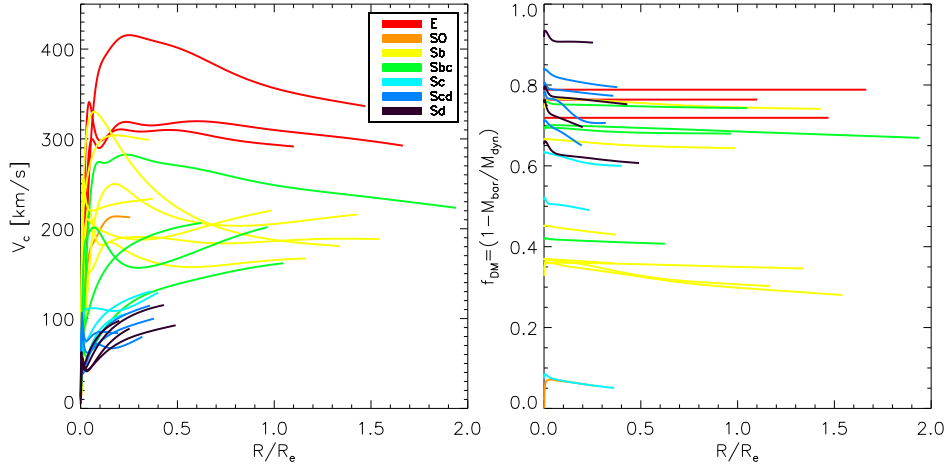


**Figure 4.9:** Hubble sequence circular velocity curves and dark matter fractions of the 26 E–Sd galaxies. The color coding corresponds to different morphological types. *Left:* Dark matter fraction radial profiles of the galaxies, defined as  $f_{DM} = (1 - M_{bar}/M_{dyn})$  and normalized at their effective radii ( $R_e$ ). Elliptical (E) and late-type galaxies (Scd–Sd) have the highest dark matter fractions. *Right:* Circular velocity curves of the galaxies, normalized on their effective radii ( $R_e$ ). There is a clear trend between the maximum circular velocities of the galaxies and their morphological types.

The recent study of 260 early-type galaxies (E/S0) by Cappellari et al. (2011a) as part of ATLAS<sup>3D</sup> project give an overview of the limitations of the classic Hubble (1936) tuning-fork diagram. They show, instead, the usefulness of a scheme similar to the one proposed by van den Bergh (1976) to properly understand the morphology of early type galaxies. The author consider two classes of objects: (i) slow rotators, which are consistent with being genuinely elliptical-like objects with intrinsic ellipticity  $\epsilon \gtrsim 0.4$ ; and (ii) the fast rotators, which are generally flatter than  $\epsilon \lesssim 0.4$  and are morphologically similar to spiral galaxies, or in some cases to flat ellipticals with discy isophotes, and span the same full range of bulge sizes of spirals. The presented revised comb-shaped scheme illustrates the morphology of nearby galaxies, which overcomes the limitations of the tuning-fork diagram.

#### 4.6.1 DYNAMICAL CLASSIFICATION OF GALAXIES

The comparison between the shapes of the rotation curves (RC) and the distribution of the stellar mass can provide insight into the amount and distribution of dark matter in galaxies, and it can be used to study the connection between the structural properties of the dark and luminous components. This connection is probably the result of galaxy formation processes.

In Sec. 4.5, we categorize the rotation curves of our galaxies depending on their shape, and hence propose four classes: slow-rising (SR), flat (F), sharp-peaked (SP) and round-peaked (RP) galaxies. Linking this RC categorization with the results of our kinematic and dynamical analyses, we design a "Dynamical classification" of the 26 E–Sd galaxies shown in Fig. 4.10. In the third row panels, we also present a scheme of the components of each galaxy class considering the results in the thesis. We focus on four main parts of the galaxies: dark matter halo (bright blue), thick disk (dark blue), thin disk (orange) and spheroid/bulge (red).

All galaxies are embedded in extensive dark matter halos (e.g., Bosma 1978; Rubin & Ford 1983; Springel et al. 2005; Klypin et al. 2011) and therefore we consider similar dark matter halos for all classes. It might be possible that dark matter halo profile (e.g., core, cusp, NFW, spherical) varies between the dynamical classes, however this is beyond the scope of our study. In Chapter 3, we learn that the galaxies can not be approximated by thin disks if their ordered-over-random motion  $V/\sigma \ll 1.5$  due to influence of thick bulges and/or thick disks. Thus,  $V/\sigma$  profiles (second row panels) show the presence of either both components. If this is the case, looking at the amplitude of the RC peak we can understand if the low ordered-over-random motion is caused by the spheroidal/bulge component or the thick disk of the galaxy. The high RC peak corresponds to a dense and large central component (e.g., Sb galaxies, sharp-peaked), while its absence is evidence for a dominance of a thick disk (e.g., Scd–Sc galaxies, slow-rising). If there is a significant contribution from both, then a flat shape of the RC may be expected. This might explain why flat/sharp-peaked class (e.g., Sb) galaxies are close to maximal disks due to the large contribution of the luminous mass from the thin disk (young stars), while slow-rising class (Scd–Sd) galaxies have sub-maximal disks due to the smaller contribution of the luminous mass from the thin disk. Therefore, it is expected that the dark matter content in slow-rising galaxies is higher than the flat/sharp-peaked ones. In the fifth row panels, we show that this is exactly the case, where slow-rising galaxies have almost two times higher dark matter fractions.

In Sec. 4.3 we find a quite clear anti-correlation between the dark matter fraction and the ratio of ordered-over-random motion. Round-peaked galaxies (e.g., E) are the most dark matter dominated objects with  $f_{DM} \sim 70 - 80$ . Slow-rising (Scd–Sd) and round-peaked (E) classes show similarly low ordered-over-random motion, indicating that both classes are dispersion dominated objects. However, in terms of dynamical masses they are different (fourth row panels): the slow-rising class are presented by low-mass ( $M_{\text{dyn}} \sim 10^9 M_{\odot}$ ) galaxies, while the round-peaked class is related to high-mass ( $M_{\text{dyn}} \sim 10^{11} M_{\odot}$ ) galaxies.

<b>Dynamical classification</b>			
slow-rising	flat	sharp-peaked	round-peaked
Scd-Sd	S0, Sb, Sbc	E, Sb, Sbc	giant E
$M_{\text{dyn}} \sim 10^9 M_{\odot}$	$M_{\text{dyn}} \sim 10^{10} M_{\odot}$	$M_{\text{dyn}} \sim 10^{10} - 10^{11} M_{\odot}$	$M_{\text{dyn}} \sim 10^{11} M_{\odot}$
$f_{\text{DM}} \sim 0.70 - 0.90$	$f_{\text{DM}} \sim 0.30 - 0.40$	$f_{\text{DM}} \sim 0.60 - 0.70$	$f_{\text{DM}} \sim 0.70 - 0.80$

**Figure 4.10:** Dynamical classification of the 26 SAURON and CALIFA galaxies into four classes based on the shape of the circular velocity curves. From left to right columns, the classes are: slow-rising, flat, sharp-peaked and round-peaked. The first row panels present the typical profiles of the rotation curves for each class; second – the ordered-over-random motion profiles; third – the structure of the different components (bright blue - dark matter halo, dark blue - thick disc, orange - thin disc, red - bulge); fourth – Hubble type of the galaxies from each class; fifth – typical masses, sixth – average dark matter fractions.

## 4.6.2 LINK WITH RECENT SIMULATIONS IN GALAXY FORMATION

It is interesting now to investigate why galaxies with low and high masses are the most velocity-dispersion and dark matter-dominated objects from the sample.

Galaxy formation states evidences that dark matter first collapses into small haloes, which merge to form progressively larger haloes. Then the gas cools towards the centre of these dark matter halos and forms stars (White & Rees 1978; Mo et al. 2010). Further, the gas collapses into the dark matter halos by radiating away its energy and settles onto a rotating disc from which stars form.

The infall of the gas on to the disc is controlled by the radiative cooling, which is one of the most important processes of galaxy formation. It might be slowed down by a number of factors including thermal pressure (Binney 1977; Rees & Ostriker 1977) and the incident radiation field (Rees 1986; Efstathiou 1992; Cantalupo 2010; Gnedin & Hollon 2012). The cooling rate of halo gas is critical to define how much fuel is present to form stars in the galaxy. For example, the photoionization can prevent the gas from cooling into low-mass halos (Rees 1986; Efstathiou 1992).

Kannan et al. (2014) investigate the effect of local ionizing radiation fields in full cosmological simulations of a Milky Way-like galaxy. They simulate the galaxy with and without the local radiation field and find that the radiation field reduces star formation after  $z \sim 1.5$  and results in  $\sim 40$  percent less stellar mass. The reduced star formation is due to a combination of factors. The hot, diffuse halo gas surrounding the disc has a higher temperature when the local photoionizing field is considered because a small amount of ionizing radiation from local sources has a big effect on the gas cooling and heating rates at low densities, which in turn raises the equilibrium temperature of the gas. This increased temperature of the hot halo gas provides pressure support to the halo gas against the gravitational potential of the galaxy and hence reduces the gas accretion rate on to the disc. This coupling of the local radiation field to the gas cooling in the host galaxy provides a preventive feedback mechanism that reduces the gas accretion to the central regions of the galaxy, regulating star formation.

The local ionizing radiation field also eliminates high-density, low-temperature gas by raising the equilibrium temperature of the dense gas in the disc. The higher average temperature of the disc gas provides pressure support to the gaseous disc that stops the disc from fragmenting and forming stars. All these effects on the gas distribution by the local radiation field cause the galaxy to form a light and more stable stellar disc, which has a slowly rising rotation curve which peaks at  $200 \text{ km s}^{-1}$ , consistent with observations of MW-like galaxies.

Moster et al. (2010) characterize the relationship between the stellar masses of galaxies and

the masses of the dark matter halos in which they live at low and high redshift, and to make predictions of stellar mass dependent galaxy clustering at high redshift.

They use a high-resolution N-body simulation and identify halos and subhalos. Halos and subhalos were populated with central and satellite galaxies using a parameterized stellar-to-halo mass (SHM) relation. For host halos, the mass is given by the virial mass  $M_{vir}$  while for subhalos they use the maximum mass of the halo over its history  $M_{max}$  since it is expected for the stellar mass of the satellite galaxies to be more tightly linked to this quantity.

Further, they describe the ratio between stellar and halo mass to be function of four free parameters, a low-mass slope  $\beta$ , a characteristic mass  $M_1$ , a high-mass slope  $\gamma$ , and a normalization  $(m/M)_0$ . They fit the values of these parameters by requiring that the observed galaxy stellar mass function (SMF) is reproduced. The authors find that the SHM function has a characteristic peak at  $M_1 \sim 10^{12} M_\odot$ , and declines steeply toward both smaller mass ( $\beta \sim 1$ ) and less steeply toward larger mass halos ( $\gamma \sim 0.6$ ). The physical interpretation of this behavior is the interplay between the various feedback processes that impact the star formation efficiency. Supernova feedback is more effective at reheating and expelling gas in low-mass halos, while AGN feedback is more effective in high mass halos (e.g., Shankar et al. 2006; Croton et al. 2006; Bower et al. 2006; Somerville et al. 2008). In this picture, the characteristic mass  $M_1$  is the halo mass where the efficiency of these two processes crosses.

Therefore, the low star formation efficiency of low- and high-mass galaxies is the link between the high dark matter fractions and the low ordered-over-random motions. In this cases the gas is not completely settled onto a rotating disc from which stars form and galaxies are dispersion dominated. Additionally, local photionizing fields, SNe and AGN feedbacks shape the rotation curve of the galaxies with different masses. The local photionizing field (or SNe) and the AGN feedbacks are the mechanisms that stop the gas to cool and form stars in low- and high-mass galaxies, respectively. If they do not occur, the star formation efficiency increases and the galaxy bulge/spheroid grows. Therefore, a peak in the rotation curve of the galaxies is expected.

## 4.7 CONCLUSIONS

In this chapter, we obtain the dynamical, stellar and gas mass distributions of 26 E–Sd SAURON and CALIFA galaxies. The dynamical mass profiles come from the deprojection of the surface brightness profiles (MGE) of the galaxies, multiplying by their dynamical mass-to-light ratio  $\Upsilon_{dyn}$ , which is calculated from Jeans axisymmetric model approach. The stellar mass profiles are derived from the same surface brightness profiles of the galaxies, but also multiplying by their stellar mass-to-light ratio  $\Upsilon_\star$  coming from stellar population analysis. We use a universal

**Table 4.1:** Photometric properties and dynamical modelling results of the 26 E–Sd galaxies: (1) Galaxy name; (2) Hubble type of CALIFA galaxies (Husemann et al. 2013) and SAURON galaxies (NASA/IPAC Extragalactic Database, NED); (3) Galactocentric distance in Mpc (NED); (4) Scale lengths of the discs in arcsec, measured by Ganda et al. (2009) for SAURON galaxies, and by Ruiz-Lara et al. (2013) and Ruiz-Lara et al., in preparation for CALIFA galaxies; (5) Total Luminosity in r-band for CALIFA and H-band for SAURON galaxies presented in  $10^{10} L_{\odot}$ ; (6) and (7) JAM best fit total dynamical mass-to-light ratios and their uncertainties in r-band for CALIFA and H-band for SAURON galaxies presented in solar units; (8) and (9) Stellar mass-to-light ratios and their uncertainties in r-band for CALIFA and H-band for SAURON galaxies presented in solar units; (10) optical radii in arcsec, defined as the 25 mag arcsec<sup>-2</sup> B-band isophote from RC3.

Name	Type	D (Mpc)	$h_{\text{disc}}$ (")	$L_{\text{tot}}$ ( $10^{10} L_{\odot}$ )	$\Upsilon_{\text{dyn}}$ ( $M_{\odot}/L_{\odot}$ )	$\Delta\Upsilon_{\text{dyn}}$ ( $M_{\odot}/L_{\odot}$ )	$\Upsilon_{\star}$ ( $M_{\odot}/L_{\odot}$ )	$\Delta\Upsilon_{\star}$ ( $M_{\odot}/L_{\odot}$ )	$r_{25}$ (")
(1)	(2)	(3)	(4)	(5)	(6)	(7)	(8)	(9)	(10)
<b>CALIFA</b>									
NGC 6125	E	68.60	–	6.31	6.16	0.08	1.67	0.07	42.4
NGC 6411	E	54.90	–	4.36	5.84	0.30	1.32	0.05	68.7
NGC 5966	E	63.10	–	3.62	7.54	0.40	1.52	0.06	54.6
NGC 1167	S0	69.10	64.48	7.87	3.00	0.46	2.77	0.06	82.6
NGC 0776	Sb	68.80	39.76	3.33	3.23	0.37	2.03	0.06	52.1
NGC 0036	Sb	84.30	49.45	4.83	3.51	0.20	2.24	0.10	65.6
IC 1683	Sb	68.70	25.78	1.62	6.20	0.32	1.44	0.03	39.5
NGC 0001	Sbc	64.70	31.53	2.47	4.93	0.10	1.47	0.04	48.7
<b>SAURON</b>									
NGC 488	Sb	32.14	43.29	35.53	1.16	0.05	0.73	0.07	157.5
NGC 772	Sb	35.63	46.30	35.33	0.95	0.07	0.52	0.20	217.5
NGC 4102	Sb	15.47	16.94	3.74	0.61	0.02	0.39	0.22	90.5
NGC 5678	Sb	31.28	20.67	9.38	1.23	0.09	0.41	0.21	99.5
NGC 3949	Sbc	14.59	15.85	1.47	1.46	0.10	0.35	0.15	86.5
NGC 4030	Sbc	21.08	26.22	10.84	0.71	0.02	0.41	0.24	125.0
NGC 2964	Sbc	20.65	16.68	3.93	1.41	0.13	0.43	0.19	86.5
NGC 628	Sc	9.76	70.35	3.92	1.05	0.09	0.50	0.20	314.5
NGC 864	Sc	21.82	27.81	4.76	1.45	0.21	0.53	0.18	140.5
NGC 4254	Sc	19.41	40.55	13.78	0.46	0.05	0.42	0.21	161.0
NGC 1042	Scd	18.06	52.35	3.11	1.92	0.19	0.55	0.17	140.5
NGC 3346	Scd	18.89	36.09	2.51	2.02	0.27	0.43	0.20	86.5
NGC 3423	Scd	14.74	38.04	1.80	2.18	0.20	0.42	0.19	114.0
NGC 4487	Scd	14.68	38.20	1.53	2.31	0.41	0.37	0.17	125.0
NGC 2805	Sd	28.17	49.06	4.00	1.83	0.21	0.43	0.21	189.5
NGC 4775	Sd	22.46	19.59	1.96	1.04	0.09	0.35	0.17	64.0
NGC 5585	Sd	8.24	54.89	0.45	5.03	0.74	0.32	0.23	172.5
NGC 5668	Sd	23.89	29.63	2.16	1.75	0.13	0.35	0.15	99.5

**Table 4.2:** Inferred enclosed masses of 26 E–Sd galaxies within an one-fifth of the effective radius ( $R_e/5$ ): (1) Galaxy name; (2) Hubble type of CALIFA galaxies (Husemann et al. 2013) and SAURON galaxies (NASA/IPAC Extragalactic Database, NED); (3) and (4) Dynamical masses from Jeans modeling and their uncertainties in  $10^9$  solar masses; (5) and (6) Stellar masses modelled by using  $\Upsilon_*$  from stellar population analysis and their uncertainties in  $10^9$  solar masses; (7) and (8) Gas (HI + H<sub>2</sub>) masses from a universal exponential profile model and their uncertainties in  $10^3$  solar masses; (9) and (10) Baryonic masses as a sum the of the stellar and gas masses, and their uncertainties in  $10^9$  solar masses;

Name	Type	$M_{dyn}^{Re/5}$ ( $10^9 M_\odot$ )	$\Delta M_{dyn}^{Re/5}$ ( $10^9 M_\odot$ )	$M_\star^{Re/5}$ ( $10^9 M_\odot$ )	$\Delta M_\star^{Re/5}$ ( $10^9 M_\odot$ )	$M_{gas}^{Re/5}$ ( $10^3 M_\odot$ )	$\Delta M_{gas}^{Re/5}$ ( $10^3 M_\odot$ )	$M_{bar}^{Re/5}$ ( $10^9 M_\odot$ )	$\Delta M_{bar}^{Re/5}$ ( $10^9 M_\odot$ )
(1)	(2)	(3)	(4)	(5)	(6)	(7)	(8)	(9)	(10)
<b>CALIFA</b>									
NGC6125	E	41.58	0.54	11.27	0.47	0.13	0.06	11.69	0.68
NGC6411	E	22.10	1.14	4.99	0.19	0.98	0.49	5.22	0.30
NGC5966	E	22.78	1.21	4.59	0.18	0.30	0.15	4.82	0.30
NGC1167	S0	21.44	3.29	19.80	0.43	3.36	1.68	20.14	0.60
NGC0776	Sb	10.11	1.16	6.36	0.19	1.48	0.74	6.51	0.26
NGC0036	Sb	12.42	0.71	7.93	0.35	1.23	0.61	8.12	0.45
IC1683	Sb	9.17	0.47	2.13	0.04	0.34	0.17	2.17	0.06
NGC0001	Sbc	12.13	0.25	3.62	0.10	0.41	0.20	3.65	0.12
<b>SAURON</b>									
NGC488	Sb	35.84	1.54	22.56	2.16	10.60	5.30	22.79	2.28
NGC772	Sb	22.62	1.67	12.38	4.76	10.76	5.38	12.69	4.92
NGC4102	Sb	4.45	0.15	2.84	1.60	0.83	0.42	2.85	1.61
NGC5678	Sb	6.25	0.46	2.08	1.07	2.20	1.10	2.13	1.09
NGC3949	Sbc	0.78	0.05	0.19	0.08	1.54	0.77	0.19	0.08
NGC4030	Sbc	4.27	0.12	2.47	1.44	3.37	1.68	2.50	1.46
NGC2964	Sbc	2.59	0.24	0.79	0.35	1.60	0.80	0.80	0.36
NGC628	Sc	2.11	0.18	1.00	0.40	30.34	15.17	1.07	0.43
NGC864	Sc	2.24	0.32	0.82	0.28	5.42	2.71	0.88	0.31
NGC4254	Sc	3.09	0.34	2.82	1.41	10.02	5.01	2.91	1.45
NGC1042	Scd	2.10	0.21	0.60	0.19	19.87	9.94	0.74	0.25
NGC3346	Scd	1.10	0.15	0.23	0.11	11.28	5.64	0.32	0.15
NGC3423	Scd	1.79	0.16	0.34	0.16	10.20	5.10	0.39	0.18
NGC4487	Scd	1.26	0.22	0.20	0.09	9.15	4.57	0.24	0.11
NGC2805	Sd	3.98	0.46	0.94	0.46	15.98	7.99	1.21	0.59
NGC4775	Sd	0.78	0.07	0.26	0.13	3.10	1.55	0.30	0.14
NGC5585	Sd	0.87	0.13	0.06	0.04	17.90	8.95	0.08	0.05
NGC5668	Sd	1.87	0.14	0.37	0.16	5.41	2.71	0.44	0.19

**Table 4.3:** Inner and total masses, ordered-over-random motions and dark matter fractions of the 26 E–Sd galaxies: (1) Galaxy name; (2) Hubble type of CALIFA galaxies (Husemann et al. 2013) and SAURON galaxies (NASA/IPAC Extragalactic Database, NED); (3) and (4) Dynamical masses from Jeans modeling within 500 pc and their uncertainties in  $10^9$  solar masses; (5) and (6) Total dynamical (from Jeans modeling) and stellar masses (modelled by using  $\Upsilon_*$  from stellar population analysis) for the whole galaxies and their uncertainties in  $10^{10}$  solar masses; (7) and (8) Ordered-over-random motion and their uncertainties at  $R_e/5$ ; (9) and (10) Dark matter fractions at  $R_e/5$  ( $f_{DM} = 1 - M_{bar}/M_{dyn}$ ) and their uncertainties;

Name	Type	$M_{dyn}^{500}$ ( $10^9 M_\odot$ )	$\Delta M_{dyn}^{500}$ ( $10^9 M_\odot$ )	$M_\star^{tot}$ ( $10^{10} M_\odot$ )	$M_{dyn}^{tot}$ ( $10^{10} M_\odot$ )	$(V/\sigma)^{Re/5}$	$\Delta(V/\sigma)^{Re/5}$	$f_{DM}^{Re/5}$	$\Delta f_{DM}^{Re/5}$
(1)	(2)	(3)	(4)	(5)	(6)	(7)	(8)	(9)	(10)
<b>CALIFA</b>									
NGC6125	E	16.48	0.21	10.54	38.87	0.050	0.263	0.719	0.010
NGC6411	E	10.31	0.53	5.76	25.46	0.063	0.006	0.764	0.001
NGC5966	E	9.79	0.52	5.50	27.29	0.084	0.019	0.788	0.002
NGC1167	S0	3.64	0.56	21.80	23.61	0.997	0.312	0.060	0.002
NGC0776	Sb	3.02	0.35	6.76	10.76	0.319	0.031	0.357	0.008
NGC0036	Sb	4.62	0.26	10.82	16.95	0.547	0.037	0.346	0.000
IC1683	Sb	7.20	0.37	2.33	10.04	0.337	0.012	0.764	0.005
NGC0001	Sbc	8.81	0.18	3.63	12.18	0.322	0.015	0.699	0.002
<b>SAURON</b>									
NGC488	Sb	9.13	0.39	25.94	41.21	0.723	0.049	0.364	0.006
NGC772	Sb	5.61	0.41	18.37	33.56	0.948	0.011	0.439	0.041
NGC4102	Sb	6.26	0.21	1.46	2.28	0.496	0.013	0.360	0.057
NGC5678	Sb	4.44	0.32	3.85	11.54	0.742	0.006	0.659	0.087
NGC3949	Sbc	1.89	0.13	0.51	2.15	0.280	0.010	0.751	0.082
NGC4030	Sbc	3.14	0.09	4.44	7.70	0.746	0.031	0.415	0.069
NGC2964	Sbc	2.92	0.27	1.69	5.54	0.491	0.012	0.689	0.073
NGC628	Sc	0.98	0.08	1.96	4.12	0.120	0.003	0.494	0.047
NGC864	Sc	1.40	0.20	2.52	6.90	0.735	0.026	0.609	0.037
NGC4254	Sc	1.16	0.13	5.79	6.34	0.448	0.055	0.060	0.007
NGC1042	Scd	0.82	0.08	1.71	5.97	0.229	0.008	0.649	0.048
NGC3346	Scd	0.59	0.08	1.08	5.07	0.516	0.043	0.712	0.073
NGC3423	Scd	0.95	0.09	0.76	3.92	0.352	0.007	0.781	0.086
NGC4487	Scd	0.76	0.13	0.57	3.53	0.372	0.075	0.806	0.070
NGC2805	Sd	0.54	0.06	1.72	7.32	0.213	0.016	0.696	0.079
NGC4775	Sd	0.53	0.05	0.69	2.04	0.085	0.002	0.621	0.075
NGC5585	Sd	0.72	0.11	0.14	2.26	0.075	0.004	0.906	0.136
NGC5668	Sd	0.69	0.05	0.76	3.78	0.185	0.006	0.764	0.084

exponential gas profile to model the distribution of the gas mass from the optical radii  $r_{25}$  of the galaxies. The gas mass contribution to the baryonic mass of the galaxies is almost negligible (between 1% to 10% from  $M_{dyn}$  for early- and late-type galaxies, respectively) within 2 effective radii. Thus, we compare the dynamical and baryonic mass of the galaxies throughout the Hubble sequence.

We find that ellipticals (E) and late-type galaxies (Scd–Sd) are the most dark matter-dominated galaxies from the complete sample with fractions  $f_{DM} \sim 70\text{--}80\%$  and  $\sim 80\text{--}95\%$ , respectively. The lenticular (S0) and early-type spirals (Sa–Sb) have significantly smaller dark matter fractions. E and Scd-Sd galaxies tend to have the lowest ordered-over-random motion values due to the spheroidal shape of the ellipticals and the thick disc of late-type spirals. Dark matter appears anti-correlated with the ratio of ordered-over-random motion, i.e. dispersion-dominated galaxies show higher dark matter fractions. Finally, we investigate the maximum circular velocities and qualitative shape of rotation curves as a function of galaxy morphological type along the Hubble sequence. Peaked rotation curves are found in early-type galaxies, while slowly rising rotation curves are typical for late-type spirals. This confirms the predictions of recent simulations of galaxy evolution with local photoionization, SNe and AGN feedback. More generally, our results for dark matter content and dynamics provide empirical constraints on current and future theoretical models of galaxy evolution across a wide range of galaxy morphological types and masses, and thereby will help to understand the relevant physics involved in the galaxy formation process.



## SUMMARY AND FUTURE WORK

### **SUMMARY: $V/\sigma$ AS A KEY PARAMETER IN THE GALAXY FORMATION**

The work presented in this thesis is focused on the precise dynamical modeling of the mass distribution of galaxies throughout the Hubble sequence. We aimed to reach a better understanding of the connection between galaxy kinematics and dark matter contents.

SAURON and CALIFA samples demonstrate that galaxies may not be approximated as thin discs. In particular, exploring two dynamical modelling approaches, we found out that the thin disc assumption is not applicable when a galaxy's local ordered-over-random motion is less than 1.5, i.e., the stars are moving mostly on extraplanar elliptical orbits. This fact might be expected for elliptical galaxies due to their round shapes, but it is surprising for spiral galaxies. Therefore, a large fraction of stars in these systems are organized in bulges (Sb–Sbc) or thick discs (Scd–Sd). Additionally, we noted that the most dark matter-dominated galaxies of our sample are those having low ordered-over-random motions at all radii – ellipticals (E) and late-type spirals (Scd–Sd). The connection between these two parameters is presented by the star formation efficiency (SFE) of the galaxies. [Moster et al. \(2010\)](#) show that both low- and high-mass galaxies are characterized by low SFE, where the dark matter halo mostly contributes to the shape of the rotation curve in comparison with the stellar mass. In this case, the gas does not settle onto a rotating disc from which stars form, and hence the velocity dispersion is much larger than the rotation velocity.

Interestingly, the circular velocity curves of our galaxies exhibit a smooth transition throughout the Hubble sequence, increasing their maximum values from late-types to early-types. The shape of  $V_c$  also changes in the same order: starting with slow-rising and flat profiles to the presence of a sharp and round peak in the central parts. This division provides a way to classify galaxies

based on their kinematics and dynamics. In the following, we argue whether we could link those observations to models of galaxy formation in order to build a “Dynamical evolutionary sequence” to put alongside with the “Dynamical classification” exposed in Section 4.6.2.

The hierarchical Lambda cold dark matter ( $\Lambda$ CDM) cosmology (Somerville & Primack 1999; Steinmetz & Navarro 2002), suggests that the first discs are formed by cooling of gas inside rotating dark matter haloes. Subsequently this gas forms stars that, losing angular momentum, organize themselves into a thick disc within the spinning dark matter halo. At this stage, the bulge is either absent or small. However, the thick disc, already formed, provides high random motions ( $V/\sigma \ll 1$ ). The star formation efficiency is low, and hence the dark matter fraction might be high (Moster et al. 2010). The circular velocity curves of these early systems might show a slowly rising shape due to the low-mass bulge. Those features are shown by the late-type Scd–Sd galaxies that might be considered as the youngest systems of our sample.

The gas will continue to collapse, forming a spheroidal region growing in mass and density. Thus, the rotational velocity and velocity dispersion of the galaxy are both expected to be high. Additionally, a thin disc starts to form having smaller scale length than the thick disc. The star formation efficiency is expected to increase, and hence the dark matter fraction decreases (Moster et al. 2010). The shape of the circular velocity might be flat, because the central part is not dense and massive enough to peak the profile. Therefore, flat rotation-curve galaxies may be considered as the second step in the galactic evolution.

Eventually photoionization or supernova feedback can stop the process of gas cooling and further formation of stars (Kannan et al. 2014; Moster et al. 2010). Then, to increase the mass of the galaxies and to trigger new processes, such as secular evolution, or minor and major mergers appear to be necessary.

At this stage, local/global instabilities of the disc due to secular evolution/minor mergers can drive the gas to the center and might form big bulges (Khochfar & Silk 2006) and maximal disks, which sharpen the rotation curve. Here, both ordered velocity and velocity dispersion are expected to be high.

Finally, to form giant elliptical galaxies with high random motions and low ordered-motions, major mergers are needed. The gas collapses fast and a large quantity of stars are formed (until AGN feedback stops the cooling of the gas and birth of new stars). In this case round-peaked rotation curves due to the spheroidal shape of the elliptical might feature those systems (since the bulge covers 100% of the disc) as we observe.

The proposed Dynamical evolution sequence of galaxies probably constitutes a scenario for the galaxy formation. However, merging can happen at any stage and therefore some dynamical classes might not be part of this picture.

The results from this thesis create new open questions in the field of galaxy dynamics and suggest a broader new direction for future studies. For example, ordered-over-random motion appears to be the key parameter of the kinematic, dynamic and dark matter study. If our dynamical classification of the galaxies has a global application, then from the observed  $V$ ,  $\sigma$  and  $V/\sigma$  profiles we can predict the shape of the rotation curves, galaxies' structural components proportion, dark matter content, and in general the complete mass distributions of the galaxies. The  $V/\sigma$  parameter might indirectly be used to trace the type of the dark matter halo and the merging history of the galaxies.

## FUTURE WORK

In a future research, we would like to expand our study on dynamical modeling using recent spectroscopic data of galaxies with complex mass distribution to explain their dynamical evolution, dark matter content and halo density profiles. We plan to investigate the stellar dynamics and total mass-to-light ratios of galaxies with **exotic morphologies**, such as the interacting galaxies of the CALIFA survey. Finally, we would like to construct the combined total circular velocity curves of the interacting galaxies from both **stellar kinematics** and **cold HI gas** to probe the types of **dark matter halo density profiles** further out from the galactic center.

## DARK MATTER IN GALAXIES WITH EXOTIC MORPHOLOGIES

Colliding galaxies are very common in galaxy clusters with high number densities. Large galaxies are formed by mergers and gravitational capture of smaller entities. Interactive galaxies are appropriate objects to study the dark matter outside the Hubble sequence. Strong evidence for its existence in the galaxies comes from the observations of their flat rotational curves. Dark matter has already been included in the dynamical simulations of Interacting galaxies (e., g. Gerhard 1981; Farouki & Shapiro 1982) to support the observed flat rotational curves, studying the mergers between equally-matched disk/halo galaxies. The current studies (Theis 2004) showed that shape and extension of the DM-halos have large effects on the behavior of interacting galaxies.

## STELLAR DYNAMICS AND TOTAL MASS-TO-LIGHT RATIO OF INTERACTING GALAXIES

In general, **interacting galaxies have very complex kinematics** of the ionized gas, which makes constructing reliable dynamical models out of it difficult. However, the galactic relaxation time

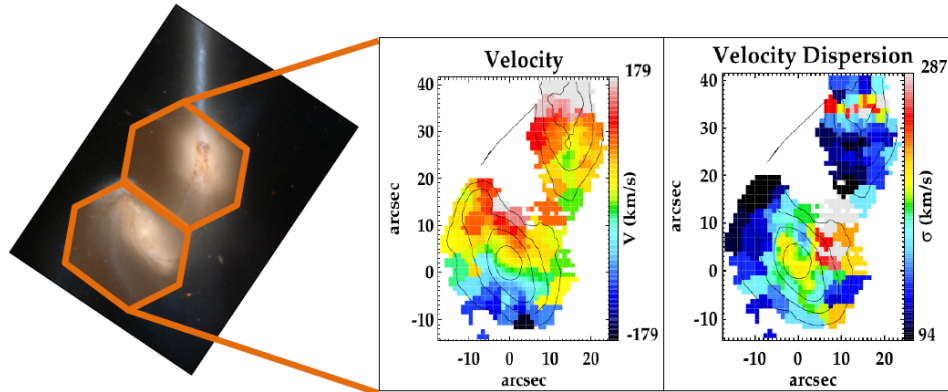


**Figure 5.1:** SDSS image of the interacting galaxy NGC 4676 (left panel) with the overplotted hexagonal ( $74'' \times 64''$ ) field of view offered by the PPAk fiber bundle of the CALIFA survey (Sánchez et al. 2012b). The interacting galaxies have very complex kinematics of the ionized gas, which does not allow one to construct reliable dynamical models. However, the galactic relaxation time is still many orders of magnitude longer than a Hubble time and the dynamics of the stars is well-described by the collisionless Boltzmann equation. Therefore, from the stellar mean velocity (middle panel) and velocity dispersion (right panel), one can apply the axisymmetric Jeans models to the stellar kinematics of the interacting galaxy in order to construct its second velocity moment map  $V_{RMS} = \sqrt{V^2 + \sigma^2}$  and to obtain the corresponding dark matter fraction.

is still many orders of magnitude longer than a Hubble time and the dynamics of the stars is well-described by the collisionless Boltzmann equation (Binney & Tremaine 1987). This would allow us to apply the axisymmetric Jeans models to the stellar kinematics of the interacting galaxies from the CALIFA survey in order to obtain their total (dynamical) mass-to-light ratio  $\Upsilon_{\text{tot}}$ . We will then compare  $\Upsilon_{\text{tot}}$  to the stellar mass-to-light ratio ( $\Upsilon_{\text{pop}}$ ) based on fitting stellar population models to multi-band photometry, available in the literature. We will **investigate if the fraction  $\Upsilon_{\text{tot}}/\Upsilon_{\text{pop}}$  of the Interacting galaxies differs from the fraction of the regular galaxies**, which will shed light on their initial mass-function (IMF) and evolutionary processes.

### DARK MATTER HALO DENSITY PROFILES OF INTERACTING GALAXIES

According to the cold dark matter (CDM) model, galaxies are surrounded by a dark matter (DM) halo (Springel et al. 2005; Boylan-Kolchin et al. 2008; Klypin et al. 2011). Navarro et al. (1997b) obtained the “universal” profile (hereafter NFW profile) of the DM halo from numerical simulations over a wide range of size and mass scales, covering the range from dwarf galaxies to rich clusters of galaxies. Current studies (Macciò et al. 2012) show that reasonable baryonic feedback is able to create a density core (not NFW) in the dark matter distribution even for massive spiral

galaxies with masses on the order of the Milky Way. Interacting galaxies are characterized by high rates of star formation and gas flows due to the collisional processes. Therefore, in most of the cases they have significant feedback from massive stars and/or supernova, which could provide an environment for core DM halo density distribution.

We would like to investigate the exact DM halo density profile (core or NFW) of the interacting galaxies. Some theories propose the existence of common DM halos (Fuentes-Carrera et al. 2003) that would require a new model of the DM halo density distribution we would like to investigate. First, we will apply the JAM model to the stellar kinematics of galaxies with integral-field spectroscopic data, extracting the total stellar mass distribution. The CALIFA survey (spatial resolution of  $\sim 2''$ ) encompasses a large sample of interacting galaxies with reliable stellar kinematics. Second, we will extract the circular motion of the cold HI from its gas kinematics obtaining the total gas mass distribution. Next, we will obtain the total circular velocity curve  $V_c$  that contains the contribution of the baryonic mass from both the stars and cold HI gas (Weijmans et al. 2008). Finally, we will obtain the best fit of the interacting galaxy DM halo density profiles (core, NFW, etc.) using the total circular velocity curve  $V_c$ . We will conclude whether most of the interacting galaxies hold a core DM halo density profile and if the type of the DM halo depends on the galactic evolution.

## CURRENT AND NEW IFU SURVEYS

Following the analysis in this thesis it is clear that many other topics remain open. The current and upcoming integral field surveys as VENGA (VIRUS-P Exploration of Nearby Galaxies, Blanc et al. 2010b), CALIFA (Sánchez et al. 2012b), SAMI (Sydney-AAO Multi-object Integral Field Spectrograph, Konstantopoulos et al. 2013) and MANGA (Mapping Nearby Galaxies, Law & MaNGA Team 2014), provide or will provide large statistical samples, large fields of view and better spatial resolutions. This will give the opportunity to investigate the mass distribution of galaxies from different morphological type and kinematics, to probe their dark matter halo profile at large radii, including a precise estimation of their mass in the centers and non-constant mass-to-light ratios in the outer parts. Our sample looks at the inner parts of the galaxies and therefore the mass modeling is limited at large radii. Eventually, these surveys will give the opportunity to probe the link between dynamical classification, evolution of galaxies and the type of the dark matter halos, as well as further perspectives on the galactic dynamics and formation theories.



## 5.1 ADC ASSUMPTIONS

To illustrate some of the assumptions adopted in the asymmetric drift correction (ADC) approach, we construct a (toy) galaxy model with parameters that are representative for our observed late-type spiral galaxies.

### 5.1.1 REPRESENTATIVE GALAXY MODEL

We place the galaxy model at a typical distance of  $\sim 20$  Mpc, so that  $1.0'' \simeq 0.1$  kpc. We adopt an exponential surface brightness profile  $I(R) \propto \exp(-R/h)$  with (radial) scale length  $h = 3.0$  kpc ( $30''$ ), which coincides approximately with the radial extent of our kinematic data. For the streaming motion, we use the power-law prescription (Evans & de Zeeuw 1994eq. 2.1) with a  $\beta = 0$  flat curve at infinity, with corresponding velocity  $v_\infty = 175$  km s $^{-1}$ , and  $R_c = 1.5$  kpc ( $15''$ ) for the core radius. Finally, for the (intrinsic) radial velocity dispersion, we assume an exponential profile  $\sigma_R^2 = \sigma_1^2 \exp(-R/R_1)$ , with  $\sigma_1 = 100$  km s $^{-1}$  and scale radius  $R_1 = 4.0$  kpc ( $40''$ ).

The latter exponential choice is motivated as follows. In case of a locally isothermal disc, the square of the vertical velocity dispersion is proportional to the mass surface density:  $\sigma_z^2 \propto \Sigma$ . Moreover, the flattening of the velocity ellipsoid in the vertical direction,  $\sigma_z/\sigma_R$ , is approximately constant in the discs of spiral galaxies (see Bottema 1993). For an exponential surface brightness

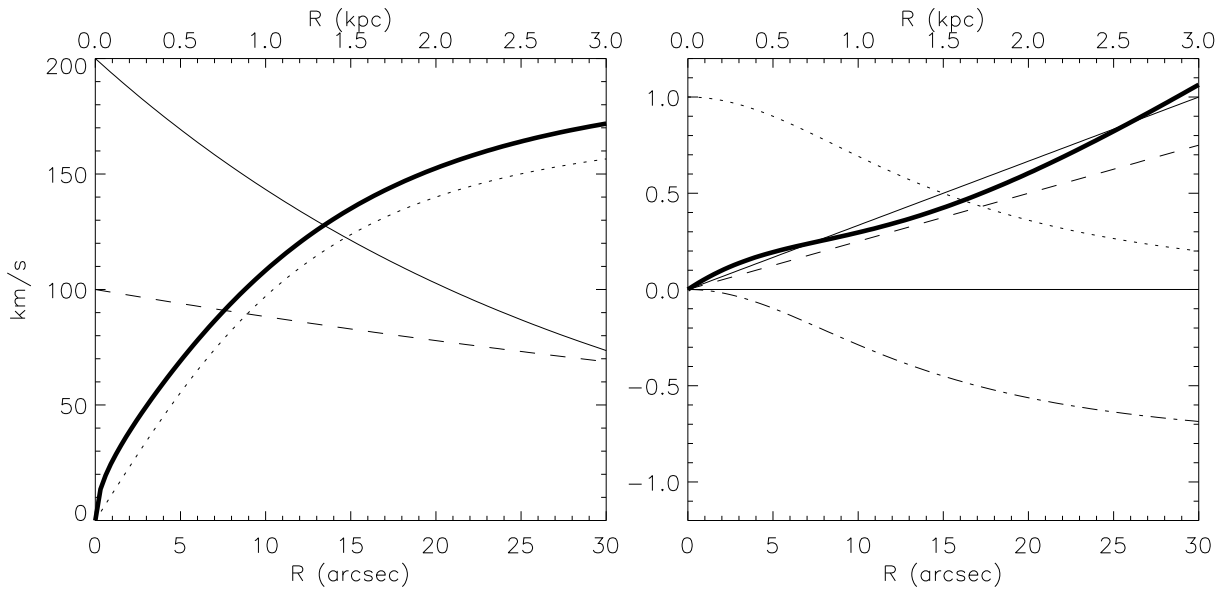


**Figure 5.2:** Properties of a representative galaxy model as function of meridional plane radius  $R$  in kpc (and in arcsec at the top for a distance  $\sim 20$  Mpc). The left panel shows the radial profiles of the (arbitrarily normalised) surface brightness  $I$  (thin solid), the streaming motion  $\bar{v}_\phi$  (thin dotted) and the radial velocity dispersion  $\sigma_R$  (thin dashed). The thick solid curve is the circular velocity  $v_c$  from equation (2.6), with (default) parameters  $q_\Phi = 1.0$  and  $\kappa = 0.5$ . The right panel shows the profile of  $\alpha_R$  (dotted), as well as the various components that contribute to the asymmetric drift correction:  $d \ln I / d \ln R$  (solid),  $d \ln \sigma_R^2 / d \ln R$  (dashed) and the last term (dash-dotted) within curled brackets in equation (2.6). The sum of all components is indicated by the thick solid curve.

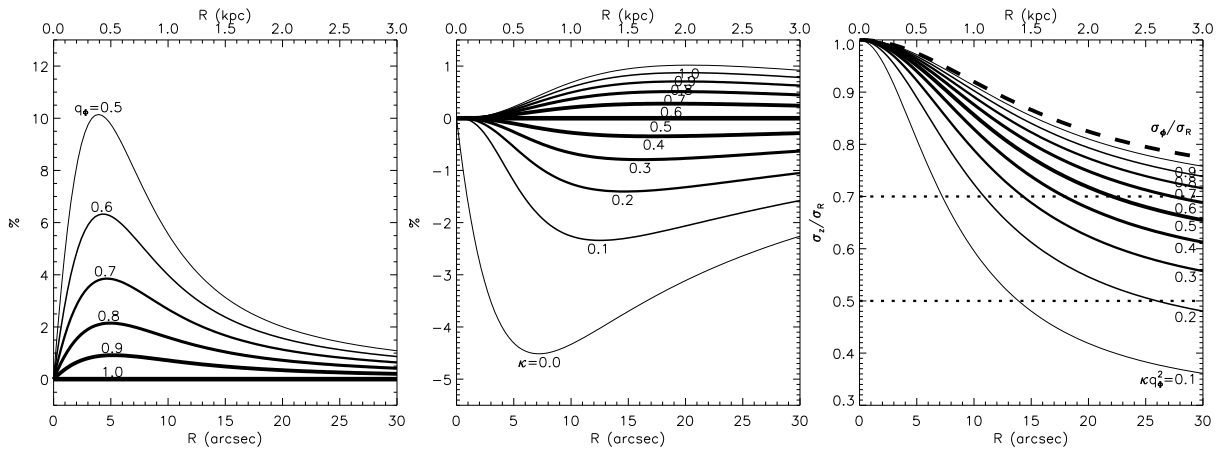


**Figure 5.3:** Variation in the circular velocity  $v_c$  of a representative galaxy model due to changes in the parameters  $q_\phi$  (left panel) and  $\kappa$  (middle panel). The decreasing thickness of the curves corresponds to increasing flattening of the potential, linearly from default  $q_\phi = 1.0$  (spherical) to 0.5, in steps of 0.1. Similarly, the alignment of the velocity ellipsoid, changes linearly from default  $\kappa = 0.5$  up to 1.0 (upper curves) and down to 0.0 (lower curves), in steps of 0.1. In the right panel, the thick dashed curve shows  $\sigma_\phi/\sigma_R$  (assuming the velocity ellipsoid is symmetric around  $v_\phi = \overline{v_\phi}$ ). The thick solid curves shows  $\sigma_z/\sigma_R$  with default  $\kappa q_\phi^2 = 0.5$ , which for the thin solid curves increases up to 0.9 (upper curves) and decreases down to 0.1 (lower curves), linearly in steps of 0.1. The horizontal dotted lines bracket the range estimated from long-slit kinematic observations (see § 5.1.3 for details).

profile and constant mass-to-light ratio, we thus expect

$$\sigma_R^2 \propto \sigma_z^2 \propto I(R) \propto \exp(-R/h), \quad (5.1)$$

to be representative.

In the left panel of Fig. 5.2 we show for the galaxy model the radial profiles of the adopted surface brightness  $I$  (thin solid curve), streaming motion  $\overline{v_\phi}$  (dotted curve) and radial velocity dispersion  $\sigma_R$  (dashed curve). The right panel shows the various contributions to the asymmetric drift correction in equation (2.6), resulting in the circular velocity  $v_c$  in the left panel (thick solid curve) for (default) parameters  $q_\phi = 1$  and  $\kappa = 1/2$ . Fig. 5.3 indicates the effect of changing these parameters, on  $v_c$  (left and middle panel) and on  $\sigma_z/\sigma_R$  (right panel), as discussed in more detail next.

### 5.1.2 POWER-LAW STREAMING MOTION

Although, in general the 'power-law' prescription in (Evans & de Zeeuw 1994eq. 2.1) does not have to be representative of the true streaming motion, it provides often a remarkably good fit to observed velocities as shown in Figures 3.7,3.8 and Figures 3.9, 3.10 (see Weijmans et al. 2008). Even so, we in principle only use this prescription to obtain an expression for the derivative of  $\overline{v_\phi}$  in the vertical direction,  $\alpha_z$  (see Section 2.5.3), which is observationally (nearly) inaccessible. The resulting expression for  $\alpha_z$  is independent of the asymptotic slope  $\beta$  (which we assume flat in the fits), and besides  $\alpha_R$  (from the observed velocity) only involves the (average) flattening of the potential  $q_\phi$ .

Even though the density distribution of most galaxies is flattened, the potential is much rounder. For example, an axisymmetric logarithmic potential is only about a third as flattened as the corresponding density distribution (Binney & Tremaine 1987). Moreover, the potential traces the total mass density, including possible dark matter, which can be significant rounder than the both the bulge and disc. Even so, the dependence of the circular velocity on  $q_\phi$  is only weak, as we show for the representative galaxy model in the left panel of Fig. 5.3. Here,  $v_c$  decreases at most by  $\sim 10\%$ , when we vary  $q_\phi$  from the adopted value of 1.0 (spherical potential) to 0.5.

### 5.1.3 SHAPE OF THE VELOCITY ELLIPSOID

For the cross term  $\overline{v_R v_z}$  in Eq. (2.5), which depends on the alignment of the velocity ellipsoid in the meridional plane, we adopt the functional form

$$\overline{v_R v_z} = \kappa (\sigma_R^2 - \sigma_z^2) \frac{(z/R)}{1 - (z/R)^2}, \quad (5.2)$$

so that the limits  $\kappa = 0$  and  $\kappa = 1$  correspond to alignment with the cylindrical and spherical coordinate system, respectively.

Substituting the expression for  $\alpha_z = -(1 - \alpha_R)z^2/q_\Phi^2 R^2$  in Eq. (5.2), we get

$$\frac{\sigma_z^2}{\sigma_R^2} = \frac{\kappa q_\Phi^2 (1 + \alpha_R)}{\kappa q_\Phi^2 (1 + \alpha_R) + (1 - \alpha_R)}. \quad (5.3)$$

Given  $\alpha_R$  from the observed velocity and a choice of  $q_\Phi$ , this means that the factor  $\kappa$ , which determines the alignment of the velocity ellipsoid, (in the meridional plane) is coupled to the flattening of the velocity ellipsoid (in the equatorial plane). The radial profile of  $\sigma_z/\sigma_R$  is shown in the right panel of Fig. 5.3 for a representative  $\alpha_R$  from the above galaxy model. The thickest solid curve is for  $\kappa q_\Phi^2 = 0.5$ , i.e., for the adopted values of  $q_\Phi = 1$  and  $\kappa = 0.5$ , while the upper (lower) curves are for increasing (decreasing) values of  $\kappa q_\Phi^2$ .

As mentioned in Section 3.6.1, this 'vertical velocity anisotropy' has been estimated from (long-slit) stellar velocity dispersion measurements for a few spiral galaxies at intermediate inclination (Gerssen et al. 1997, 2000; Shapiro et al. 2003), and predicted from simple isothermal thin-disc models applied to stellar kinematics of (nearly) edge-on spiral galaxies (Bottema 1993; Kregel et al. 2005). The results are consistent, yielding a range of  $\sigma_z/\sigma_R \simeq 0.6 \pm 0.1$ , indicated by the dotted vertical lines in the right panel of Fig. 5.3.

These studies assume a constant  $\sigma_z/\sigma_R$  with radius, whereas from equation (5.3) we expect a (mild) decline with radius, as long as  $\kappa q_\Phi^2$  remains approximately constant. This is because  $\alpha_R$  decreases from unity to zero, corresponding to a 'rotation curve' that goes from linearly increasing in the centre to becoming flat at larger radii. On the other hand, in these studies most of the observational constraints on  $\sigma_z/\sigma_R$  come from radii where the rotation curve is indeed flat. We see from the right panel of Fig. 5.3 that at larger radii, the profiles of  $\sigma_z/\sigma_R$  around the adopted one with  $\kappa q_\Phi^2 = 0.5$ , nicely stay within the 'observed' range. Specifically, for  $\alpha_R = 0$ , the adopted values  $q_\Phi = 1$  and  $\kappa = 0.5$  imply  $\sigma_z/\sigma_R = 0.56$ . The other way around, the 'observed' range in  $\sigma_z/\sigma_R$  from 0.5 to 0.7 corresponds to  $\kappa q_\Phi^2$  from 0.33 to 0.96. In any case, from the middle panel of Fig. 5.3, we expect within the latter range of  $\kappa$  (with  $q_\Phi = 1$ ) that on average  $v_c$  only changes by  $\lesssim 1\%$ .

As in (nearly) all previous studies we assume that the velocity ellipsoid is symmetric around  $v_\phi = \bar{v}_\phi$ . The shape of the velocity ellipsoid in the equatorial plane  $\sigma_\phi/\sigma_R$  then only depends on the 'radial' slope  $\alpha_R$  of the streaming motion<sup>1</sup>. As shown by the dashed curve in the right panel of Fig. 5.3, in this case we expect  $\sigma_\phi/\sigma_R$  to decrease from unity in the centre to  $\sqrt{1/2} \simeq 0.71$  at large radii.

From equation (3.4), we see that at each radius  $R$ , the contribution of  $\sigma_R$  and  $\sigma_\phi$  to the observed

<sup>1</sup>The logarithmic slope of the circular velocity as sometimes assumed.

velocity dispersion  $\sigma$  depends on the azimuthal angle  $\phi$ , while that of  $\sigma_z$  is constant (for given inclination). In particular, if we observe  $\sigma_{\text{maj}}$  and  $\sigma_{\text{min}}$  along respectively the projected major axis  $x' = R$  and projected minor axis  $y' = R \cos i$ , we find that the 'skewness' of the velocity ellipsoid follows from

$$\frac{\overline{(v_\phi - \bar{v}_\phi)^3}}{2\sigma_R^2 \bar{v}_\phi} = \frac{1}{2}(1 + \alpha_R) + \left(1 - \frac{\sigma_{\text{maj}}^2}{\sigma_{\text{min}}^2}\right) \left(1 + \frac{\sigma_z^2 \cos^2 i}{\sigma_R^2 \sin^2 i}\right), \quad (5.4)$$

where  $\sigma_z/\sigma_R$  follows from equation (5.3) above. Unfortunately, our stellar velocity dispersion maps are not accurate enough (due to insufficient spectral resolution and dust obscuration) to estimate the possible asymmetry of the velocity ellipsoid around  $v_\phi = \bar{v}_\phi$ .

Alternatively, we may assume a plausible distribution function (DF) and compute the 'skewness' directly. However, in general it is (very) difficult to find such a DF that also simultaneously satisfies all observational constraints. For example, [Kuijken & Gilmore \(1991\)](#) construct such DF for the Milky Way, but find that the predicted value of  $\sigma_z/\sigma_R$  is too low compared to the measured value of  $0.53 \pm 0.07$  ([Dehnen & Binney 1998](#); [Mignard 2000](#)).

## 5.2 MULTI-GAUSSIAN EXPANSION TABLES

On the smooth light models of the 26 E–Sd galaxies, we applied the multi-Gaussian expansion method to parameterize the observed surface brightness  $I(x', y')$  by a sum of  $N$  Gaussian components,

$$I(x', y') = \sum_{j=0}^N I_{0,j} \exp \left\{ -\frac{1}{2\sigma_j'^2} \left[ x'^2 + \frac{y'^2}{q_j'^2} \right] \right\}. \quad (5.5)$$

Each component has three parameters: the central surface brightness  $I_{0,j}$  ( $L_\odot pc^{-2}$ ), the dispersion  $\sigma_j'$  along the major  $x'$ -axis (in arcsec), and the flattening  $q_j'$ . These values are presented in the following tables:

CALIFA		
NGC0776		
$I_0$	$\sigma_{maj}$	$q_p$
L/pc <sup>2</sup>	arcsec	
5144.87	0.386100	0.51
1771.35	1.34006	1.00
237.682	3.20061	0.90
129.998	11.6842	0.46
64.5480	22.8751	1.00
NGC1167		
$I_0$	$\sigma_{maj}$	$q_p$
L/pc <sup>2</sup>	arcsec	
3401.11	0.641045	1.00
1284.02	2.12300	0.94
409.845	5.65947	0.88
108.934	15.7529	0.82
45.0308	44.3080	0.80
NGC5966		
$I_0$	$\sigma_{maj}$	$q_p$
L/pc <sup>2</sup>	arcsec	
9865.33	0.412814	0.62
1876.53	1.59101	0.79
536.913	4.70579	0.68
202.925	11.3455	0.62
48.0580	30.3827	0.74
NGC6125		
$I_0$	$\sigma_{maj}$	$q_p$
L/pc <sup>2</sup>	arcsec	
7425.77	0.649860	0.84
2757.21	1.63927	0.96
975.311	3.98309	0.97
187.228	11.4305	0.94
51.6799	29.3074	0.97

<b>NGC6411</b>		
$I_0$	$\sigma_{maj}$	$q_p$
L/pc <sup>2</sup>	arcsec	
22550.4	0.386100	0.62
2243.95	1.66093	0.72
812.122	4.45579	0.71
271.385	11.7075	0.70
62.5315	36.8964	0.63
<b>IC1683</b>		
$I_0$	$\sigma_{maj}$	$q_p$
L/pc <sup>2</sup>	arcsec	
3669.18	0.386100	0.77
2517.98	0.815606	0.66
580.464	1.37138	0.67
280.939	2.76811	0.43
208.311	8.61082	0.63
65.3589	18.8436	0.44
<b>NGC0001</b>		
$I_0$	$\sigma_{maj}$	$q_p$
L/pc <sup>2</sup>	arcsec	
13633.6	0.386100	0.55
2628.96	1.12639	0.98
755.809	2.98976	0.84
215.818	7.76497	0.86
51.7125	23.5421	0.65
<b>NGC0036</b>		
$I_0$	$\sigma_{maj}$	$q_p$
L/pc <sup>2</sup>	arcsec	
12837.7	0.386100	0.45
745.508	1.61565	0.78
354.096	3.54319	1.00
115.945	12.0081	0.81
41.1454	27.6639	0.81

SAURON		
NGC488		
$I_0$	$\sigma_{maj}$	$q_p$
L/pc <sup>2</sup>	arcsec	
24161.1	0.379487	1.00
16980.5	0.100000	0.90
14945.1	0.229639	0.90
12930.5	0.455221	0.90
10798.0	0.840047	0.90
8245.04	1.48429	0.90
5595.02	2.52935	0.90
3318.18	4.16837	0.90
1694.88	6.65835	0.90
734.894	10.3317	0.90
266.760	15.6081	0.90
79.9548	23.0174	0.90
19.4387	33.2535	0.90
3.72155	47.2815	0.90
0.534507	66.5092	0.90
0.0534290	93.1119	0.90
0.00326282	130.936	0.90
8.91710e-05	189.043	0.90
4.75880e-08	307.694	0.90
1.93613e-07	323.268	0.90
30.4184	0.692449	0.77
84.0009	2.86532	0.77
176.598	8.01318	0.77
287.490	17.8046	0.77
340.678	33.2894	0.77
267.029	54.3381	0.77
125.559	80.1382	0.77
31.5344	110.269	0.77
3.37897	145.586	0.77
0.0869407	189.762	0.77

NGC628		
$I_0$	$\sigma_{maj}$	$q_p$
L/pc <sup>2</sup>	arcsec	
32854.4	0.162448	1.00
125.782	0.100728	0.95
225.980	0.242207	0.95
374.317	0.523082	0.95
564.486	1.03724	0.95
758.446	1.90804	0.95
876.392	3.27384	0.95
831.858	5.26280	0.95
616.017	7.97434	0.95
336.156	11.4870	0.95
125.584	15.8877	0.95
28.9493	21.2922	0.95
3.58537	27.8429	0.95
0.200084	35.7110	0.95
0.00399263	45.1215	0.95
2.05845e-05	56.3965	0.95
1.70177e-08	70.0022	0.95
1.12294e-12	86.5841	0.95
4.80382e-27	489.198	0.95
9.90921	0.567729	0.81
28.1312	2.32220	0.81
63.3584	6.67239	0.81
117.059	15.5591	0.81
173.223	30.9861	0.81
190.871	54.1050	0.81
143.022	84.8694	0.81
65.2218	123.148	0.81
14.5351	170.510	0.81
0.890928	232.944	0.81

NGC772		
$I_0$	$\sigma_{maj}$	$q_p$
L/pc <sup>2</sup>	arcsec	
96530.9	0.323785	1.00
11343.6	0.100000	0.83
8973.63	0.231649	0.83
7132.09	0.459679	0.83
5671.02	0.846972	0.83
4271.96	1.50079	0.83
2958.77	2.58269	0.83
1857.68	4.32888	0.83
1046.19	7.07829	0.83
523.087	11.3058	0.83
229.915	17.6598	0.83
88.0309	27.0071	0.83
29.1180	40.5002	0.83
8.23669	59.7335	0.83
1.95057	87.1689	0.83
0.365980	127.320	0.83
0.0470251	190.417	0.83
0.00266180	307.883	0.83
3.24587e-06	587.780	0.83
20.9777	0.647263	0.66
58.4499	2.67009	0.66
125.531	7.52827	0.66
212.585	16.9770	0.66
268.284	32.3401	0.66
228.939	53.7768	0.66
119.176	80.5657	0.66
33.5965	112.231	0.66
4.11365	149.606	0.66
0.124326	196.620	0.66

NGC864		
$I_0$	$\sigma_{maj}$	$q_p$
L/pc <sup>2</sup>	arcsec	
834.177	1.90394	1.00
26446.2	0.100000	0.95
12341.5	0.222975	0.95
6151.01	0.413665	0.95
3110.85	0.715851	0.95
1406.19	1.21152	0.95
526.613	2.02067	0.95
160.131	3.31228	0.95
38.7765	5.33337	0.95
7.30361	8.43184	0.95
1.05188	13.0750	0.95
0.114532	19.8688	0.95
0.00938373	29.5636	0.95
0.000581376	43.0392	0.95
2.75913e-05	61.3164	0.95
9.94468e-07	85.8935	0.95
2.36983e-08	120.155	0.95
2.37742e-10	173.333	0.95
7.82690e-14	303.662	0.95
4.47863e-15	588.145	0.95
49.8034	0.765973	0.68
137.002	3.23021	0.68
265.666	8.90197	0.68
352.744	18.9248	0.68
287.206	33.2980	0.68
128.139	51.1065	0.68
28.5955	71.4334	0.68
2.84957	93.9640	0.68
0.0999143	119.255	0.68
0.000663265	149.532	0.68

NGC1042		
$I_0$	$\sigma_{maj}$	$q_p$
L/pc <sup>2</sup>	arcsec	
29277.5	0.225435	1.00
23.4874	0.110375	0.95
54.3990	0.261989	0.95
111.359	0.540496	0.95
200.801	0.998301	0.95
305.636	1.66752	0.95
361.532	2.53343	0.95
301.093	3.53820	0.95
162.476	4.62167	0.95
51.7188	5.76355	0.95
7.95007	6.97769	0.95
0.149559	7.97398	0.95
0.319706	8.36578	0.95
0.00448162	9.78088	0.95
4.42727e-06	11.4406	0.95
5.59134e-21	23.7012	0.95
2.43918e-25	77.5327	0.95
5.19700	0.603112	0.71
14.7382	2.49900	0.71
32.4085	7.13229	0.71
57.2462	16.3648	0.71
77.6200	31.8271	0.71
73.9129	54.0421	0.71
44.7778	82.4533	0.71
15.3972	116.628	0.71
2.41452	157.630	0.71
0.0978087	210.096	0.71

NGC2805		
$I_0$	$\sigma_{maj}$	$q_p$
L/pc <sup>2</sup>	arcsec	
12769.8	0.118577	1.00
96.3980	0.100000	0.80
134.251	0.237574	0.80
177.193	0.507706	0.80
213.890	1.00832	0.80
229.573	1.87997	0.80
212.939	3.30796	0.80
165.324	5.51611	0.80
103.930	8.75357	0.80
51.2172	13.2826	0.80
19.1686	19.3841	0.80
5.23762	27.3977	0.80
0.982865	37.7820	0.80
0.115772	51.1542	0.80
0.00760520	68.3166	0.80
0.000239083	90.3358	0.80
2.87226e-06	118.840	0.80
8.16283e-09	157.495	0.80
1.16820e-15	560.319	0.80
7.58880e-17	588.145	0.80
2.97383	0.618881	0.76
8.34783	2.55054	0.76
18.2898	7.24864	0.76
31.8804	16.5775	0.76
41.7488	32.0219	0.76
37.5706	53.8773	0.76
21.0198	81.4733	0.76
6.51151	114.326	0.76
0.898087	153.370	0.76
0.0312727	202.871	0.76

NGC2964		
$I_0$	$\sigma_{maj}$	$q_p$
L/pc <sup>2</sup>	arcsec	
78000.0	0.196710	1.00
2617.84	0.100000	0.95
4856.21	0.203529	0.95
7703.26	0.346765	0.95
10286.1	0.528236	0.95
10381.2	0.741877	0.95
6767.80	0.977947	0.95
2380.00	1.22640	0.95
379.756	1.47897	0.95
23.9956	1.72954	0.95
0.535075	1.97749	0.95
0.00271667	2.23729	0.95
1.17448e-06	2.52394	0.95
5.64675e-28	17.7617	0.95
343.248	0.999484	0.55
847.417	4.12719	0.55
1253.73	10.5231	0.55
996.241	20.1928	0.55
374.578	32.2402	0.55
61.2272	45.7852	0.55
4.03948	60.3928	0.55
0.0922878	76.1353	0.55
0.000510860	93.5743	0.55
3.02412e-07	114.061	0.55

NGC3346		
$I_0$	$\sigma_{maj}$	$q_p$
L/pc <sup>2</sup>	arcsec	
8592.16	0.117764	1.00
5.51674	0.100000	0.75
12.9259	0.208550	0.75
23.8059	0.364702	0.75
52.0977	0.585304	0.75
127.032	0.951958	0.75
257.570	1.46913	0.75
358.462	2.04420	0.75
266.261	2.58562	0.75
81.5607	3.06420	0.75
7.85732	3.48843	0.75
0.165698	3.87620	0.75
0.000417065	4.24755	0.75
4.61527e-27	30.8663	0.75
20.0281	1.11722	0.84
54.8215	4.86336	0.84
102.722	13.3917	0.84
125.357	28.0738	0.84
88.3988	48.4973	0.84
32.2569	73.2196	0.84
5.54370	101.153	0.84
0.381378	132.444	0.84
0.00645749	169.723	0.84
5.59180e-09	588.145	0.84

NGC3423		
$I_0$	$\sigma_{maj}$	$q_p$
L/pc <sup>2</sup>	arcsec	
13792.7	0.122759	1.00
123.675	0.100000	0.87
180.255	0.229912	0.87
250.354	0.468852	0.87
322.260	0.886519	0.87
372.270	1.57506	0.87
374.591	2.64297	0.87
317.685	4.20366	0.87
219.509	6.35935	0.87
119.930	9.18498	0.87
50.9526	12.7278	0.87
16.6610	17.0800	0.87
3.89080	22.5135	0.87
0.546012	29.4395	0.87
0.0382586	38.2542	0.87
0.00111557	49.3528	0.87
1.07896e-05	63.2343	0.87
2.47404e-08	80.6561	0.87
6.96086e-12	103.251	0.87
8.71787e-25	588.145	0.87
20.0696	1.08784	0.77
55.3163	4.73887	0.77
105.741	13.1254	0.77
134.744	27.7765	0.77
101.826	48.4840	0.77
40.7383	73.8467	0.77
7.84745	102.700	0.77
0.622501	135.133	0.77
0.0127447	173.882	0.77
2.50706e-08	588.145	0.77

NGC3949		
$I_0$	$\sigma_{maj}$	$q_p$
L/pc <sup>2</sup>	arcsec	
33147.0	0.117549	1.00
247.937	0.100000	0.70
415.669	0.224872	0.70
648.526	0.445563	0.70
915.744	0.811084	0.70
1122.66	1.37307	0.70
1141.20	2.17487	0.70
911.230	3.24702	0.70
534.216	4.61299	0.70
209.626	6.29826	0.70
48.6101	8.33288	0.70
5.69204	10.7510	0.70
0.275836	13.5965	0.70
0.00422451	16.9350	0.70
1.37961e-05	20.8693	0.70
5.38056e-09	25.5418	0.70
1.33772e-13	31.0183	0.70
8.26695e-31	190.196	0.70
255.386	1.02019	0.64
619.844	4.18955	0.64
886.676	10.5806	0.64
663.271	20.1236	0.64
227.576	31.9031	0.64
32.9462	45.0697	0.64
1.86959	59.2178	0.64
0.0355133	74.4355	0.64
0.000155128	91.2871	0.64
6.65842e-08	111.070	0.64

NGC4030		
$I_0$	$\sigma_{maj}$	$q_p$
L/pc <sup>2</sup>	arcsec	
48113.1	0.132673	1.00
6683.20	0.100000	0.85
6306.38	0.227580	0.85
5769.43	0.438836	0.85
5280.87	0.774118	0.85
4689.75	1.30304	0.85
3905.92	2.12728	0.85
2987.56	3.38532	0.85
2069.12	5.26083	0.85
1282.12	7.99280	0.85
702.743	11.8898	0.85
336.428	17.3566	0.85
138.185	24.9419	0.85
47.3918	35.4081	0.85
13.0706	49.8181	0.85
2.76458	69.6535	0.85
0.422491	97.0337	0.85
0.0428413	135.256	0.85
0.00245804	190.513	0.85
5.11449e-05	279.530	0.85
94.5874	0.792567	0.76
257.160	3.31880	0.76
490.145	9.09118	0.76
622.904	19.1448	0.76
471.994	33.3173	0.76
190.981	50.6405	0.76
37.7912	70.2410	0.76
3.26045	91.8574	0.76
0.0959369	116.043	0.76
0.000511032	144.891	0.76

NGC4102		
$I_0$	$\sigma_{maj}$	$q_p$
L/pc <sup>2</sup>	arcsec	
0.00000	1.51675	1.00
780479.	0.100000	0.80
430239.	0.226887	0.80
225994.	0.440837	0.80
105796.	0.794823	0.80
41165.9	1.36520	0.80
12914.9	2.25180	0.80
3209.39	3.58225	0.80
623.145	5.51522	0.80
93.5110	8.24291	0.80
10.7426	11.9978	0.80
0.929351	17.0778	0.80
0.0583541	23.8971	0.80
0.00249597	33.0476	0.80
6.69346e-05	45.3535	0.80
1.02441e-06	61.9366	0.80
8.01166e-09	84.3564	0.80
2.71410e-11	115.032	0.80
2.61335e-14	159.316	0.80
2.76672e-20	317.404	0.80
417.543	0.994193	0.56
1034.48	4.10798	0.56
1546.11	10.4974	0.56
1252.87	20.1999	0.56
484.597	32.3341	0.56
82.0881	46.0066	0.56
5.65901	60.7653	0.56
0.136634	76.6745	0.56
0.000812731	94.2986	0.56
5.30141e-07	115.010	0.56

NGC4254		
$I_0$	$\sigma_{maj}$	$q_p$
L/pc <sup>2</sup>	arcsec	
55276.7	0.214221	1.00
2360.27	0.100000	0.90
2650.37	0.233512	0.90
2884.28	0.482931	0.90
2932.75	0.932225	0.90
2689.19	1.70569	0.90
2177.31	2.97412	0.90
1527.83	4.96009	0.90
912.721	7.93882	0.90
456.199	12.2341	0.90
187.781	18.2019	0.90
63.0606	26.1995	0.90
17.3132	36.5978	0.90
3.86202	50.0313	0.90
0.644074	67.8690	0.90
0.0681569	92.3699	0.90
0.00372418	127.134	0.90
6.80162e-05	180.772	0.90
4.11136e-09	588.145	0.90
41.7816	0.666318	0.73
116.763	2.76838	0.73
247.553	7.80158	0.73
402.276	17.4427	0.73
465.561	32.7082	0.73
345.322	53.3655	0.73
148.269	78.4943	0.73
32.8698	107.567	0.73
3.02333	141.295	0.73
0.0650717	183.067	0.73

NGC4487		
$I_0$	$\sigma_{maj}$	$q_p$
L/pc <sup>2</sup>	arcsec	
29433.2	0.165082	1.00
128.292	0.112584	0.60
205.535	0.292928	0.60
289.403	0.673927	0.60
350.123	1.39815	0.60
338.214	2.63211	0.60
256.844	4.48080	0.60
154.946	6.98504	0.60
79.4202	10.3593	0.60
27.0033	14.9615	0.60
6.25964	20.8722	0.60
0.820399	28.6377	0.60
0.0541719	38.4246	0.60
0.00165814	50.5337	0.60
1.93090e-05	65.5090	0.60
6.24197e-08	84.2494	0.60
2.94771e-11	108.714	0.60
7.07961e-23	588.145	0.60
21.1661	1.08232	0.63
58.3548	4.71134	0.63
111.869	13.0577	0.63
143.326	27.6705	0.63
109.166	48.3613	0.63
44.1688	73.7178	0.63
8.65970	102.536	0.63
0.711274	134.829	0.63
0.0157054	173.290	0.63
4.05190e-08	588.145	0.63

NGC4775		
$I_0$	$\sigma_{maj}$	$q_p$
L/pc <sup>2</sup>	arcsec	
21385.2	0.124139	1.00
85.9422	0.123094	0.83
104.353	0.282609	0.83
70.8265	0.428213	0.83
137.729	0.648835	0.83
156.922	0.983124	0.83
206.294	1.48964	0.83
231.293	2.25713	0.83
231.400	3.42004	0.83
176.995	5.18210	0.83
86.6828	7.85199	0.83
18.6892	11.8974	0.83
0.957515	18.0272	0.83
0.00329265	27.3151	0.83
9.24867e-08	41.3882	0.83
4.44062e-16	62.7120	0.83
1.60312e-33	330.558	0.83
50.9787	0.921593	0.87
131.086	3.82851	0.87
216.630	10.0446	0.87
209.753	19.9602	0.87
104.720	32.8503	0.87
24.4608	47.7321	0.87
2.47746	64.0000	0.87
0.0955427	81.6159	0.87
0.00103602	101.137	0.87
1.51587e-06	124.136	0.87

NGC5585		
$I_0$	$\sigma_{maj}$	$q_p$
L/pc <sup>2</sup>	arcsec	
5628.53	0.273743	1.00
4.28034	0.123094	0.80
8.10928	0.282609	0.80
1.55002	0.428213	0.80
18.2717	0.648835	0.80
5.84072	0.983124	0.80
38.1377	1.48964	0.80
23.6071	2.25713	0.80
72.0216	3.42004	0.80
70.4650	5.18210	0.80
112.156	7.85199	0.80
95.4806	11.8974	0.80
45.3761	18.0272	0.80
3.29264	27.3151	0.80
0.00218430	41.3882	0.80
2.05312e-11	62.7120	0.80
5.74238e-30	330.558	0.80
3.21709	0.591974	0.64
9.09807	2.43075	0.64
20.2298	6.95518	0.64
36.2837	16.0602	0.64
50.5433	31.4870	0.64
50.2132	53.9351	0.64
32.2378	82.9654	0.64
11.9305	118.182	0.64
2.04626	160.725	0.64
0.0921618	215.519	0.64

NGC5668		
$I_0$	$\sigma_{maj}$	$q_p$
L/pc <sup>2</sup>	arcsec	
10359.2	0.119730	1.00
86.9484	0.100000	0.80
126.047	0.237680	0.80
173.703	0.509145	0.80
220.000	1.01368	0.80
249.903	1.89395	0.80
247.841	3.33890	0.80
207.787	5.57667	0.80
142.255	8.85864	0.80
76.8615	13.4452	0.80
31.6726	19.6113	0.80
9.54045	27.6862	0.80
1.97044	38.1101	0.80
0.254297	51.4679	0.80
0.0181732	68.5049	0.80
0.000616560	90.1850	0.80
7.98818e-06	117.921	0.80
2.55423e-08	154.806	0.80
4.08927e-15	588.145	0.80
10.1447	0.748824	0.85
27.9426	3.12987	0.85
55.5687	8.68316	0.85
77.0558	18.6757	0.85
67.3458	33.2674	0.85
33.1058	51.6073	0.85
8.34376	72.7273	0.85
0.964738	96.2633	0.85
0.0405347	122.792	0.85
0.000336888	154.699	0.85

NGC5678		
$I_0$	$\sigma_{maj}$	$q_p$
L/pc <sup>2</sup>	arcsec	
34754.5	0.316706	1.00
25905.1	0.100000	0.80
17168.6	0.222086	0.80
12031.9	0.415340	0.80
8529.89	0.758518	0.80
4679.15	1.38871	0.80
1949.35	2.46579	0.80
629.794	4.19844	0.80
156.649	6.86295	0.80
29.6078	10.8051	0.80
4.20867	16.4380	0.80
0.446915	24.2437	0.80
0.0351698	34.7965	0.80
0.00201145	48.8200	0.80
8.10467e-05	67.2019	0.80
2.27355e-06	90.8343	0.80
4.45396e-08	121.040	0.80
3.92066e-10	164.610	0.80
1.73057e-14	309.025	0.80
1.59105e-15	588.145	0.80
168.114	0.890927	0.53
439.461	3.72212	0.53
749.057	9.86524	0.53
769.257	19.8315	0.53
418.841	32.9859	0.53
109.353	48.3167	0.53
12.6780	65.1673	0.53
0.574821	83.4665	0.53
0.00763208	103.765	0.53
1.45925e-05	127.714	0.53

## ACKNOWLEDGEMENTS

I would like to thank my supervisor Glenn van de Ven for his great contribution to my scientific career development. I learned a lot from my work with him, ranging from the sophisticated IDL coding to the deep analysis of scientific problems. Hiring me, he made real a big dream of mine – to study Dark Matter problems on galactic scales. I am glad that I was part of his group, where the knowledge flow and the relationships were friendly. I hope we will continue working together in the future.

There is one other person, without whom this thesis would not have been possible - Mariya Lyubenova, my co-advisor and guide. She showed me how to go deep within my results and how to search and see more details in their interpretation. She is an example of an astronomer with a great enthusiasm and original ideas.

I would like to thank Dr. Thorsten Lisker and Prof. Dr. Hans-Walter for being my thesis committee and giving useful suggestions. Many thanks to Dr. Glenn van de Ven and Prof. Dr. Luca Amendola for being the referees of my thesis, and Prof. Dr. Eva Grebel and Dr. Hubert Klahr for being the examiners of my defence.

I would like to acknowledge my collaborators Jesus Fàlcon-Barroso, Roberto Cid-Fernandes, Rosa González-Delgado, and E. Pérez, Tomas Ruiz-Lara, Jakob Walcher and Sebastian Sànches for their help and support during my work and career, as well all the people from CALIFA team. They made me proud to be part of a large and excellent collaboration.

A special thanks to Ronald Läscher, who is an amazing colleague and friend. I am happy to know him, because he was helping me always in my daily and scientific life. Thank you a lot for improving my English version of the thesis abstract and also making its translation into German.

Astronomy has made it possible for me to meet my great love and fiance Dario Colombo. Thank you, dear, for your daily support, patience, scientific and life discussions. Thank you also for your great meals and your sense of humour. Every day with you is an adventure.

I am grateful to Michael Maseda, Sarah Sadavoy, Jonatan McCreedy, Dario Colombo and Bozhana Filipova for helping me improve the English of this thesis.

Thanks to all my international friends and in particular - Trifon Trifonov and Anna Eremeeva (also my neighbours), Somayeh Sheikhnezami, Yu-Yen Chang, Sareh Ataiee, Sladjana Nikolic, Rahul Kannan, Dading Nugroho, Bala Ramkumar, Alberto Rorai, Tobias Albertsson, Karsten Dittrich, Maren Mohler-Fischer, Salvatore Cielo, Gabriele Cologna, Nikolay Kacharov, Fredrik Windmark, Maria Ewerlöf, Matthieu Brangier and Danielle Sorini.

My previous and current office-mates – Mario Gennaro, Bhargav Vaidya, Mauricio Cisternas, Min Fang, Miguel Querejeta, Natalie Raettig, Deniss Stepanovs and Kai-Martin Dittkrist. The members from our Dynamics group, who welcomed me everytime – Remco van de Bosch, Laura Watkins, Robert Singh, Akin Yildirim, Alex Büdenbender, Athanasia Tsatsi, Paolo Bianchini, Wilma Trick, Ling Zhu and Marie Martig.

I would like to acknowledge all of the employers at MPIA and particularly – Christian Fendt, Markus Pössel, Tom Herbst, Ingrid Apfel, Ina Beckmann, Uli Hiller, Björn Binroth, Heide Seifert, Frank Witzel and Britta Witzel.

Many thanks to my friends in Bulgaria – Kamelia Spassova, Andriana Spassova, Vaniya Chukova, Galin Gyulchev, Yanko Nikolov, Rostislav Kandilarov, Neli Dineva, Georgi Latev, Iglia Asenova and Tsvetan Vetsov.

I acknowledge my Bulgarian teachers and professors in Astronomy for their passion – Ivanka Getsova, Peter Kunchev, Plamen Fiziev, Valeri Golev, Tony Antonova, Petko Nedyalkov, Tsvetan Georgiev, Evgeni Ovcharov, Ivan Zhelyazkov, Georgi Ivanov, Orlin Stanchev, Todor Velchev, Ivanka Yankulova, Miglena Nikolchina, Tanyu Bonev, Alexander Antov and Boyko Mihov.

I express a great gratitude to my family, helping me to chase and reach my dreams – my mother Vanya Dimitrova and my father Kalin Dimitrov for giving me their unlimited love and support all the time; to my wonderful sister Mariya Kalinova for being my best friend and to my brother-in-law Aleksander Baytoshev – the most kind and generous person that I know.

Special thanks to my grandmother Mariya Georgieva whom I lost last year. Dear grandma, I will never forget your love and I hope that you are guiding me from the stars. Thank you always for supporting me and for giving me your beautiful garden to observe the night sky or count the meteors! I miss you very much and I hope that you will be always with me!

## BIBLIOGRAPHY

- Abadi, M. G., Navarro, J. F., Steinmetz, M., & Eke, V. R. 2003, *ApJ*, 597, 21
- Aguerri, J. A. L., Beckman, J. E., & Prieto, M. 1998, *AJ*, 116, 2136
- Allington-Smith, J. R., Content, R., Haynes, R., & Lewis, I. J. 1997, in *Society of Photo-Optical Instrumentation Engineers (SPIE) Conference Series*, Vol. 2871, *Optical Telescopes of Today and Tomorrow*, ed. A. L. Ardeberg, 1284–1294
- Arnold, R., de Zeeuw, P. T., & Hunter, C. 1994, *MNRAS*, 271, 924
- Arribas, S., Colina, L., Monreal-Ibero, A., Alfonso, J., García-Marín, M., & Alonso-Herrero, A. 2008, *A&A*, 479, 687
- Athanassoula, E. 2005, *MNRAS*, 358, 1477
- Avila-Reese, V., Firmani, C., & Zavala, J. 2002, in *Astronomical Society of the Pacific Conference Series*, Vol. 282, *Galaxies: the Third Dimension*, ed. M. Rosada, L. Binette, & L. Arias, 137
- Bacon, R., Emsellem, E., Copin, Y., & Monnet, G. 2000, in *Astronomical Society of the Pacific Conference Series*, Vol. 195, *Imaging the Universe in Three Dimensions*, ed. W. van Breugel & J. Bland-Hawthorn, 173
- Bacon, R., et al. 1988, in *European Southern Observatory Conference and Workshop Proceedings*, Vol. 30, *European Southern Observatory Conference and Workshop Proceedings*, ed. M.-H. Ulrich, 1185
- Bacon, R., et al. 1995a, *A&AS*, 113, 347
- . 1995b, *A&AS*, 113, 347
- . 2001a, *MNRAS*, 326, 23
- . 2001b, *MNRAS*, 326, 23
- Baes, M., et al. 2003, *MNRAS*, 343, 1081

- Bak, J., & Statler, T. S. 2000, *AJ*, 120, 110
- Banerjee, A., & Jog, C. J. 2012, ArXiv e-prints
- Barnes, J. E. 1994, in *The Formation and Evolution of Galaxies*, ed. C. Munoz-Tunon & F. Sanchez, 399
- Bayet, E., et al. 2013, *MNRAS*, 432, 1742
- Bedregal, A. G., Aragón-Salamanca, A., & Merrifield, M. R. 2006, *MNRAS*, 373, 1125
- Beers, T. C., & Sommer-Larsen, J. 1995, *ApJS*, 96, 175
- Begeman, K. G. 1987, PhD thesis, , Kapteyn Institute, (1987)
- Bekki, K., & Chiba, M. 2001, *ApJ*, 558, 666
- Bell, E. F., et al. 2008, *ApJ*, 680, 295
- Belokurov, V., et al. 2007, *ApJ*, 658, 337
- Bender, R., Doebereiner, S., & Moellenhoff, C. 1988, *A&AS*, 74, 385
- Bender, R., & Nieto, J.-L. 1990, *A&A*, 239, 97
- Bender, R., Saglia, R. P., & Gerhard, O. E. 1994, *MNRAS*, 269, 785
- Bender, R., Surma, P., Doebereiner, S., Moellenhoff, C., & Madejsky, R. 1989, *A&A*, 217, 35
- Bendo, G. J., & Barnes, J. E. 2000, *MNRAS*, 316, 315
- Bensby, T., Feltzing, S., Lundström, I., & Ilyin, I. 2005, *A&A*, 433, 185
- Benson, A. J., Lacey, C. G., Baugh, C. M., Cole, S., & Frenk, C. S. 2002, *MNRAS*, 333, 156
- Bigiel, F., & Blitz, L. 2012, *ApJ*, 756, 183
- Bigiel, F., Leroy, A., Walter, F., Brinks, E., de Blok, W. J. G., Madore, B., & Thornley, M. D. 2008, *AJ*, 136, 2846
- Binney, J. 1976, *MNRAS*, 177, 19
- . 1977, *ApJ*, 215, 483
- . 1978, *Comments on Astrophysics*, 8, 27
- Binney, J., & Merrifield, M. 1998a, *Galactic Astronomy*
- . 1998b, *Galactic Astronomy*
- Binney, J., & Tremaine, S. 1987, *Galactic dynamics*
- . 2008, *Galactic Dynamics: Second Edition* (Princeton University Press)
- Blanc, G. A., et al. 2010a, in *Astronomical Society of the Pacific Conference Series*, Vol. 432, *New Horizons in Astronomy: Frank N. Bash Symposium 2009*, ed. L. M. Stanford, J. D. Green, L. Hao, & Y. Mao, 180
- Blanc, G. A., et al. 2010b, in *Astronomical Society of the Pacific Conference Series*, Vol. 432, *New Horizons in Astronomy: Frank N. Bash Symposium 2009*, ed. L. M. Stanford, J. D. Green, L. Hao, & Y. Mao, 180
- Blumenthal, G. R., Faber, S. M., Primack, J. R., & Rees, M. J. 1984, *Nature*, 311, 517

- Böker, T., Laine, S., van der Marel, R. P., Sarzi, M., Rix, H.-W., Ho, L. C., & Shields, J. C. 2002, *AJ*, 123, 1389
- Boselli, A., & Gavazzi, G. 2006, *PASP*, 118, 517
- Bosma, A. 1978, PhD thesis, PhD Thesis, Groningen Univ., (1978)
- . 1981a, *AJ*, 86, 1791
- . 1981b, *AJ*, 86, 1791
- . 1981c, *AJ*, 86, 1825
- Bottema, R. 1993, *A&A*, 275, 16
- Bournaud, F., Elmegreen, B. G., & Martig, M. 2009, *ApJ*, 707, L1
- Bovy, J., & Rix, H.-W. 2013, *ApJ*, 779, 115
- Bovy, J., Rix, H.-W., & Hogg, D. W. 2012a, *ApJ*, 751, 131
- Bovy, J., Rix, H.-W., Liu, C., Hogg, D. W., Beers, T. C., & Lee, Y. S. 2012b, *ApJ*, 753, 148
- Bower, R. G., Benson, A. J., Malbon, R., Helly, J. C., Frenk, C. S., Baugh, C. M., Cole, S., & Lacey, C. G. 2006, *MNRAS*, 370, 645
- Boylan-Kolchin, M., Ma, C.-P., & Quataert, E. 2008, *MNRAS*, 383, 93
- Broeils, A. H. 1992, *A&A*, 256, 19
- Brook, C. B., Gibson, B. K., Martel, H., & Kawata, D. 2005, *ApJ*, 630, 298
- Brook, C. B., Kawata, D., Gibson, B. K., & Freeman, K. C. 2004, *ApJ*, 612, 894
- Brook, C. B., et al. 2012, *MNRAS*, 426, 690
- Bureau, M., & Freeman, K. C. 1999, *AJ*, 118, 126
- Burstein, D. 1979, *ApJ*, 234, 829
- Buta, R. J., & Zhang, X. 2009, *ApJS*, 182, 559
- Cantalupo, S. 2010, *MNRAS*, 403, L16
- Cappellari, M. 2002, *MNRAS*, 333, 400
- . 2008, *MNRAS*, 390, 71
- Cappellari, M., & Copin, Y. 2003, *MNRAS*, 342, 345
- Cappellari, M., & Emsellem, E. 2004, *PASP*, 116, 138
- Cappellari, M., et al. 2006, *MNRAS*, 366, 1126
- . 2007, *MNRAS*, 379, 418
- . 2011a, *MNRAS*, 413, 813
- . 2011b, *MNRAS*, 413, 813
- Carignan, C., & Freeman, K. C. 1985, *ApJ*, 294, 494
- Carollo, C. M., Scarlata, C., Stiavelli, M., Wyse, R. F. G., & Mayer, L. 2007, *ApJ*, 658, 960
- Carollo, C. M., Stiavelli, M., de Zeeuw, P. T., & Mack, J. 1997, *AJ*, 114, 2366
- Carollo, C. M., Stiavelli, M., & Mack, J. 1998, *AJ*, 116, 68

- Carollo, C. M., Stiavelli, M., Seigar, M., de Zeeuw, P. T., & Dejonghe, H. 2002, *AJ*, 123, 159
- Chiba, M., & Beers, T. C. 2000, *AJ*, 119, 2843
- Cid Fernandes, R., et al. 2013, *A&A*, 557, A86
- Collins, M. L. M., et al. 2013, *ApJ*, 768, 172
- Combes, F., & Elmegreen, B. G. 1993, *A&A*, 271, 391
- Combes, F., & Sanders, R. H. 1981, *A&A*, 96, 164
- Comerón, S., et al. 2011, *ApJ*, 741, 28
- Conroy, C., & Wechsler, R. H. 2009, *ApJ*, 696, 620
- Conroy, C., Wechsler, R. H., & Kravtsov, A. V. 2007, *ApJ*, 668, 826
- Corradi, R. L. M., & Capaccioli, M. 1990, *A&A*, 237, 36
- Croton, D. J., et al. 2006, *MNRAS*, 365, 11
- Dalcanton, J. J., & Bernstein, R. A. 2002, *AJ*, 124, 1328
- Dalcanton, J. J., Spergel, D. N., & Summers, F. J. 1997, *ApJ*, 482, 659
- Davies, R. L., & Birkinshaw, M. 1988, *ApJS*, 68, 409
- Davies, R. L., & Illingworth, G. 1983a, *ApJ*, 266, 516
- . 1983b, *ApJ*, 266, 516
- de Vaucouleurs, G. 1959, *Handbuch der Physik*, 53, 275
- de Vaucouleurs, G. 1974, in *IAU Symposium, Vol. 58, The Formation and Dynamics of Galaxies*, ed. J. R. Shakeshaft, 1–52
- . 1991, *Science*, 254, 1667
- de Zeeuw, P. T. 1996, in *Gravitational dynamics*, ed. O. Lahav, E. Terlevich, & R. J. Terlevich, 1
- de Zeeuw, P. T., et al. 2002, *MNRAS*, 329, 513
- de Zeeuw, T., & Franx, M. 1991, *ARA&A*, 29, 239
- Debattista, V. P., Carollo, C. M., Mayer, L., & Moore, B. 2004, *ApJ*, 604, L93
- . 2005, *ApJ*, 628, 678
- Debattista, V. P., Mayer, L., Carollo, C. M., Moore, B., Wadsley, J., & Quinn, T. 2006, *ApJ*, 645, 209
- Dehnen, W., & Binney, J. J. 1998, *MNRAS*, 298, 387
- Dekel, A., Sari, R., & Ceverino, D. 2009, *ApJ*, 703, 785
- Dekel, A., & Silk, J. 1986, *ApJ*, 303, 39
- Di Cintio, A., Brook, C. B., Macciò, A. V., Stinson, G. S., Knebe, A., Dutton, A. A., & Wadsley, J. 2014, *MNRAS*, 437, 415
- Doménech-Moral, M., Martínez-Serrano, F. J., Domínguez-Tenreiro, R., & Serna, A. 2012, *MNRAS*, 421, 2510
- D’Onofrio, M., Zaggia, S. R., Longo, G., Caon, N., & Capaccioli, M. 1995, *A&A*, 296, 319

- Dressler, A. 1980, *ApJ*, 236, 351
- Durrell, P. R., Harris, W. E., & Pritchett, C. J. 2001, *AJ*, 121, 2557
- Efstathiou, G. 1992, *MNRAS*, 256, 43P
- Eggen, O. J., Lynden-Bell, D., & Sandage, A. R. 1962, *ApJ*, 136, 748
- Emsellem, E., Monnet, G., & Bacon, R. 1994, *A&A*, 285, 723
- Emsellem, E., et al. 2004, *MNRAS*, 352, 721
- . 2007, *MNRAS*, 379, 401
- . 2011, *MNRAS*, 414, 888
- Evans, N. W., & de Zeeuw, P. T. 1994, *MNRAS*, 271, 202
- Falcón-Barroso, J., Sánchez-Blázquez, P., Vazdekis, A., Ricciardelli, E., Cardiel, N., Cenarro, A. J., Gorgas, J., & Peletier, R. F. 2011, *A&A*, 532, A95
- Falcón-Barroso, J., et al. 2006, *MNRAS*, 369, 529
- Fall, S. M., & Efstathiou, G. 1980a, *MNRAS*, 193, 189
- . 1980b, *MNRAS*, 193, 189
- Farouki, R. T., & Shapiro, S. L. 1982, *ApJ*, 259, 103
- Ferguson, A. M. N., Irwin, M. J., Ibata, R. A., Lewis, G. F., & Tanvir, N. R. 2002, *AJ*, 124, 1452
- Fisher, D. B., & Drory, N. 2008, *AJ*, 136, 773
- Franx, M., Illingworth, G., & de Zeeuw, T. 1991, *ApJ*, 383, 112
- Freeman, K. C. 1970, *ApJ*, 161, 802
- Frogel, J. A. 1988, *ARA&A*, 26, 51
- Fuentes-Carrera, I., Rosado, M., & Amram, P. 2003, in *Revista Mexicana de Astronomía y Astrofísica Conference Series*, Vol. 17, *Revista Mexicana de Astronomía y Astrofísica Conference Series*, ed. V. Avila-Reese, C. Firmani, C. S. Frenk, & C. Allen, 44–44
- Fuhrmann, K. 2008, *MNRAS*, 384, 173
- Ganda, K., Falcón-Barroso, J., Peletier, R. F., Cappellari, M., Emsellem, E., McDermid, R. M., de Zeeuw, P. T., & Carollo, C. M. 2006, *MNRAS*, 367, 46
- Ganda, K., Peletier, R. F., Balcells, M., & Falcón-Barroso, J. 2009, *MNRAS*, 395, 1669
- Ganda, K., et al. 2007, *MNRAS*, 380, 506
- Gebhardt, K., et al. 2000, *AJ*, 119, 1157
- . 2003, *ApJ*, 583, 92
- Gerhard, O., Jeske, G., Saglia, R. P., & Bender, R. 1998, *MNRAS*, 295, 197
- Gerhard, O., Kronawitter, A., Saglia, R. P., & Bender, R. 2001, *AJ*, 121, 1936
- Gerhard, O. E. 1981, *MNRAS*, 197, 179
- . 1993, *MNRAS*, 265, 213
- Gerhard, O. E., Vietri, M., & Kent, S. M. 1989, *ApJ*, 345, L33

- Gerssen, J., Kuijken, K., & Merrifield, M. R. 1997, *MNRAS*, 288, 618  
— . 2000, *MNRAS*, 317, 545
- Gilmore, G., & Reid, N. 1983, *MNRAS*, 202, 1025
- Gnedin, N. Y. 2000, *ApJ*, 542, 535
- Gnedin, N. Y., & Hollon, N. 2012, *ApJS*, 202, 13
- González Delgado, R. M., et al. 2014, *A&A*, 562, A47
- Governato, F., et al. 2010, *Nature*, 463, 203  
— . 2012, *MNRAS*, 422, 1231
- Grillmair, C. J. 2006, *ApJ*, 645, L37
- Häfner, R., Evans, N. W., Dehnen, W., & Binney, J. 2000, *MNRAS*, 314, 433
- Hambrick, D. C., Ostriker, J. P., Johansson, P. H., & Naab, T. 2011, *MNRAS*, 413, 2421
- Herschel, W. 1785, *Philosophical Transactions of the Royal Society of London (1776-1886)*, 113, 213
- Holmberg, E. 1950, *Meddelanden fran Lunds Astronomiska Observatorium Serie II*, 128, 1  
— . 1958, *Meddelanden fran Lunds Astronomiska Observatorium Serie II*, 136, 1
- Hopkins, P. F., et al. 2010, *ApJ*, 715, 202
- Hubble, E., & Humason, M. L. 1931, *ApJ*, 74, 43
- Hubble, E. P. 1926, *ApJ*, 64, 321  
— . 1936, *The Realm of the Nebulae*, New Haven: Yale University Press
- Hunter, C. 1977, *AJ*, 82, 271
- Husemann, B., Jahnke, K., & Sánchez et al., S. F. 2013, *A&A*, 549, A87
- Ibata, R., Irwin, M., Lewis, G., Ferguson, A. M. N., & Tanvir, N. 2001, *Nature*, 412, 49
- Jablonka, P., Tafelmeyer, M., Courbin, F., & Ferguson, A. M. N. 2010, *A&A*, 513, A78
- Jeans, J. H. 1915, *MNRAS*, 76, 70
- Johansson, P. H., Naab, T., & Ostriker, J. P. 2009, *ApJ*, 697, L38
- Jones, B. J. T., & Wyse, R. F. G. 1983, *A&A*, 120, 165
- Jorgensen, I., Franx, M., & Kjaergaard, P. 1996, *MNRAS*, 280, 167
- Jubelgas, M., Springel, V., Enßlin, T., & Pfrommer, C. 2008, *A&A*, 481, 33
- Jurić, M., et al. 2008, *ApJ*, 673, 864
- Kalnajs, A. J. 1983, in *IAU Symposium, Vol. 100, Internal Kinematics and Dynamics of Galaxies*, ed. E. Athanassoula, 109–115
- Kannan, R., et al. 2014, *MNRAS*, 437, 2882
- Kelson, D. D., et al. 2000, *ApJ*, 529, 768
- Kent, S. M. 1987, *AJ*, 93, 816  
— . 1990, *MNRAS*, 247, 702

- Khochfar, S., & Ostriker, J. P. 2008, *ApJ*, 680, 54
- Khochfar, S., & Silk, J. 2006, *MNRAS*, 370, 902
- Klypin, A. A., Trujillo-Gomez, S., & Primack, J. 2011, *ApJ*, 740, 102
- Konstantopoulos, I., et al. 2013, in *American Astronomical Society Meeting Abstracts*, Vol. 221, *American Astronomical Society Meeting Abstracts*, 215.01
- Kormendy, J. 1982, in *Saas-Fee Advanced Course 12: Morphology and Dynamics of Galaxies*, ed. L. Martinet & M. Mayor, 113–288
- Kormendy, J. 1993, in *IAU Symposium*, Vol. 153, *Galactic Bulges*, ed. H. Dejonghe & H. J. Habing, 209
- Kormendy, J. 1999, in *Astronomical Society of the Pacific Conference Series*, Vol. 182, *Galaxy Dynamics - A Rutgers Symposium*, ed. D. R. Merritt, M. Valluri, & J. A. Sellwood, 124
- Kormendy, J., & Kennicutt, Jr., R. C. 2004a, *ARA&A*, 42, 603
- . 2004b, *ARA&A*, 42, 603
- Krajnović, D., Cappellari, M., de Zeeuw, P. T., & Copin, Y. 2006, *MNRAS*, 366, 787
- Krajnović, D., et al. 2011, *MNRAS*, 414, 2923
- Kregel, M., & van der Kruit, P. C. 2005, *MNRAS*, 358, 481
- Kregel, M., van der Kruit, P. C., & de Grijs, R. 2002, *MNRAS*, 334, 646
- Kregel, M., van der Kruit, P. C., & Freeman, K. C. 2005, *MNRAS*, 358, 503
- Kuijken, K., & Gilmore, G. 1991, *ApJ*, 367, L9
- Kuijken, K., & Merrifield, M. R. 1993, *MNRAS*, 264, 712
- Kuntschner, H. 2000, *MNRAS*, 315, 184
- Kuzio de Naray, R., & McGaugh, S. S. 2014, *ApJ*, 782, L12
- Laine, S., Shlosman, I., Knapen, J. H., & Peletier, R. F. 2002, *ApJ*, 567, 97
- Lambas, D. G., Maddox, S. J., & Loveday, J. 1992, *MNRAS*, 258, 404
- Larson, R. B. 1974, *MNRAS*, 169, 229
- Laurikainen, E., Salo, H., Buta, R., Knapen, J. H., & Comerón, S. 2010, *MNRAS*, 405, 1089
- Law, D. R., & MaNGA Team. 2014, in *American Astronomical Society Meeting Abstracts*, Vol. 223, *American Astronomical Society Meeting Abstracts*, 254.31
- Lee, Y. S., et al. 2011, *ApJ*, 738, 187
- Lequeux, J., Combes, F., Dantel-Fort, M., Cuillandre, J.-C., Fort, B., & Mellier, Y. 1998, *A&A*, 334, L9
- Leroy, A. K., Walter, F., Brinks, E., Bigiel, F., de Blok, W. J. G., Madore, B., & Thornley, M. D. 2008, *AJ*, 136, 2782
- Lilly, S. J. 1989, *ApJ*, 340, 77
- Liu, C., & van de Ven, G. 2012, *MNRAS*, 425, 2144

- Loebman, S. R., Roškar, R., Debattista, V. P., Ivezić, Ž., Quinn, T. R., & Wadsley, J. 2011, *ApJ*, 737, 8
- Longair, M. S., ed. 1998, *Galaxy formation*
- Longair, M. S. 2008, *Galaxy Formation*
- Lynden-Bell, D. 1962, *MNRAS*, 123, 447
- Macciò, A. V., Stinson, G., Brook, C. B., Wadsley, J., Couchman, H. M. P., Shen, S., Gibson, B. K., & Quinn, T. 2012, *ApJ*, 744, L9
- Majewski, S. R. 1993, *ARA&A*, 31, 575
- Majewski, S. R., Siegel, M. H., Kunkel, W. E., Reid, I. N., Johnston, K. V., Thompson, I. B., Landolt, A. U., & Palma, C. 1999, *AJ*, 118, 1709
- Marsakov, V. A., Koval', V. V., Borkova, T. V., & Shapovalov, M. V. 2011, *Astronomy Reports*, 55, 667
- Martig, M., Bournaud, F., Teyssier, R., & Dekel, A. 2009, *ApJ*, 707, 250
- Martinsson, T. P. K., Verheijen, M. A. W., Westfall, K. B., Bershadsky, M. A., Andersen, D. R., & Swaters, R. A. 2013, *A&A*, 557, A131
- Martizzi, D., Teyssier, R., & Moore, B. 2012, *MNRAS*, 420, 2859
- McConnachie, A. W. 2012, *AJ*, 144, 4
- Merrifield, M. R., & Kuijken, K. 1995, *MNRAS*, 274, 933
- Merritt, D. 1997, *AJ*, 114, 228
- Mignard, F. 2000, *A&A*, 354, 522
- Minchev, I., & Famaey, B. 2010, *ApJ*, 722, 112
- Mo, H., van den Bosch, F. C., & White, S. 2010, *Galaxy Formation and Evolution*
- Mo, H. J., Mao, S., & White, S. D. M. 1998, *MNRAS*, 295, 319
- Monnet, G., Bacon, R., & Emsellem, E. 1992, *A&A*, 253, 366
- Moore, B., Katz, N., Lake, G., Dressler, A., & Oemler, A. 1996, *Nature*, 379, 613
- Moore, B., Lake, G., Quinn, T., & Stadel, J. 1999, *MNRAS*, 304, 465
- Moster, B. P., Naab, T., & White, S. D. M. 2013, *MNRAS*, 428, 3121
- Moster, B. P., Somerville, R. S., Maulbetsch, C., van den Bosch, F. C., Macciò, A. V., Naab, T., & Oser, L. 2010, *ApJ*, 710, 903
- Mouhcine, M., Ferguson, H. C., Rich, R. M., Brown, T. M., & Smith, T. E. 2005, *ApJ*, 633, 821
- Naab, T., Burkert, A., & Hernquist, L. 1999, *ApJ*, 523, L133
- Naab, T., & Trujillo, I. 2006, *MNRAS*, 369, 625
- Navarro, J. F., Frenk, C. S., & White, S. D. M. 1997a, *ApJ*, 490, 493
- . 1997b, *ApJ*, 490, 493
- Navarro, J. F., & Steinmetz, M. 1997, *ApJ*, 478, 13

- Neistein, E., Maoz, D., Rix, H.-W., & Tonry, J. L. 1999, *AJ*, 117, 2666
- Noordermeer, E., & van der Hulst, J. M. 2007, *MNRAS*, 376, 1480
- Noordermeer, E., van der Hulst, J. M., Sancisi, R., Swaters, R. S., & van Albada, T. S. 2007, *MNRAS*, 376, 1513
- Norris, J. E., & Ryan, S. G. 1991, *ApJ*, 380, 403
- Oort, J. H. 1932a, *Bull. Astron. Inst. Netherlands*, 6, 289
- . 1932b, *Bull. Astron. Inst. Netherlands*, 6, 249
- Oppenheimer, B. D., & Davé, R. 2008, *MNRAS*, 387, 577
- Ostriker, J. P., & Peebles, P. J. E. 1973, *ApJ*, 186, 467
- Palunas, P., & Williams, T. B. 2000, *AJ*, 120, 2884
- Peletier, R. F., Valentijn, E. A., & Jameson, R. F. 1990, *A&A*, 233, 62
- Peng, E. W., Ford, H. C., Freeman, K. C., & White, R. L. 2002, *AJ*, 124, 3144
- Persic, M., & Salucci, P. 1988, *MNRAS*, 234, 131
- Persic, M., Salucci, P., & Stel, F. 1996, *MNRAS*, 281, 27
- Pfenniger, D., & Norman, C. 1990, *ApJ*, 363, 391
- Pizagno, J., et al. 2005, *ApJ*, 633, 844
- Poggianti, B. M., Smail, I., Dressler, A., Couch, W. J., Barger, A. J., Butcher, H., Ellis, R. S., & Oemler, Jr., A. 1999, *ApJ*, 518, 576
- Puchwein, E., Pfrommer, C., Springel, V., Broderick, A. E., & Chang, P. 2012, *MNRAS*, 423, 149
- Quillen, A. C., Minchev, I., Bland-Hawthorn, J., & Haywood, M. 2009, *MNRAS*, 397, 1599
- Quinn, P. J., Hernquist, L., & Fullagar, D. P. 1993, *ApJ*, 403, 74
- Raha, N., Sellwood, J. A., James, R. A., & Kahn, F. D. 1991, *Nature*, 352, 411
- Read, J. I., Lake, G., Agertz, O., & Debattista, V. P. 2008, *MNRAS*, 389, 1041
- Reddy, B. E., Lambert, D. L., & Allende Prieto, C. 2006, *MNRAS*, 367, 1329
- Rees, M. J. 1986, *MNRAS*, 218, 25P
- Rees, M. J., & Ostriker, J. P. 1977, *MNRAS*, 179, 541
- Rieke, G. H., & Lebofsky, M. J. 1985, *ApJ*, 288, 618
- Rix, H.-W., de Zeeuw, P. T., Cretton, N., van der Marel, R. P., & Carollo, C. M. 1997, *ApJ*, 488, 702
- Rix, H.-W., & White, S. D. M. 1992, *MNRAS*, 254, 389
- Rix, H.-W., & Zaritsky, D. 1995, *ApJ*, 447, 82
- Rocha-Pinto, H. J., Majewski, S. R., Skrutskie, M. F., & Crane, J. D. 2003, *ApJ*, 594, L115
- Rosales-Ortega, F. F., Kennicutt, R. C., Sánchez, S. F., Díaz, A. I., Pasquali, A., Johnson, B. D., & Hao, C. N. 2010, *MNRAS*, 405, 735

- Rubin, V. C. 2000, *PASP*, 112, 747
- Rubin, V. C., Burstein, D., Ford, Jr., W. K., & Thonnard, N. 1985, *ApJ*, 289, 81
- Rubin, V. C., & Ford, Jr., W. K. 1983, *ApJ*, 271, 556
- Rubin, V. C., Ford, Jr., W. K., Strom, K. M., Strom, S. E., & Romanishin, W. 1978a, *ApJ*, 224, 782
- Rubin, V. C., Ford, W. K. J., & Thonnard, N. 1980, *ApJ*, 238, 471
- Rubin, V. C., Thonnard, N., & Ford, Jr., W. K. 1978b, *ApJ*, 225, L107
- Ruiz-Lara, T., Florido, E., Pérez, I., Sánchez-Blázquez, P., Falcón-Barroso, J., & Cacho, R. 2013, in *Highlights of Spanish Astrophysics VII*, 367–372
- Ryden, B. S. 2004, *ApJ*, 601, 214
- Sackett, P. D. 1997, *ApJ*, 483, 103
- Sackett, P. D., Morrisoni, H. L., Harding, P., & Boroson, T. A. 1994, *Nature*, 370, 441
- Saha, P., & Williams, T. B. 1994, *AJ*, 107, 1295
- Sánchez, S. F. 2006, *Astronomische Nachrichten*, 327, 850
- Sánchez, S. F., et al. 2012a, *A&A*, 538, A8
- . 2012b, *A&A*, 538, A8
- Sánchez-Blázquez, P., Forbes, D. A., Strader, J., Brodie, J., & Proctor, R. 2007, *MNRAS*, 377, 759
- Sánchez-Blázquez, P., et al. 2006, *MNRAS*, 371, 703
- Sancisi, R. 1985, *Mem. Soc. Astron. Italiana*, 56, 709
- Sancisi, R. 2004, in *IAU Symposium, Vol. 220, Dark Matter in Galaxies*, ed. S. Ryder, D. Pisano, M. Walker, & K. Freeman, 233
- Sandage, A. 1961, *The Hubble atlas of galaxies*
- . 1975, *Classification and Stellar Content of Galaxies Obtained from Direct Photography*, ed. A. Sandage, M. Sandage, & J. Kristian (the University of Chicago Press), 1
- Sandage, A., & Bedke, J. 1994, *The Carnegie Atlas of Galaxies. Volumes I, II*.
- Sandage, A., Freeman, K. C., & Stokes, N. R. 1970a, *ApJ*, 160, 831
- . 1970b, *ApJ*, 160, 831
- Schönrich, R., & Binney, J. 2009a, *MNRAS*, 396, 203
- . 2009b, *MNRAS*, 399, 1145
- Schruba, A., et al. 2011, *AJ*, 142, 37
- Schwarzschild, M. 1979, *ApJ*, 232, 236
- Searle, L., & Zinn, R. 1978, *ApJ*, 225, 357
- Sellwood, J. A., & Binney, J. J. 2002, *MNRAS*, 336, 785
- Seth, A. C., Dalcanton, J. J., & de Jong, R. S. 2005, *AJ*, 130, 1574

- Shapiro, K. L., Gerssen, J., & van der Marel, R. P. 2003, *AJ*, 126, 2707
- Simien, F., & de Vaucouleurs, G. 1986, *ApJ*, 302, 564
- Slipher, V. M. 1914, *Popular Astronomy*, 22, 19
- Sofue, Y., Tutui, Y., Honma, M., Tomita, A., Takamiya, T., Koda, J., & Takeda, Y. 1999, *ApJ*, 523, 136
- Somerville, R. S., & Primack, J. R. 1999, *MNRAS*, 310, 1087
- Somerville, R. S., et al. 2008, *ApJ*, 672, 776
- Spitzer, Jr., L., & Baade, W. 1951, *ApJ*, 113, 413
- Springel, V., et al. 2005, *NATURE*, 435, 629
- Stark, A. A. 1977, *ApJ*, 213, 368
- Statler, T. S. 1988, *ApJ*, 331, 71
- . 1991, *ApJ*, 382, L11
- . 1994, *AJ*, 108, 111
- Statler, T. S., & Smecker-Hane, T. 1999, *AJ*, 117, 839
- Steinmetz, M., & Navarro, J. F. 2002, *New Astronomy*, 7, 155
- Swaters, R. A., Sancisi, R., van Albada, T. S., & van der Hulst, J. M. 2009, *A&A*, 493, 871
- Teyssier, R., Moore, B., Martizzi, D., Dubois, Y., & Mayer, L. 2011, *MNRAS*, 414, 195
- Theis, C. 2004, in *IAU Symposium*, Vol. 220, *Dark Matter in Galaxies*, ed. S. Ryder, D. Pisano, M. Walker, & K. Freeman, 461
- Thomas, J., Saglia, R. P., Bender, R., Thomas, D., Gebhardt, K., Magorrian, J., Corsini, E. M., & Wegner, G. 2007, *MNRAS*, 382, 657
- Toth, G., & Ostriker, J. P. 1992, *ApJ*, 389, 5
- Tsikoudi, V. 1980, *ApJS*, 43, 365
- Valluri, M., Merritt, D., & Emsellem, E. 2004, *ApJ*, 602, 66
- van Albada, T. S., Bahcall, J. N., Begeman, K., & Sancisi, R. 1985, *ApJ*, 295, 305
- van de Ven, G., Falcón-Barroso, J., McDermid, R. M., Cappellari, M., Miller, B. W., & de Zeeuw, P. T. 2010, *ApJ*, 719, 1481
- van de Ven, G., van den Bosch, R. C. E., Verolme, E. K., & de Zeeuw, P. T. 2006, *A&A*, 445, 513
- van den Bergh, S. 1976, *ApJ*, 206, 883
- . 1998, *Galaxy Morphology and Classification*
- van den Bosch, F. C. 1998, *ApJ*, 507, 601
- . 2000, *ApJ*, 530, 177
- van den Bosch, R., de Zeeuw, T., Gebhardt, K., Noyola, E., & van de Ven, G. 2006, *ApJ*, 641, 852

- van den Bosch, R. C. E., & de Zeeuw, P. T. 2010, *MNRAS*, 401, 1770
- van den Bosch, R. C. E., van de Ven, G., Verolme, E. K., Cappellari, M., & de Zeeuw, P. T. 2008, *MNRAS*, 385, 647
- van der Marel, R. P. 1994, *ApJ*, 432, L91
- van der Marel, R. P., & Franx, M. 1993, *ApJ*, 407, 525
- van der Marel, R. P., & van den Bosch, F. C. 1998, *AJ*, 116, 2220
- van Gorkom, J. H. 2004, *Clusters of Galaxies: Probes of Cosmological Structure and Galaxy Evolution*, 305
- Vazdekis, A., Sánchez-Blázquez, P., Falcón-Barroso, J., Cenarro, A. J., Beasley, M. A., Cardiel, N., Gorgas, J., & Peletier, R. F. 2010, *MNRAS*, 404, 1639
- Verolme, E. K., et al. 2002, *MNRAS*, 335, 517
- Villalobos, Á., & Helmi, A. 2008, *MNRAS*, 391, 1806
- Vivas, A. K., & Zinn, R. 2006, *AJ*, 132, 714
- Vogelsberger, M., Genel, S., Sijacki, D., Torrey, P., Springel, V., & Hernquist, L. 2013, *MNRAS*, 436, 3031
- Wada, K., & Koda, J. 2004, *MNRAS*, 349, 270
- Wadepuhl, M., & Springel, V. 2011, *MNRAS*, 410, 1975
- Walker, M. G., Mateo, M., Olszewski, E. W., Gnedin, O. Y., Wang, X., Sen, B., & Woodroffe, M. 2007, *ApJ*, 667, L53
- Weijmans, A.-M., Krajnović, D., van de Ven, G., Oosterloo, T. A., Morganti, R., & de Zeeuw, P. T. 2008, *MNRAS*, 383, 1343
- Weil, M. L., & Hernquist, L. 1996, *ApJ*, 460, 101
- Weitzel, L., Krabbe, A., Kroker, H., Thatte, N., Tacconi-Garman, L. E., Cameron, M., & Genzel, R. 1996, *A&AS*, 119, 531
- White, M., Zheng, Z., Brown, M. J. I., Dey, A., & Jannuzi, B. T. 2007, *ApJ*, 655, L69
- White, S. D. M., & Rees, M. J. 1978, *MNRAS*, 183, 341
- Williams, M. J., Bureau, M., & Cappellari, M. 2009, *MNRAS*, 400, 1665
- . 2010, *MNRAS*, 409, 1330
- Woodgate, B. E., et al. 1998, *PASP*, 110, 1183
- Yang, X., Mo, H. J., & van den Bosch, F. C. 2003, *MNRAS*, 339, 1057
- Yanny, B., et al. 2000, *ApJ*, 540, 825
- Yoachim, P., & Dalcanton, J. J. 2005, *ApJ*, 624, 701
- . 2006, *AJ*, 131, 226
- Young, L. M. 2002, *AJ*, 124, 788
- Young, L. M., et al. 2011, *MNRAS*, 414, 940

Zasov, A. V., & Kyazumov, G. A. 1983, *Soviet Ast.*, 27, 384

Zibetti, S., White, S. D. M., & Brinkmann, J. 2004, *MNRAS*, 347, 556

Zwicky, F. 1933, *Helvetica Physica Acta*, 6, 110